PROBING PROTON CROSS-SHELL EXCITATIONS IN ^{70}NI USING NUCLEON KNOCKOUT REACTIONS

By

Brandon Alexander Elman

A DISSERTATION

Submitted to
Michigan State University
in partial fulfillment of the requirements
for the degree of

Physics — Doctor of Philosophy

2019

ABSTRACT

PROBING PROTON CROSS-SHELL EXCITATIONS IN ^{70}NI USING NUCLEON KNOCKOUT REACTIONS

By

Brandon Alexander Elman

The neutron-rich Ni isotopes serve as an important benchmark for nuclear structure models because they exhibit interesting phenomena such as shape or configuration coexistence driven by cross-shell excitations. Reported here are the excited-state population distributions following one-proton, one-neutron, and two-proton knockout from ^{71}Cu, ^{71}Ni, and ^{72}Zn, respectively, into excited states of ^{70}Ni. By comparing these final-state populations, this work will attempt to determine the role of neutron and proton excitations separately in the configurations of excited states. The specific aim is to identify those excited states associated with configurations containing proton excitations across the $Z = 28$ shell gap. These levels are suggested in the literature to be associated with prolate deformation at relatively low excitation energy compared to neighboring isotopes in the nickel chain.

TABLE OF CONTENTS

LIST OF TABLES

LIST OF FIGURES

Chapter 1

Introduction

1.1 Nuclear physics

Nuclear physics is concerned with nuclei, strongly-interacting systems composed of neutrons and protons. Neutrons and protons are fermions, particles of half-integer spin $s = 1/2$, and are collectively known as *nucleons*. The number of protons and neutrons will henceforth be referred to as Z and N, respectively. In the shell-model picture of nuclei, nucleons fill energy orbitals with distinct quantum numbers based on the *Pauli exclusion principle*, which states that indistinguishable fermions in the same quantum system cannot have the same quantum numbers.

Orbitals are labeled by their quantum numbers nlj, where $n = 0, 1, 2, \ldots$ is the principal quantum number and $l = 0, 1, 2, \ldots$ is the orbital angular momentum quantum number. The orbital angular momentum and spin are coupled to a total angular momentum $\vec{j} = \vec{l} + \vec{s}$, and $j = l \pm 1/2$ is the total angular momentum quantum number. Typically, the orbital angular momentum is represented in spectroscopic notation, so that the different values $l = 0, 1, 2, 3, 4, \ldots$ are represented as $l = s, p, d, f, g, \ldots$ instead. For each j value, there are $2j+1$ magnetic sub-states indicated by a magnetic quantum number $m = -j, -j+1, \ldots, j-1, j$, which is the z-projection of $\vec{j}$. Every orbital labeled nlj can therefore be occupied by $2j + 1$ nucleons, because no two fermions can occupy the same $nljm$ state. Note that because

protons and neutrons are distinguishable, a proton and a neutron can share the same $nljm$ values, though two protons or two neutrons cannot. Normal-order configurations refer to the distribution of the nucleons between the different single-particle orbitals in the case where only the lowest-energy orbitals allowed by the Pauli exclusion principle are filled. Figure 1.1 presents a simple view of a normal-order configuration for the ground state of ^{17}O.

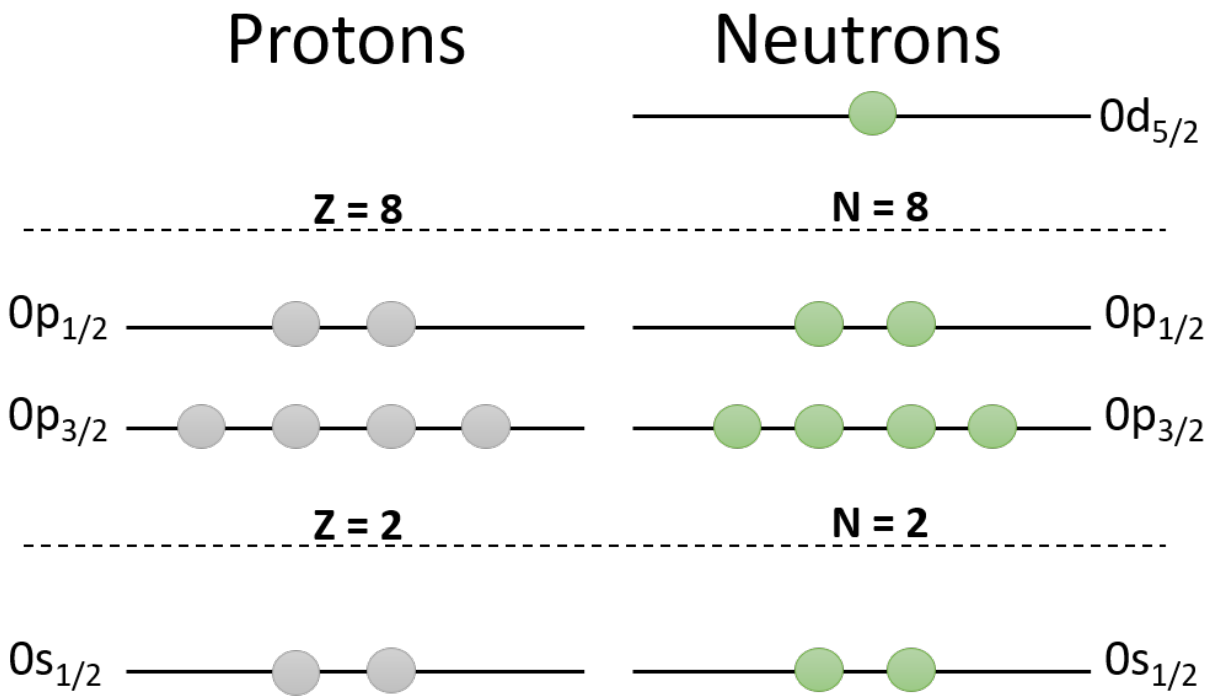

Figure 1.1: Simplified picture for the single-particle configuration of the ground state of ^{17}O with the shell gaps at $N, Z = 2, 8$.

Parity (written as π) is a characteristic of nuclear states that describes the behavior of the wavefunction under the parity transformation: $x \to -x,\ y \to -y,\ z \to -z$. Parity can either be even ($\pi = +1$) or odd ($\pi = -1$), and is determined by $(-1)^l$. Energy levels in nuclei are most-often presented in terms of the *spin-parity*, or J^π, where $\vec{J} = \sum_{i=1}^{A} \vec{j}$, A being the number of nucleons.

1.1.1 Nuclear shell model

In the independent-particle shell model, nucleons are modeled as moving independently in a mean-field created by all the other nucleons. There are relatively large energy gaps between sets of orbitals at certain numbers of protons or neutrons known as magic numbers (i.e., $2, 8, 20, 28, 50, 82, 126$) analogous to the situation in the atomic shell model. A shell is considered to be *closed* when all orbitals below it are filled by the allowed number of nucleons based on the Pauli principle. So-called *valence* nucleons are the nucleons outside of these closed shells. Nucleons tend to form pairs such that each pair has total spin 0 and even parity, leaving the unpaired valence nucleons to determine the spin-parity of a given nuclear state. For example, the unpaired nucleon in the $0d_{5/2}$ orbital in ^{17}O (see Fig. 1.1) leads to a ground-state spin-parity of $5/2^+$.

Shell gaps result in observable shell effects in nuclei that are *singly-magic*, wherein Z or N is a magic number, or *doubly-magic*, wherein both are magic numbers, when compared to neighboring nuclei. For example, *even-even* nuclei are nuclei with an even Z and N. The ground state of even-even nuclei always has spin-parity $J^\pi = 0^+$, and the first excited state has, in most cases, $J^\pi = 2^+$. For singly- and doubly-magic nuclei, the excitation energy of the 2^+ is generally larger than this same quantity in non-magic nuclei. Another sign of magicity is a small *electric quadrupole transition rate*, written as $B(E2; 0_1^+ \rightarrow 2_1^+)$, between the ground state and the 2_1^+ state in even-even nuclei, which is systematically smaller when comparing magic nuclei to neighboring nuclei. This quantity will be introduced in the following section.

1.1.2 Electromagnetic transitions in nuclei

Decays between states of an atomic nucleus most commonly involve γ-ray emission. The γ-ray energy is equal to the energy difference between the initial and final state, with a negligible contribution from the recoil of the atomic nucleus. A schematic view of γ decay is shown in Fig. 1.2

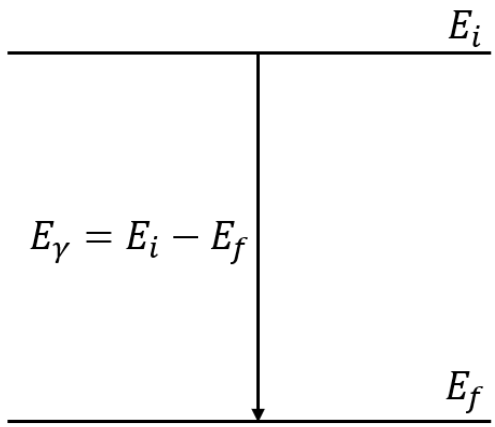

Figure 1.2: A schematic view of γ decay from the excited state of energy E_i to a state at lower energy E_f.

Electromagnetic transitions are differentiated by the amount of angular momentum λ carried away and the parity of the initial and final states. Consider an initial state of spin-parity $J_i^{\pi i}$ and final state with spin-parity $J_f^{\pi f}$. Because photons are bosons, they must carry away at least one unit of angular momentum, meaning that γ-ray transitions between two states with $J_i = J_f = 0$ are forbidden. In this case, the decay is mediated by emission of conversion electrons and/or internal-pair formation if the energy difference exceeds 1022 keV. Because of conservation of angular momentum, λ for the photon can take integer values between $|J_i - J_f| \leq \lambda \leq J_i + J_f$, except $\lambda = 0$ as noted above. This carried-away angular momentum determines the *multipolarity* of the transition; i.e., $\lambda = 1$ is a dipole transition, $\lambda = 2$ is a quadrupole transition, and so on.

In terms of parity, the parity carried by photons is $(-1)^{\lambda}$ for those associated with the electric multipoles or $(-1)^{\lambda+1}$ for the magnetic multipoles. These are denoted by either E or M, respectively. Therefore, due to parity conservation, if $\pi_i = \pi_f$ $M1, E2, M3, E4, \ldots$ are the possible transitions. The possible transitions are $E1, M2, E3, M4, \ldots$ otherwise. Because photons cannot have $\lambda = 0$, $E0$ radiation denotes decays proceeding through conversion-electron emission.

Let $\sigma \in E, M$ represent whether the transition is electric or magnetic. The transition rate T can be written [13] as the sum of matrix elements for the tensor operators $O_{\sigma\lambda\mu}$ of rank λ, where μ is the projection of λ:

$$T_{M_i,M_f,\mu} = \sum_{\sigma\lambda} \left(\frac{8\pi(\lambda+1)}{\lambda[(2\lambda+1)!!]^2} \right) \frac{1}{\hbar} \left(\frac{E_\gamma}{\hbar c} \right)^{2\lambda+1} | < J_f M_f | O(\sigma\lambda)_\mu | J_i M_i > |^2 \tag{1.1}$$

where E_γ is the γ-ray energy, $\hbar$ is the reduced Planck constant, c is the speed of light, and $\hbar c = 197$ MeV fm.

One can then sum over the M_f and μ values since they are not observed individually and average over the initial states to rewrite $T_{M_i,M_f,\mu}$ in terms of reduced matrix elements:

$$T = \frac{1}{2J_i+1} \sum_{M_i} \sum_{M_f,\mu} T_{M_i,M_f,\mu} \tag{1.2}$$

$$= \sum_{\sigma\lambda} \left(\frac{8\pi(\lambda+1)}{\lambda[(2\lambda+1)!!]^2} \right) \frac{1}{\hbar} \left(\frac{E_\gamma}{\hbar c} \right)^{2\lambda+1} \frac{| < J_f || O(\sigma\lambda) || J_i > |^2}{2J_i+1} \tag{1.3}$$

$$= \sum_{\sigma\lambda} \left(\frac{8\pi(\lambda+1)}{\lambda[(2\lambda+1)!!]^2} \right) \frac{1}{\hbar} \left(\frac{E_\gamma}{\hbar c} \right)^{2\lambda+1} B(\sigma\lambda; J_i \to J_f) \tag{1.4}$$

where $B(\sigma\lambda; J_i \rightarrow J_f)$ is the *reduced transition probability.*

Although λ can take all of the values allowed by angular momentum conservation, the lowest-allowed multipolarity λ for either electric or magnetic transitions will have a transition rate several orders of magnitude higher than transitions with the multipolarity $\lambda+2$; e.g., for $J_i^{\pi i} = 4^+$ and $J_f^{\pi f} = 3^+$, $E2$ and $M1$ transitions are more than seven orders of magnitude stronger than $E4$ and $M3$ transitions, which are also allowed. For transitions of mixed multipolarity, such as the aforementioned $4^+ \rightarrow 3^+$ or $2^+ \rightarrow 2^+$, the *multipole mixing ratio* δ is defined, where in the case of $E2 - M1$ transitions:

$$\delta^2 \left(\frac{E2}{M1} \right) = \frac{T(E2)}{T(M1)} \tag{1.5}$$

The *lifetime* τ of an excited state is related to the transition rate:

$$\tau = \frac{1}{T} \tag{1.6}$$

For E2 transitions, the partial mean lifetime can be written as:

$$\tau_p = \frac{816}{E_\gamma^5 B(E2)} e^2\text{fm}^4\text{MeV}^5\text{ps}, \tag{1.7}$$

where the B(E2) value is in $e^2\text{fm}^4$ and the energy E_γ is in MeV. The diagonal transition matrix elements, i.e. the transition matrix elements where the initial and final states are the same, are moments such as the electric quadrupole moment. These can quantify the shape of a nucleus in a given state.

Shape coexistence is the peculiar nuclear phenomenon where, at low excitation energy and within a narrow energy range, two or more states (or band structures of states) exist

which can be interpreted in terms of different intrinsic shapes.

1.2 Shape and configuration coexistence in exotic nuclei

On a microscopic level, shape coexistence in nuclei can be caused by the competition between normal-order configurations and configurations involving excitations across shell gaps, referred to as *cross-shell* excitations, at relatively low excitation energy. These states resulting from cross-shell excitations often exhibit different electric quadrupole properties, such as moments and transition rates, than those based on normal-order configurations. While initially believed to be a rare occurrence on the nuclear chart, there is now evidence that shape coexistence may occur in almost all nuclei [14].

The most common shapes for nuclear systems are spherical, prolate (cigar-like), and oblate (pancake-like), which are shown in Fig. 1.3. More exotic nuclear shapes, such as pear-like shapes due to octupole deformations, exist but are less prevalent in the regions of the nuclear chart discussed here. Assuming neither triaxiality nor higher-order deformations beyond quadrupole, Fig. 1.3 approximates the nuclear shape $R(\theta, \phi)$ as:

$$R(\theta, \phi) = 1 + \beta Y_{2,0}(\theta, \phi), \tag{1.8}$$

where $Y_{2,0}(\theta, \phi)$ is a spherical harmonic, and β is the quadrupole deformation parameter, whose sign determines whether a nucleus is prolate or oblate. Prolate deformations correspond to positive quadrupole deformation parameters, in contrast with oblate nuclei which correspond to negative ones. It is possible for excited states of a nucleus to exhibit dramatically different shapes compared to the ground state of the same nucleus.

On a microscopic level, the effect of cross-shell excitations across a shell gap are par-

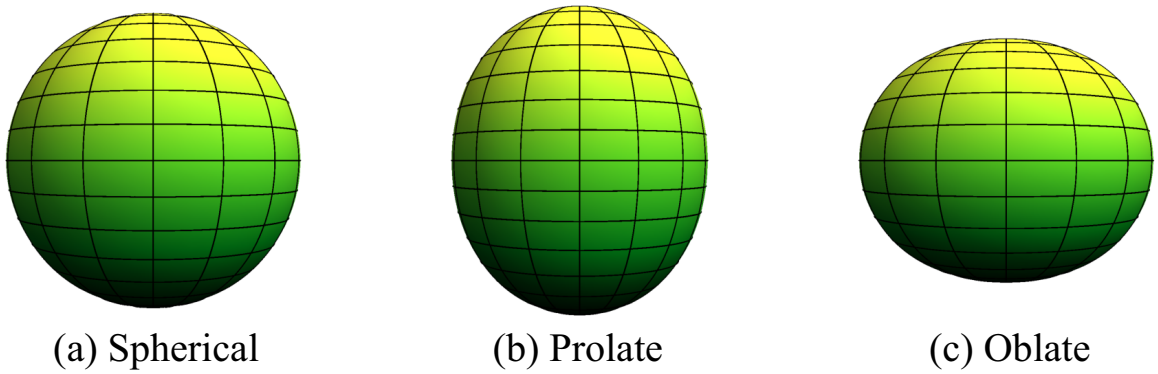

Figure 1.3: Common shapes of atomic nuclei. In panels (b) and (c) the magnitude of the quadrupole deformation parameter was chosen to be $|\beta| = 0.2$.

ticularly interesting in neutron-rich singly-magic nuclei. These cross-shell excitations into so-called *intruder* orbitals outside of the normal-order shell fillings, become energetically favored because of a variety of effects, such as quadrupole correlations [14] or the proton-neutron tensor force [15].

Along the nickel isotopic chain, for example, the proton-neutron tensor force is one driver responsible for changes to the nuclear structure. The effect of the *proton-neutron* tensor interaction can be described in a simplified way by considering $j_> = l+1/2$ and $j_< = l-1/2$ orbitals separately. Consider the following example. The neutrons in the $0g_{9/2}$ ($j_>$) orbital interact with the proton $0f_{7/2}$ ($j_>$) and $0f_{5/2}$ ($j_<$) orbitals. The interaction between $j_>j_>$ and $j_<j_<$ orbitals is repulsive; i.e., the orbital being acted on becomes less bound. In contrast, the interaction between $j_>j_<$ orbitals is attractive. Therefore, as the number of neutrons in the $0g_{9/2}$ increases, the gap between the $0f_{5/2}$ and $0f_{7/2}$ decreases, and the likelihood of excitations across the $Z = 28$ shell gap increases. This interaction is strongest when the $0g_{9/2}$ orbital is half-filled; i.e., when it contains $\frac{2j+1}{2} = 5$ nucleons.

Effects like the aforementioned proton-neutron tensor force leads to states associated

with these excitations across shell gaps being at relatively low excitation energy compared to states associated with similar configurations in stable nuclei. This work will focus on the singly-magic ($Z = 28$) Ni isotopes, in particular on ^{70}Ni, in which several states have been associated with configurations based on such cross-shell excitations.

1.3 Shape coexistence in the Ni isotopes

Shape coexistence appears as a common feature in the neutron-rich Ni isotopes, as evidenced by recent work on ^{66,68,70}Ni [1, 3, 16–19] and predictions for ^{78}Ni [20, 21]. In ^{78}Ni, which is doubly-magic, shell-model calculations [20] predicted that the first excited state is a prolate-deformed, 2.65 MeV 0^+ state. This 0^+ state serves as the bandhead of a prolate-deformed intruder band and signals an *island of inversion* centered on $N = 50$ analogous to those at $N = 8, 20, 28,$ and 40. An island of inversion [22, 23] is a region of the nuclear chart where the traditional shell gaps seem to disappear, so that states associated with configurations involving multiple particles being excited across shell gaps energetically compete with normal-order configurations.

Proposed [19] as one of the lightest known systems to exhibit shape isomerism, ^{66}Ni is known to have four low-lying 0^+ states. A hindered γ transition between the prolate-deformed 0^+_4 state and the *yrast* 2^+_1 level has been reported in ^{66}Ni based on the small measured electric quadrupole transition strengths. Note that yrast refers to a state of a nucleus with the lowest energy for a given spin-parity, such as the ground-state band (0^+_1, 2^+_1, 4^+_1, ...). Such *shape isomerism* occurs when a large potential energy barrier exists between the states associated with different deformations.

The situation is quite different for ^{68}Ni, which appears to exhibit substantial mixing

between deformed and spherical configurations [17]. There are three known 0^+ states in ^{68}Ni associated with different shapes [1, 16, 17]: the spherical ground state, an oblate deformed level at 1604 keV, and a prolate deformed one at 2511 keV, where the shapes have been inferred from shell-model calculations [1, 16]. A potential energy surface calculated [1, 16] for ^{68}Ni using Hartree-Fock constrained by the quadrupole moment determined from the Monte Carlo shell model Hamiltonian is shown in Fig. 1.4. The minima in the potential energy surface correspond to the different 0^+ states associated with different shapes.

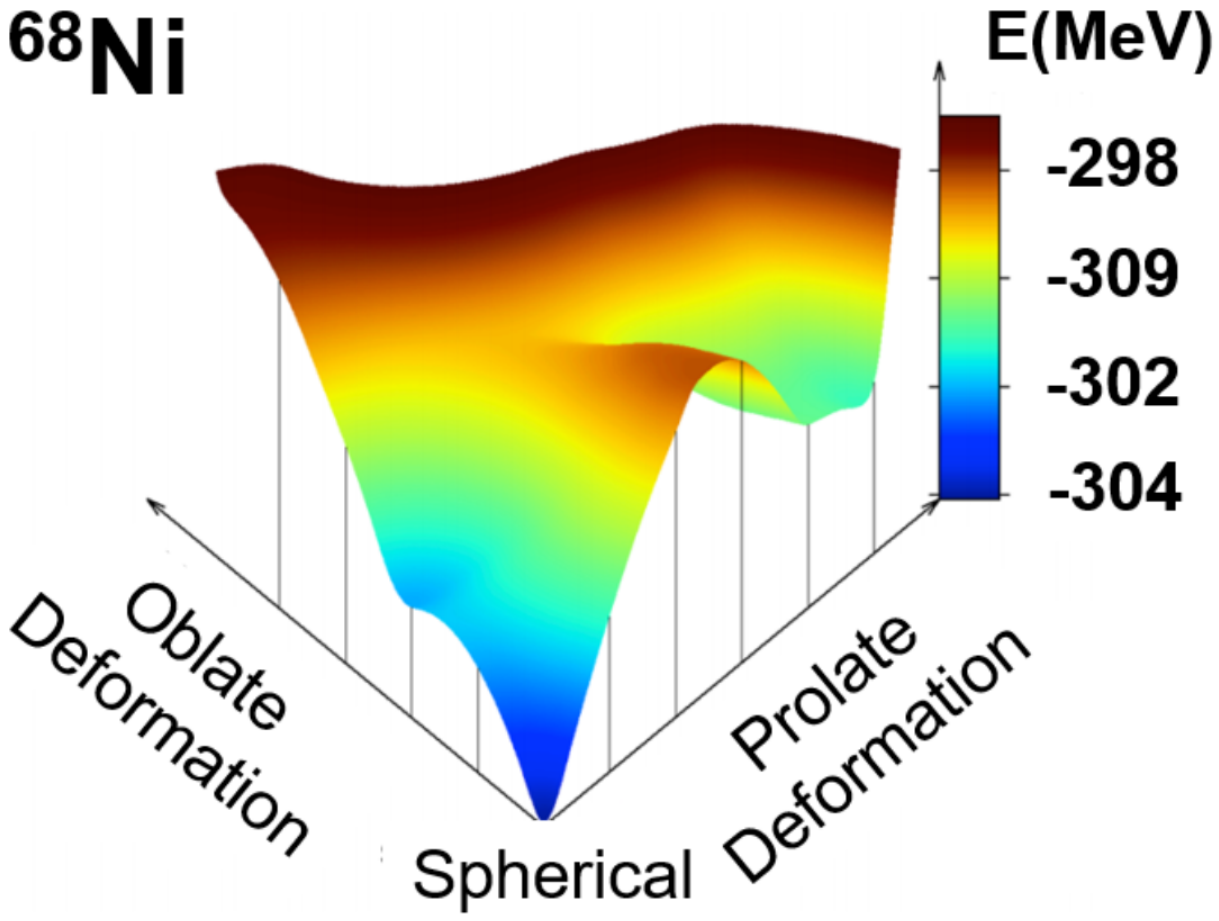

Figure 1.4: Potential energy surface for ^{68}Ni calculated using Hartree-Fock calculations constrained by the quadrupole moment. The three minima in the potential energy surface are associated with spherical, oblate, and prolate deformed 0^+ states. Figure adapted from Ref. [1].

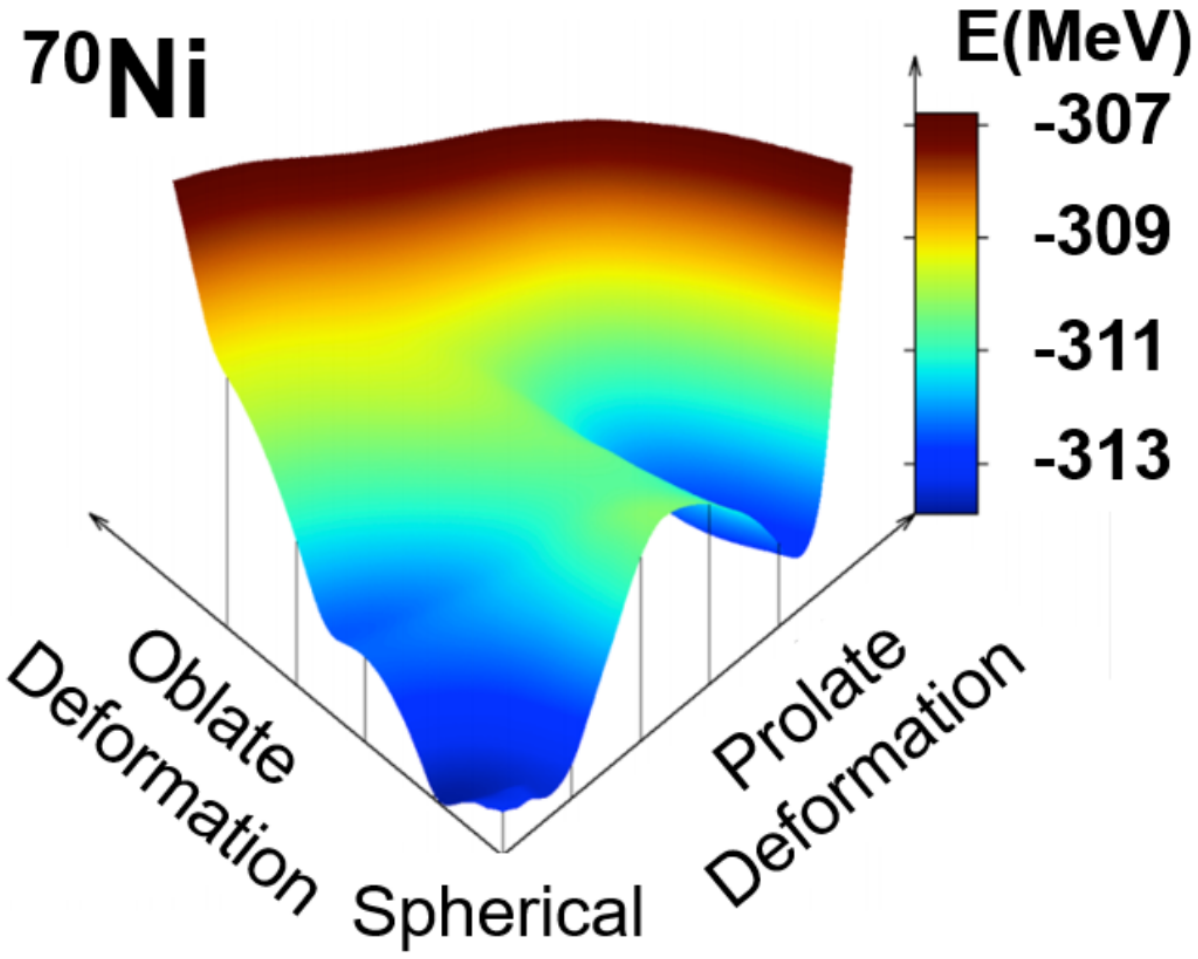

Figure 1.5: Potential energy surface for ^{70}Ni calculated using Hartree-Fock calculations constrained by the quadrupole moment. There is a considerable deepening of the prolate minimum in ^{70}Ni compared to ^{68}Ni, which is shown in Fig. 1.4. Figure adapted from Ref. [2].

Considerably less is known concerning shape coexistence in ^{70}Ni. Monte Carlo shell-model calculations [16] predict both that the ground state of ^{70}Ni is weakly oblate, and that the prolate deformed level drops from 2.5 MeV in ^{68}Ni to around 1.5 MeV in ^{70}Ni, highlighting the effect of shell evolution [16] when adding only a couple nucleons. Looking at potential energy surfaces calculated using Hartree-Fock calculations [1, 2, 16] constrained by the quadrupole moment determined from the Monte Carlo shell model Hamiltonian, there is a clear deepening of the minima in the potential energy surface in ^{70}Ni in Fig. 1.5 compared

to ^{68}Ni in Fig. 1.4. Ref. [18] reported the observation of a (0_2^+), 1567-keV level, possibly corresponding to the predicted prolate 0^+ state.

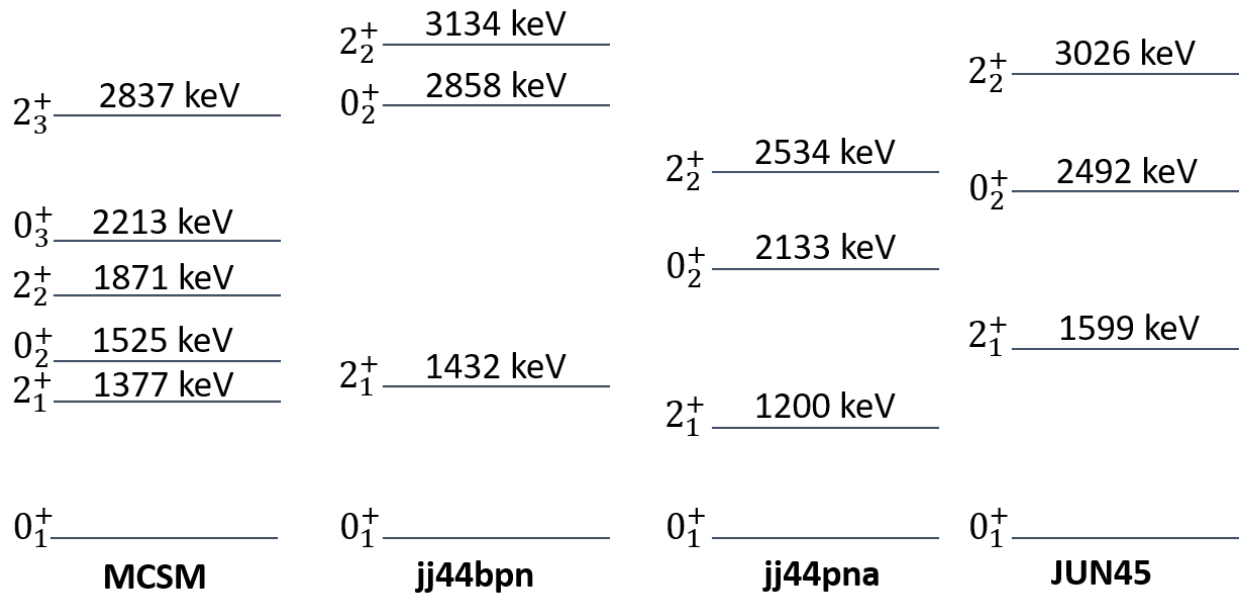

Figure 1.6: Results of shell-model calculations from Ref. [3] using the Monte Carlo shell model (MCSM) [4] with the full proton and neutron $fpg_{9/2}d_{5/2}$ model space compared to results using traditional shell-model calculations utilizing only the neutron $f_{5/2}pg_{9/2}$ model space and effective interactions: jj44bpn [5], jj44pna [6], and JUN45 [7]. Only the 0^+ and 2^+ levels are shown for comparison.

A comparison between the predictions for the Monte Carlo shell model and traditional shell-model calculations utilizing a number of different effective interactions is shown in Fig. 1.6, which is based on the shell-model calculations discussed in Ref. [3]. The Monte Carlo shell model is able to utilize the full proton and neutron $fpg_{9/2}d_{5/2}$ model space in the calculation. For traditional shell-model calculations of ^{70}Ni, including cross-shell proton excitations requires diagonalizing intractably large matrices, and therefore the aforementioned calculations could only include neutron excitations to the $f_{5/2}pg_{9/2}$ orbitals. Unlike the Monte Carlo shell model, these traditional calculations were unable to predict the suspected prolate 0^+ state, nor the 1868-keV, 2_2^+ one, possibly suggesting that these states are

built on cross-shell proton excitations outside of the traditional model space. A predicted oblate 0^+ state at energies above 2 MeV from both traditional shell-model and Monte Carlo shell-model calculations has not yet been observed. It is important to note that the prolate shape of the structure in ^{70}Ni is suspected solely from shell-model calculations and cannot be currently inferred from any current experimental data.

Exploring the band structures, states of similar structure connected to each other by strong transitions, built atop shape-coexisting 0^+ states provides stringent tests for nuclear models due to the demanding configuration spaces and the inclusion of cross-shell excitations. This has been probed experimentally in ^{68}Ni, for example, by observing the β decay of ^{68}Co and measuring the lifetimes and branching ratios of transitions from the three 0^+ states associated with different shapes. Another experimental technique, nucleon knockout, has been used to probe cross-shell excitations in proton-magic nuclei in the past [24]. Here, the role of excitations across $Z = 28$ is explored using complementary one- and two-nucleon knockout reactions to determine the leading orbital configurations of excited states in ^{70}Ni.

In the direct one- and two-nucleon knockout experiment performed in this work, a projectile of interest impinges on a ^{9}Be target and one or two nucleons are removed, leaving the projectile-like residue as a spectator to the sudden collision [25]. One- and two-nucleon knockout provide a way of probing the single-particle configurations of excited states in nuclei. For example, by knocking out a proton from ^{71}Cu, excited states in ^{70}Ni associated with configurations involving excitations across the $Z = 28$ shell closure can be selectively populated, as the ^{70}Ni nucleus is, with some probability related to wavefunction overlaps, left in a configuration that corresponds to a one-particle one-hole proton excitation after the reaction. The use of knockout as a direct reaction to probe spectroscopic factors was not pursued here due to knockout from isomers that cannot be quantified event-by-event,

as well as to (1) mostly unknown or tentative final-state quantum numbers, to (2) complex associated configurations, and to (3) expected high level densities (see for example [26]). More details about these direct reactions can be found in Ref. [25]. Here, the focus is on the population of excited states in ^{70}Ni. By comparing the population of the different excited states, as measured through their characteristic γ-ray de-excitations, to the resulting populations following one-neutron knockout from ^{71}Ni, it is possible to determine which states are associated primarily with proton or neutron excitations. The aim of the present work was to probe the proton and neutron degrees of freedom in ^{70}Ni with complementary reactions, and more specifically to verify the role of cross-shell proton excitations in the configuration of states proposed as belonging to the predicted prolate structure in ^{70}Ni.

Chapter 2

Experimental details and detection systems

The experiment was performed at the National Superconducting Cyclotron Laboratory (NSCL) [27] at Michigan State University. An overview of the Coupled Cyclotron Facility at the NSCL, including the K500 and K1200 coupled cyclotrons as well as the A1900 fragment separator, is shown in Fig. 2.1.

2.1 Beam production

The production of the primary ^{76}Ge beam proceeds as follows. A germanium vapor is created by oven heating and then ionized in an electron cyclotron resonance (ECR) ion source, the Advanced Room TEMperature Ion Source (ARTEMIS) [28]. The ions are then injected into the K500 cyclotron. The primary ^{76}Ge beam was ionized to $^{76}Ge^{+12}$ before injection.

Cyclotrons take advantage of the circular motion of a particle moving perpendicular to a uniform magnetic field. A particle with momentum p and charge q moving in a magnetic field of strength B will trace out a circle of radius ρ, where:

$$\rho = \frac{p}{qB} \tag{2.1}$$

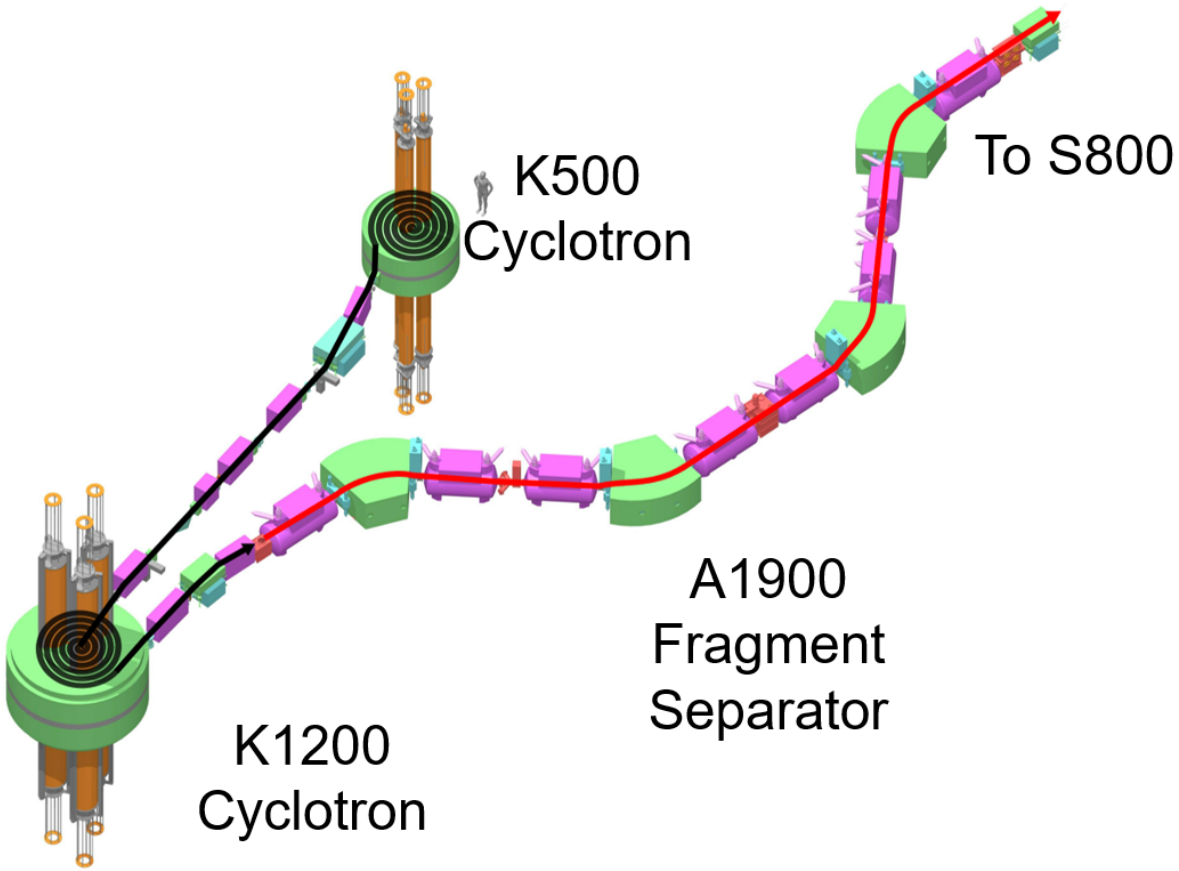

Figure 2.1: An overview of the layout for the Coupled Cyclotron Facility at Michigan State University, including the K500-K1200 coupled cyclotrons and the A1900 fragment separator.

A cyclotron is composed of pairs of "dees", copper electrodes surrounded by a superconducting electromagnet. A magnetic field serves to confine the particle along a circle of radius ρ and a radio-frequency electric field accelerates the particle as it crosses a gap between the dees. As the particle gains energy, its momentum p increases and it spirals outward from its point of injection at the center of the cyclotron.

Through this process, the ions will eventually reach the maximum energy obtainable from the K500 cyclotron and will be extracted and transported to the entrance point at the center of the K1200 cyclotron. Following acceleration in the K500 cyclotron, the $^{76}Ge^{+12}$ particles reached 11.6 MeV/nucleon. At the entrance of the K1200 cyclotron, the accelerated

ions strike a thin carbon "stripper" foil that further ionizes the particle; i.e., the charge q becomes larger, which by Eqn. 2.1 results in higher achievable energies. After striking the stripper foil, the $^{76}Ge^{+30}$ particles are accelerated to 130 MeV/nucleon in the K1200 cyclotron, undergoing the same process as in the K500 cyclotron.

The $^{76}Ge^{+30}$ primary beam then impinged on a thick 399 mg/cm^2 ^{9}Be production target, producing a cocktail of different fully-stripped ions including ^{71}Cu, ^{71}Ni, and ^{72}Zn, referred to as secondary beam, through projectile fragmentation. To select components of interest from the secondary cocktail beam, the A1900 fragment separator was utilized [29].

The A1900 fragment separator is composed of 24 quadrupole magnets and four 45° dipoles. It separates the fragments using a $B\rho - \Delta E - B\rho$ technique, where $B\rho = \frac{p}{q}$ is the magnetic rigidity. The magnetic rigidity allows selecting the particles of interest, because only those within a small range of momentum-to-charge ratio can pass through the dipole magnets based on the fixed radius of curvature of the beam line element ρ and the selected magnetic field strength B. Only particles with similar $\frac{p}{q} = \frac{\gamma m v}{q}$, where γ is the Lorentz factor, m is the particle mass, and v is the velocity, will pass through the selection process. Therefore, further beam purification is necessary to remove particles of similar momentum-to-charge ratios. One way this is accomplished is through several slits located both in the focal plane and the image points of the A1900, which can be partially closed to further limit the range of accepted momenta. An aluminum wedge degrader with an areal density of 300 mg/cm^2 located at the mid-acceptance position of the A1900 fragment separator was also used to further purify the secondary beam cocktails. Ions striking this wedge will lose differing amounts of energy based on the Bethe formula:

$$-\frac{dE}{dx} = \frac{4\pi e^4 n_e Z^2}{m_e \beta^2}\left[\ln\left(\frac{2m_e\gamma^2\beta^2}{I}\right) - \beta^2\right]. \tag{2.2}$$

where e is the elementary charge constant, n_e is the degrader's electron number density, m_e is the mass of the electron, $\beta = \frac{v}{c}$ is the ratio of the ion velocity v to the speed of light c, and I is the average excitation energy of the degrader material. This means that particles with different atomic numbers Z will exit the degrader with significantly different energies due to the Z^2 term in Eqn. 2.2.

Following the wedge degrader, there is another $B\rho$ selection process using the final two dipoles of the A1900 fragment separator that functions in the same manner as the first stage. The momentum acceptances for the different secondary beams of interest were limited by slits to 1.0%, 2.0%, and 0.5% for the ^{71}Cu, ^{71}Ni, and ^{72}Zn secondary-beam settings, respectively.

2.2 The S800 magnetic spectrograph

The separated fragments of interest were delivered from the A1900 through the transfer hall to the analysis line of the high-resolution, high-acceptance S800 magnetic spectrograph [30], shown in Fig. 2.2. The spectrograph is an optical system for charged particles that bends and focuses ions in a way analogous to the way lenses and prisms act on light [31].

The S800 is composed of two main parts: the analysis line, which delivers the beam from the transfer hall to the S800 target position, and the spectrograph itself. The analysis line is composed of four dipoles, five sets of quadrupole triplets, one quadrupole doublet, and four sextupoles [31]. The dipoles bend ion trajectories, the quadrupoles focus them, and the sextupoles serve to correct higher-order aberrations. At the beginning of the analysis line is the object position of the S800, where a thin plastic scintillator is located. This scintillator

is used for time-of-flight measurements.

At the target position of the spectrograph, fragments struck a thin ^{9}Be reaction target of thickness 100 mg/cm^2 for the one-proton knockout reaction or 188 mg/cm^2 for the one-neutron and two-proton knockout reactions. The analysis beam line was operated in focus mode [30].

At the entrance to the spectrograph is a quadrupole doublet that focuses the beam, which is then directed into the S800 focal plane using two large dipole magnets. Similar to the discussion of the A1900 fragment separator, the dipoles of the S800 spectrograph are used to bend charged-particle trajectories into the focal plane based on their magnetic rigidity. The magnetic field strength of the dipoles is adjusted to spatially center the reaction products of interest in the focal plane. The detectors in the S800 focal plane [32] include: two cathode-readout drift chambers (CRDCs) used to determine the position and trajectory of the particles entering the focal plane, an ionization chamber used to measure energy loss of the ions for particle Z identification, a thin plastic scintillator called the E1 scintillator that enabled measurements of a particle's time of flight and served as the particle trigger, and a CsI(Na) array [33] that was used in this work to detect decays from long-lived states of ions embedded into an aluminum plate directly in front of it.

The different detection systems in the S800 focal plane enabled trajectory reconstruction, particle identification, and isomer detection, and will be discussed in more detail in the following sections.

2.2.1 Particle identification

To identify components of the incoming cocktail beam, time of flight was measured between scintillators placed at the object position of the S800 (obj) and at the focal plane of the A1900

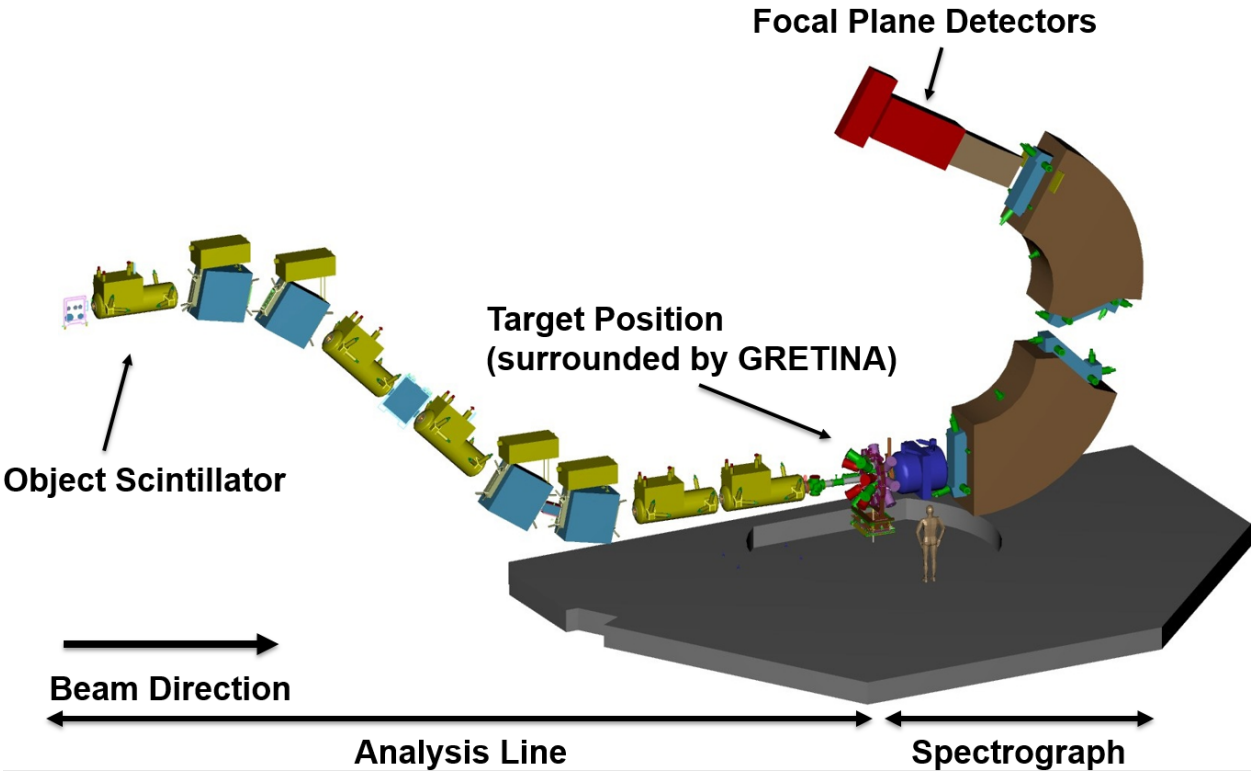

Figure 2.2: The secondary cocktail beams were delivered to the S800 spectrograph, pictured here.

(xfp) to the E1 scintillator in the S800 focal plane. Because ions entering the S800 focal plane have been selected based on their magnetic rigidity $B\rho = \frac{\gamma m v}{q}$, the mass-to-charge ratio $\frac{m}{q}$ is inversely proportional to the velocity v assuming a fixed flight path through the S800. Therefore, the time of flight is proportional to the mass-to-charge ratio $\frac{m}{q}$. The time-of-flight difference xfp-obj is sensitive to the mass of the incoming beam.

When attempting to identify the outgoing reaction products, the time-of-flight difference obj-E1 is utilized. It is important to correct for the correlation between the obj-E1 time-of-flight difference and the angle and position in the S800 focal plane, as the time of flight being proportional to the mass-to-charge ratio depends on the assumption of a fixed flight path ρ through the spectrograph. In the case where the reaction products are fully stripped, as is the case in this work, the mass-to-charge ratio $\frac{m}{q}$ is equivalent to $\frac{A}{Z}$, where A is

the mass number and Z is the atomic number of the ion. Using the time-of-flight difference outgoing reaction products can be separated by $\frac{A}{Z}$, but this is not sufficient to identify specific reaction products. Therefore, a gas-filled ionization chamber [32] is utilized to measure the energy-loss ΔE of the reaction products in the S800 focal plane. The ionization chamber is filled with a P10 gas and is partitioned into 16 1-inch anode segments. When the ions enters the ionization chamber, it loses energy based on the Bethe formula (see Eqn. 2.2) proportional to Z^2, ionizing the gas along the particle track and causing the electrons to drift towards the anodes. By plotting the energy deposited in the ion chamber ($\propto Z^2$) against the corrected time of flight ($\propto \frac{A}{Z}$), it is possible to discriminate between different outgoing reaction products. This is the standard $\Delta E - ToF$ technique.

2.2.2 Trajectory reconstruction

As noted in the previous section, the angles and positions of particles in the focal plane are crucial for outgoing particle identification. Furthermore, based on this angle and position information, the trajectory of a fragment can be reconstructed enabling the determination of its dispersive (ata) and non-dispersive (bta) angles, non-dispersive position (yta), and momentum (measured as the kinetic energy, dta) at the target position. While this momentum information is essential in many experiments for obtaining momentum distributions [34], here the reconstructed trajectories will play an important role in the Doppler-shift correction discussed in detail in Chapter 3.

Trajectory reconstruction is accomplished using position information from two position-sensitive cathode-readout drift chambers (CRDCs) [32] in the S800 focal plane. The CRDCs are separated by about 1 m. The CRDCs provide information about the angle and position of the particle in the focal plane of the S800. Particles passing through the CRDC ionize the gas,

causing electrons to drift towards the anode wire due to an applied voltage. The drift time of the electrons to the anode determines the y position in each CRDC, while the distribution of induced charge on the cathode pads determines the x position. Position information is calibrated using a thick mask with holes and slits drilled into it at known positions, so that particles can only pass through the holes and slits. The calibrated spectrum for the downstream CRDC is shown in Fig. 2.3. By using two separate CRDCs, it is possible to determine the dispersive (afp) and non-dispersive (bfp) angles in the focal plane from the measured positions.

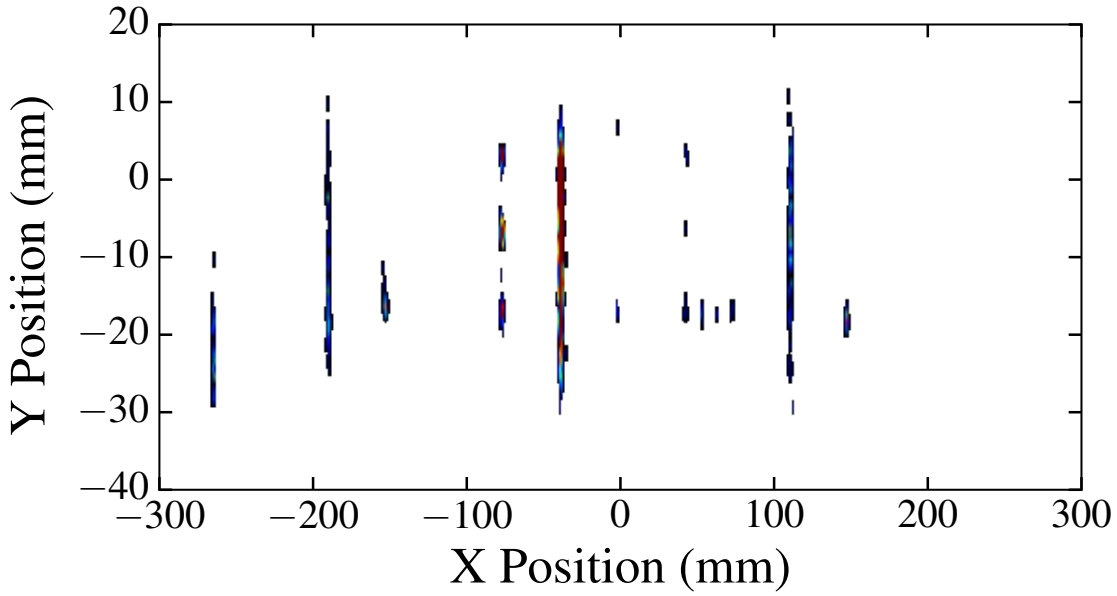

Figure 2.3: Calibrated mask run for the downstream CRDC used to determine the knockout residue's position in the focal plane. Note that the non-dispersive position is shifted so that it is centered on the knockout residue of interest, rather than the center of the focal plane.

An inverse map generated with the ion optics code COSY Infinity [35], which takes into account the magnet settings of the S800, is used to convert the quantities determined in

the focal plane (xfp, yfp, afp, bfp) to the previously mentioned ones at the target position (ata, bta, yta, dta) through ray tracing. Note that the dta value is the difference between the kinetic energy of the particle and the kinetic energy of a particle that would enter the center of the focal plane. The determination of the beam trajectory at the target position is important for Doppler reconstruction of γ rays emitted in-flight.

2.2.3 Isomer detection

Because the experiments require the detection of γ rays emitted from nuclei moving at substantial fractions of the speed of light, in contrast to those that implant the nuclei of interest in some material, the identification of long-lived excited states is difficult. These so-called isomeric states arise from a number of different factors related to nuclear structure; e.g., differences between the electric quadrupole properties of the excited states and the ground states as in the case of shape coexistence or large angular-momentum differences can lead to such behavior. Assuming a flight path through the spectrograph of about 15 m, nuclei with velocities $v \approx 0.4c$ will have a flight time of roughly 125 ns. Therefore, it would be necessary to measure de-excitations towards the end of the reaction product's flight path in the focal plane to identify the decays from states with lifetimes $\tau \geq 125$ ns.

To attempt the identification of such states, after the beam-like reaction residues pass the E1 scintillator functioning as the particle trigger, they are embedded in a 6.35 mm thick aluminum plate at a distance of 10.5 cm from a CsI(Na) hodoscope array [33], composed of 32 closely packed CsI(Na) crystals coupled to photomultiplier tubes. The energy resolution typical of CsI(Na) scintillators is roughly 6% FWHM for a ^{137}Cs source. The inclusion of the aluminum plate for implanting the reaction products is known as the IsoTagger configuration [36].

The IsoTagger configuration enables the identification of decays from states of the knock-out residues with lifetimes between 100 ns and several ms, such as the 2861-keV level (τ = 335(1) ns [11]) in ^{70}Ni. In the range 50 keV to 1.9 MeV, the simulated full-energy peak efficiency in this setup ranges between 6% and 16% based on the energy of the peak assuming γ-ray emission from the center of the aluminum plate and an implantation profile consistent with expectations for one nucleon removal reactions [36].

2.3 In-beam γ-ray spectroscopy with GRETINA

The purpose of this experiment is to measure the population of excited states in ^{70}Ni. As these states only decay by emitting a γ ray, this can be accomplished by measuring the intensity of γ rays tagging the de-excitations. To this end, the Gamma-Ray Energy Tracking In-beam Nuclear Array (GRETINA) [37], which in this experiment was composed of nine cryostats each housing four 36-fold segmented high-purity germanium crystals, surrounded the target position of the S800 magnetic spectrograph and was used for in-flight γ-ray detection. The array was arranged in the NSCL standard configuration, which means the four positions at 58° relative to the beam axis were populated, and the remaining detectors were at 90°. A photograph of GRETINA detectors arranged around the S800 target position in front of the entrance quadrupole of the spectrograph is shown in Fig. 2.4. Note that there are ten detectors shown here, one of which in the 90° ring was not available yet for this experiment.

Figure 2.4: Photograph of GRETINA surrounding the target position of the S800 in front of the entrance quadrupole of the spectrograph. The beam pipe is removed, and the beam direction would be into the page. Note that there was one less detector at 90° utilized for this experiment as compared to the photograph, as the tenth was not yet available.

2.3.1 The Gamma-Ray Energy Tracking In-Beam Nuclear Array (GRETINA)

High-purity germanium detectors are semiconductor devices used for the detection of γ rays that provide the best possible intrinsic energy resolution of about 0.2% FWHM at 1 MeV for efficient γ-ray detection. Because γ rays are not charged, they cause no direct ionization of a material. Therefore, it is necessary for the γ ray to go undergo some interaction with the detection medium to produce energetic electrons, which are then detected and used to reconstruct the energy of the initial γ ray. The three important types of interaction for γ rays are: photoelectric absorption, Compton scattering, and pair production. As the cross section for photoelectric absorption is small for γ rays with energies greater than a few 100 keV compared with Compton scattering, a γ ray undergoes multiple interactions before being fully absorbed within a detector; e.g., multiple Compton scatters followed by photoelectric absorption. Because of this, there are often multiple *interaction points* within a detector for every γ ray that is detected as a full-energy-peak event in a spectrum.

The main aim of GRETINA is to measure these interaction points along with the energy deposited at each point. The segmentation of the detectors makes it possible to determine the sub-volume in a crystal where the γ-ray interactions occurred. By analyzing the detected signal shapes, which are governed by the charge collection process, it is possible to achieve sub-segment resolution. An interaction position in a segment is associated with a unique set of signals observed on the hit segment contact, and via mirror charges on neighboring segment electrodes as well. The unique set of signals is known as a *signal basis*. Because there are several interaction points per event, a superposition of energy-scaled basis signals are measured. To disentangle the different interaction points along with deposited energies at

each point, the measured signals from all 36 segments are fit against the signal basis, and up to two interactions per segment are allowed. This process is known as *signal decomposition*, and is accomplished online utilizing the GRETINA computer farm, which is capable of processing 30,000 γ rays per second.

Measuring the interaction points and their associated deposited energies makes it possible to perform γ-ray tracking. Using the kinematics of Compton scattering and the photoelectric effect, γ-ray tracking makes it possible to determine whether a γ ray was completely absorbed. This means it is feasible to eventually have a sphere providing full 4π coverage with germanium without sacrificing the peak-to-total ratio, i.e. the ratio of counts in the full-energy peak to the number of counts in the sum of the full-energy peak and the Compton continuum. Although in the case of fast-beam experiments this is less of a concern due to the relatively low γ-ray multiplicity for events, the number of GRETINA detectors provides a large efficiency. In addition, the compactness of GRETINA detectors downstream of the target is advantageous because of the forward focusing of γ rays emitted in flight at $\frac{v}{c} > 30\%$ due to the Lorentz boost [38].

2.3.2 Doppler reconstruction

Because the γ rays are emitted from projectiles moving at substantial fractions of the speed of light, they are detected in the laboratory frame with a significant Doppler shift. To account for this, a Doppler reconstruction is performed to determine the energy of the γ ray in the projectile frame (E_{p}) from the detected γ-ray energy in the lab frame E_{lab}:

$$E_{\mathrm{p}} = E_{\mathrm{lab}} \frac{1 - \frac{v}{c}\cos\theta}{\sqrt{1 - \frac{v^2}{c^2}}}, \tag{2.3}$$

where $\frac{v}{c}$ is the velocity of the projectile emitting the γ ray and θ is the γ-ray emission angle. To properly determine the Doppler correction angle (θ in Eqn. 2.3) it is necessary to determine the first interaction position in GRETINA, which is capable of providing interaction points within $\sigma \approx 2$ mm. To accomplish this, the assumption is that the first interaction point is the *main interaction point*, which is the interaction point with the largest energy deposition. The consequence of selecting the wrong first interaction point will be discussed later.

The ability to reconstruct the energy of the γ ray is limited by knowledge of the emitting particle's velocity v and the detection angle θ from Eqn. 2.3. The reconstruction velocity v is typically determined using the velocity at the mid-target position. The uncertainty in the velocity determination is due to the thickness of the reaction target, because one cannot determine the exact distance through the target at which the particle decays. The *dta* value from the spectrograph only provides information on the kinetic energy *after* the target. Therefore, as the decay can happen at any point in the target, there is an uncertainty due to the energy loss in the target. Consider the knockout of one-neutron from ^{71}Ni to ^{70}Ni using the 188 mg/cm^2 ^{9}Be target. The energy after the target is measured based on the magnetic rigidity of the spectrograph to be 66.8 MeV/nucleon. Therefore, the ^{71}Ni decays at some velocity between $v/c = 0.394$ and $v/c = 0.3597$, a 9% effect.

When a thinner target is used, such as the 100 mg/cm^2 ^{9}Be target used for the one-proton knockout setting, the largest contributor to the uncertainty in determining the energy of the γ ray is the determination of the emission angle (θ in Eqn. 2.3). As mentioned previously, the emission angle depends on the determination of the first interaction point, which is assumed to be the interaction point with the largest energy deposition. Assuming a typical distance between the target and GRETINA of 200 mm, the $\sigma = 2$ mm position resolution

of GRETINA results in an angular resolution of $\sigma \approx 10$ mrad. This is much larger than the few mrad uncertainty in the reconstruction of the particle trajectory using the S800. The emission angle determination can be further refined by accounting for the non-dispersive position of the particle at the target (yta) determined with the inverse map.

Finally, there is another relatively small effect due to the incoming beam being offset from the optical beam axis. This can lead to the angle θ in Eqn. 2.3 being improperly shifted by about 3 mrad in the worst case. [38]. The forward detectors are more sensitive to this effect than those at 90°, because the nearly-perpendicular emission angle for the 90° detectors are not sensitive to small shifts in the xy-position of the beam on the target. All detectors, however, would be sensitive to any beam angle offset from the optical axis. This is corrected by systematically varying the beam spot offset (x_0, y_0) and beam angle offset (a_0, b_0) until the measured centroids of individual crystals align. A discussion of corrections to manage the aforementioned sources of uncertainty will be presented with examples in Chapter 3.

2.3.3 Nearest-neighbor add-back

It is common in GRETINA for neighboring crystals to detect interactions within the same event, and this is likely caused by a single γ ray scattering from one crystal into the next. This would lead to increased Compton background in a γ-ray *singles* spectrum, which is simply the sum of the spectra from the central core of each individual crystal. The full energy of the γ ray can be recovered by adding together the energy from the neighboring crystals. This improves both the efficiency and the peak-to-total ratio as the two Compton background γ rays are now part of the full-energy peak.

This process of recovering the full energy of γ rays scattered between crystals is known as *nearest-neighbor add-back*. Two crystals are considered nearest neighbors if they share a

common boundary, whether they are in the same cryostat or in adjacent GRETINA modules. In this work, add-back is accomplished by first sorting all interaction points in an event by energy. Then, each interaction point is compared based on their distance and time difference. If two interaction points lie within 80 mm and occurred within 440 ns, they are summed, taking the position of the summed interaction points as that of the one associated with a higher energy deposition.

Improving the peak-to-total ratio is particularly helpful for determining $\gamma\gamma$ coincidence relationships, used in this work to place transitions into the level scheme, due to the decrease in Compton scattered γ rays in the background when attempting to gate on individual transitions. For example, if one γ ray in a cascade scatters between crystals, it could lead to misidentifying artifacts of this process as peaks in the $\gamma\gamma$ *coincidence spectrum*. A $\gamma\gamma$ coincidence spectrum for a specific γ ray is a spectrum containing all other γ rays observed within the same events as that γ ray.

While nearest-neighbor add-back could be used to determine transition intensities, there are number of difficulties; e.g., determining the absolute efficiency gain is subject to significant systematic uncertainties, as add-back factors to scale the efficiency can only be reliably determined for events with γ-ray multiplicity = 1 due to the possibility of summing two coincident γ rays, particularly in this naive approach to add-back described above.

2.3.4 Simulating GRETINA's peak response

The peak response was an important component of the fitting template used to extract the peak areas from the spectra, particularly due to the presence of multiple, unresolvable peaks in the spectra observed in this experiment. To this end, GEANT4 simulations using the UCGretina framework [39] were utilized. The peak responses of both the observed γ rays

in the Doppler-corrected γ-ray spectra, and the stopped background lines, which can be observed in the γ- spectra without a Doppler reconstruction, were simulated.

The simulation takes in to account: the geometry of GRETINA, including the segmentation of the detectors, the cryostats, and the mounting hemispheres, the target nucleus and target thickness, the aluminum beam pipe, the identity and energy of the incoming projectiles, as well as the identity, excitation energy, and lifetime of the outgoing reaction products. The inclusion of information concerning the target, incoming projectiles, and outgoing reaction products makes it possible to model the energy loss of the beam through the target, and therefore the resulting uncertainty in the velocity for the Doppler correction observed in the experiment due to the energy loss in the target. The reaction is modeled as a single-step excitation, producing the reaction residue in an excited state with the given excitation energy and lifetime. After the reaction, a new momentum vector is chosen for the particle, and the distance it travels until decay is obtained from a Monte Carlo simulation based on the lifetime of the excited state. The particle then continues to travel until it exits the target, at which point the trajectory is recorded in the same format as from the S800 spectrograph; i.e., as *ata*, *bta*, *dta*, and *yta*.

The simulation process is complicated by the manner in which GRETINA obtains interactions points, i.e., the signal decomposition process. While it is possible to determine exactly the interaction points in the simulation, in reality multiple interactions within a single segment are difficult for the decomposition process to distinguish. To approximate this in the simulation, all interaction points within a segment are aggregated within a defined packing radius. In these simulations, the packing radius is chosen to be 6 mm, so all interaction points determined in a single segment within 6 mm are combined into a single interaction point with the energy as the sum of the energies of the different interaction points and with

position determined by an energy-weighted averaging. The resulting interaction points are smeared based on the position resolution of GRETINA. In this analysis, the dependence of the position resolution on the energy of the detected γ ray was explored, which has been done previously for AGATA [40], the European γ-ray tracking detection array.

One important feature of the experimental data that is not directly reproduced in the simulated peak response is the existence of tails extending both towards lower and higher energies for peaks in the spectrum, a phenomena previously reported in Ref. [38]. This is clearly visible in Fig. 2.5, where a simulation utilizing the nominal position resolution of $\sigma = 2$ mm to smear the interaction points is unable to reproduce these tails when attempting to fit a 1368-keV transition from ^{24}Mg. This data comes from a measurement where the peak shape is entirely dominated by the uncertainty in the detection angle due to the use of a thin 100 mg/cm^2 target. It is clear that the simulated spectra is unable to reproduce the tails on the side of the peak. This suggests that the γ rays are reconstructed using the wrong θ in Eqn. 2.3. Some possible causes of this are selecting the wrong first interaction point or the complex decomposition process returning incorrect interaction points for some fraction of events. Reproducing the peak shapes was particularly important in this experiment as there were a number of regions of the experimental spectra where multiple peaks could not be resolved and intensity determination then relies on the modeling of the peaks within a doublet.

Therefore, to reproduce the peak shapes with the aim of handling these tails when fitting the full γ-ray spectrum to determine the peak areas, a strategy was devised where each peak was split into two components: a narrow component corresponding to the expected peak width, and a second, wider component, which would approximate the effect of the incorrectly determined angle. The two components were summed with an 80%-20% scaling for the

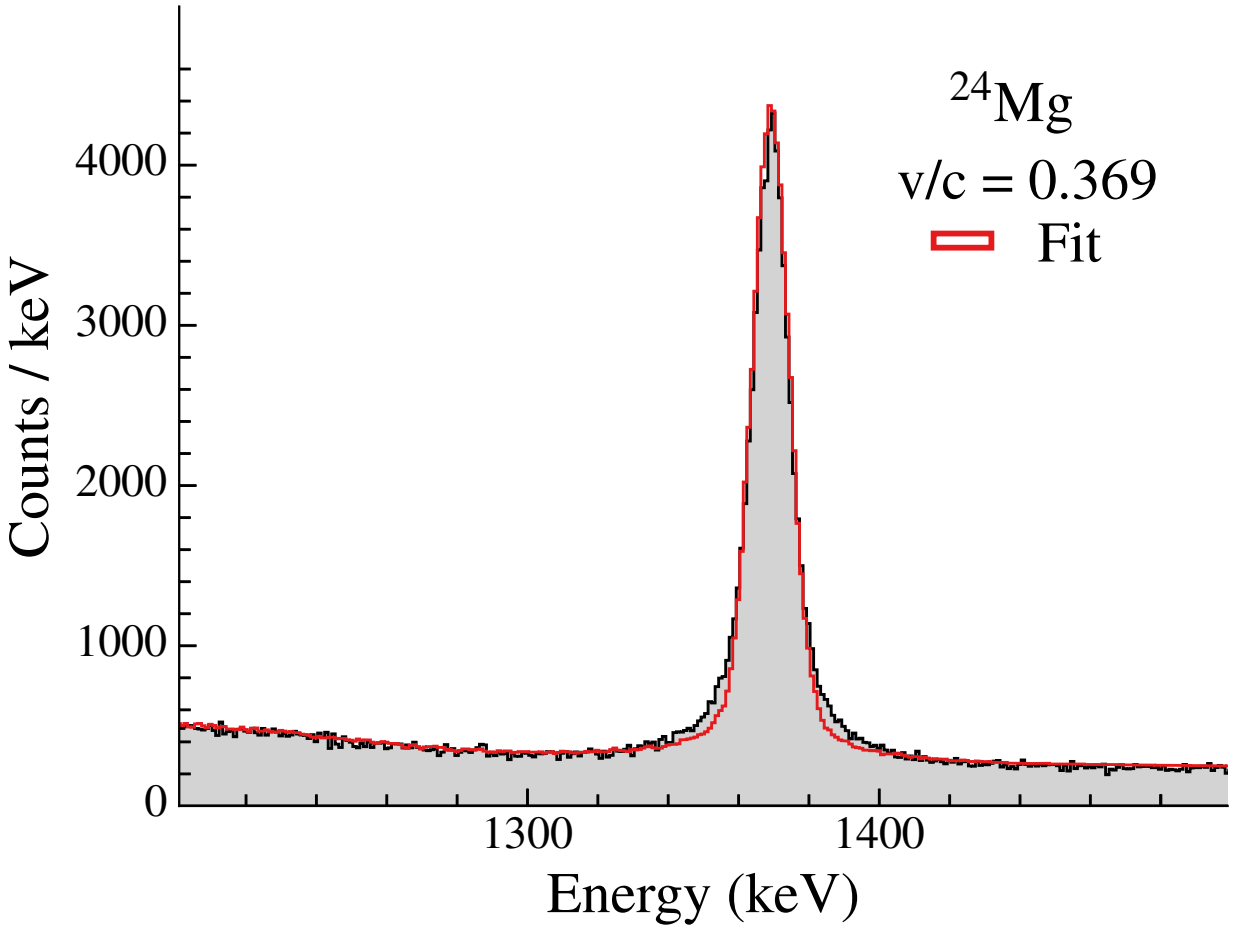

Figure 2.5: Fit with peak response determined from the GEANT4 simulation, assuming a position resolution of $\sigma = 2$ mm to smear the simulated interaction points. There are clear tails on the peak that are not reproduced by the simulation.

narrow and wide component, respectively. Varying the widths of the narrow component in the range 1.0 mm to 5.0 mm and the wide component in the range 5.1 mm to 7.5 mm, the value resulting in the best fit for this 1368-keV transition as measured by the χ^2-value was determined to be $\sigma = 2.0$ mm and $\sigma = 7.0$ mm for the narrow and wide components, respectively. This fit is shown in Fig. 2.6, and produced a factor of five improvement in terms of χ^2 compared to Fig. 2.5. Note that the fits were considerably more sensitive to the narrow component than the wide component, and the wide component was not observed to have an energy dependence.

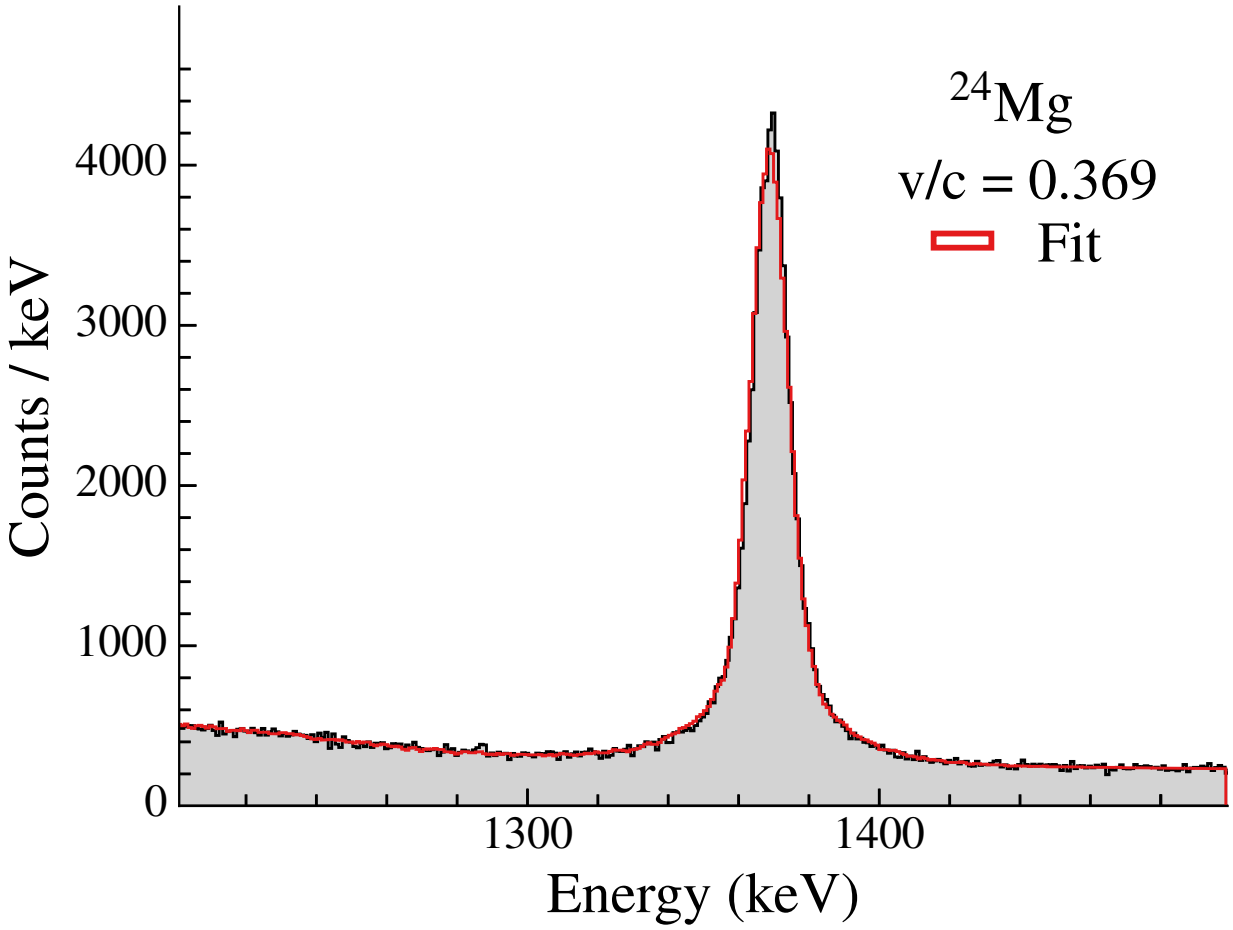

Figure 2.6: Fit with peak response determined from the GEANT4 simulation, assuming a position resolution of $\sigma = 2$ mm for the narrow component and a position resolution of $\sigma = 7$ mm for the wide component, which are added together in the ratio $80\% - 20\%$ as described in the text.

The energy dependence of the narrow component of the peak response was constrained by fitting GRETINA data from light nuclei (^{21}Ne, ^{23}Na, ^{24}Mg, ^{28}Si, and ^{32}S) on a 100 mg/cm^2 ^{9}Be target with well-separated peaks at different energies and varying the simulated position resolution of GRETINA, enabling the determination of the energy dependence of the peak widths as shown in Fig. 2.7. The use of data from light nuclei on such a thin target is advantageous, as it almost eliminates the uncertainty in the velocity determination and therefore improves the sensitivity to the position resolution in GRETINA. Unfortunately,

the fit in Fig. 2.7 is not well constrained in the region between 500-1200 keV; however, because the beams used in this experiment are considerably higher-Z than those used for the determination of the spatial resolution in Fig. 2.7, the greater energy loss in the target due to the Z^2 term in Eqn. 2.2 will cause the uncertainty in the velocity to be a more dominant contribution to the width than the uncertainty in the position resolution of GRETINA. Note that extrapolating to lower energies using this function does not work as the fit function increases exponentially. Instead the optimal width of the narrow component is assumed to remain constant below the 351-keV transition included in the fit.

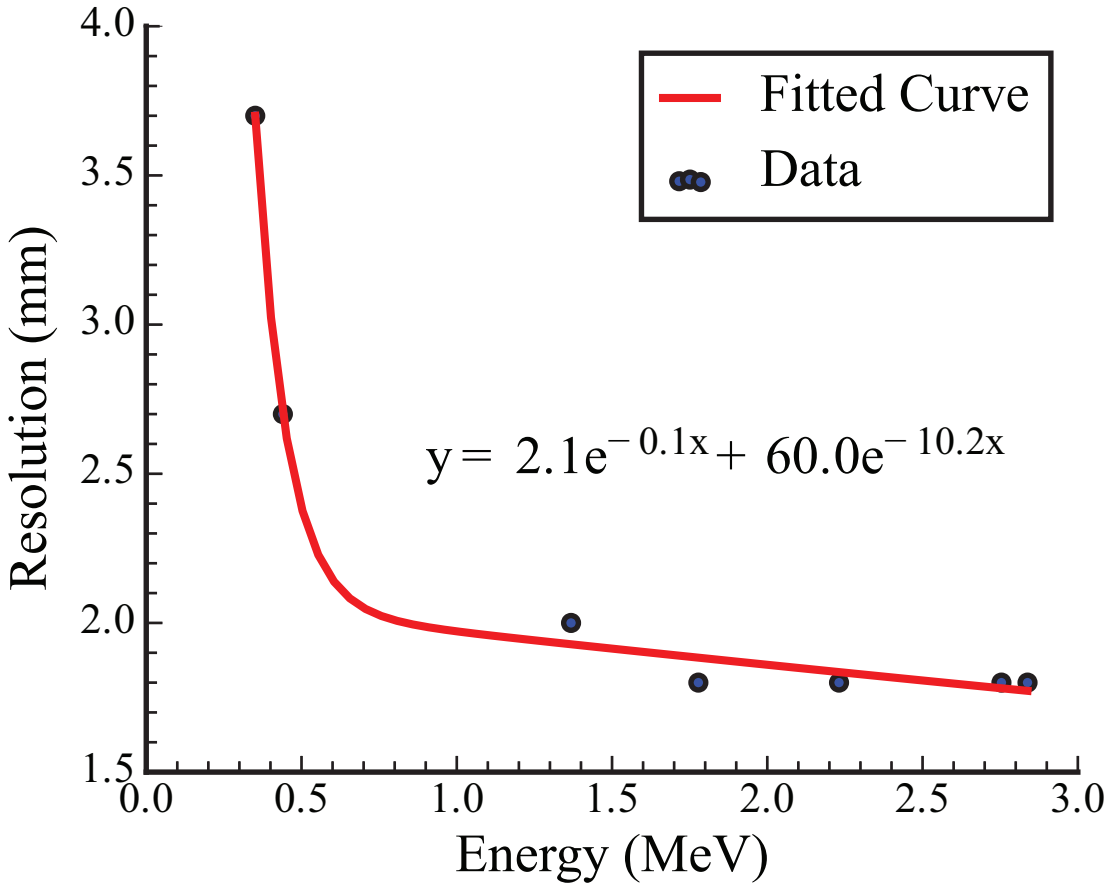

Figure 2.7: Determination of the position resolution for the narrow component of the peak response, as described in the text.

A caveat with this approach is that it causes one to overestimate the peak-to-total con-

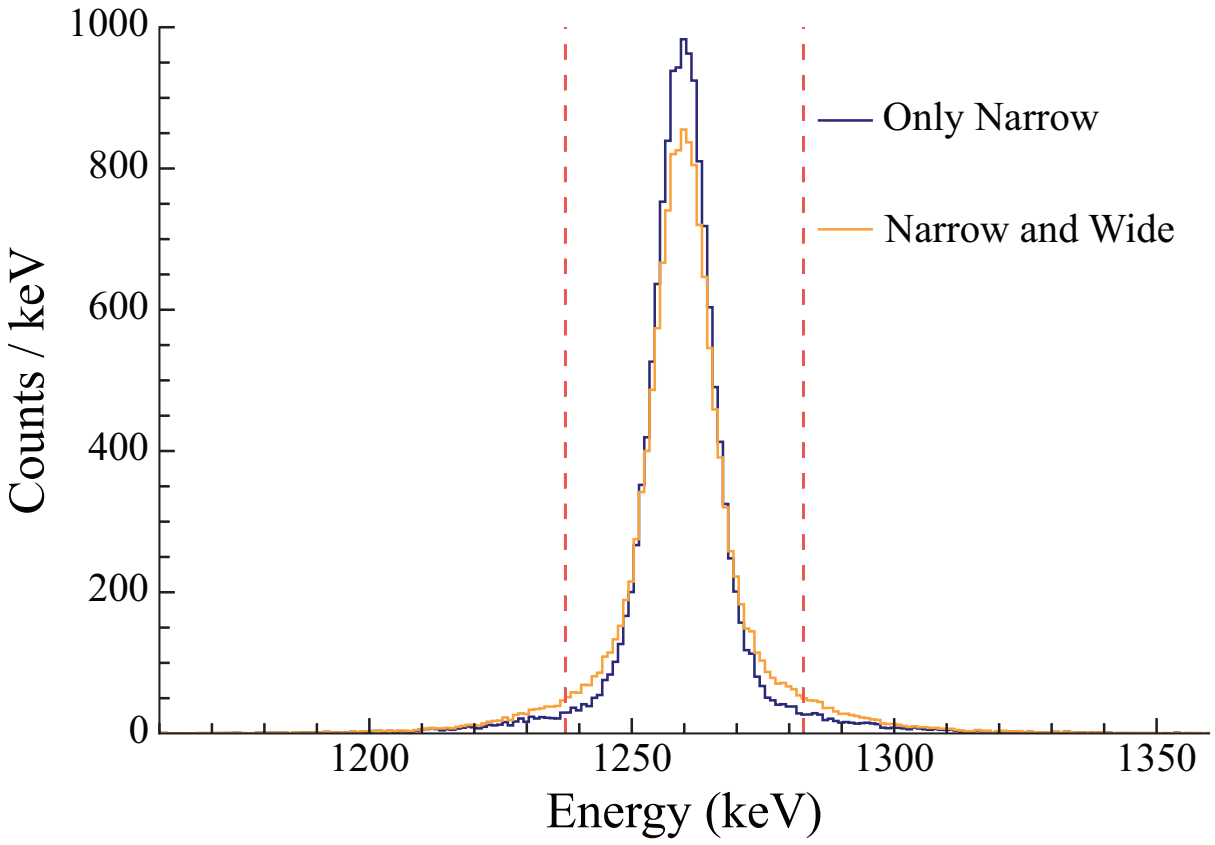

Figure 2.8: Comparing the simulated full-energy peak for the narrow component of the peak template and the one described in the text containing both a narrow and wide component combined with the ratio 80%-20%, respectively. The dashed lines show the region of integration to determine the peak areas in this work, which accounts for 95% of the area of the spectrum containing only the narrow component.

tribution for individual peaks. This is because counts that would traditionally be placed in the background are now able to be accounted for in the wide tails, as seen in Fig. 2.8, where a 1260-keV full-energy peak is shown using only a narrow component (blue) and both a narrow and wide component (tan). To account for this, the peaks fit to experimental data were integrated in a range around the centroid to avoid including background counts in the peak areas. This region was chosen to be 2 FWHM from the peak centroid in either direction, as shown by the dashes lines in Fig. 2.8, which recovers 95% of the intensity for the simulated full-energy peak if only the narrow component was included. Uncertainties from including

more or less of the fitted peak were included in the uncertainty estimates for all measured peak intensities discussed later in Chapter 4.

2.3.5 Lifetime effects on peak centroids

The lifetime of decaying states has a significant effect on the observed peak shapes and centroids for γ rays emitted in flight due to the sensitivity of the Doppler correction to the velocity and position of the emitter. While these effects are also important for prompt transitions, the use of a single velocity to optimize spectral quality when performing the Doppler reconstruction for spectra containing primarily prompt transitions means that the long-lived states will be Doppler corrected with a velocity that is too high. Longer-lived states decay at lower velocities than prompt transitions due to the on-average loss of more energy through interaction with more of the target material. Because the emission point will occur further along the trajectory for such states, the emission angle will be underestimated, leading to an underestimation of the transition energy for γ decays from isomeric states.

Consider the 188 mg/cm^2 ^{9}Be target, which is about 1 mm thick. Assuming a velocity of $\frac{v}{c} = 0.33$, the beam takes 10 ps to traverse the target. In this lifetime range, the uncertainty due to the lifetime is dominated by the uncertainty of the energy loss in the target. For lifetimes in the range 10-30 ps, the decay happens mostly after target, leading to a well-known velocity due to the *dta* measurement and an angle uncertainty comparable to the $\sigma \approx 10$ mrad uncertainty from the position resolution of GRETINA. For the range between ≈ 30 ps-1 ns, the angle plays a dominant role in the energy determination due to uncertainty concerning the decay position. Finally, for lifetimes longer than approximately 2 ns, the decay starts to happen in the S800 spectrograph.

For short lifetimes, on the order of $\tau < 100$ ps, the net effect is a shift of the peak centroids

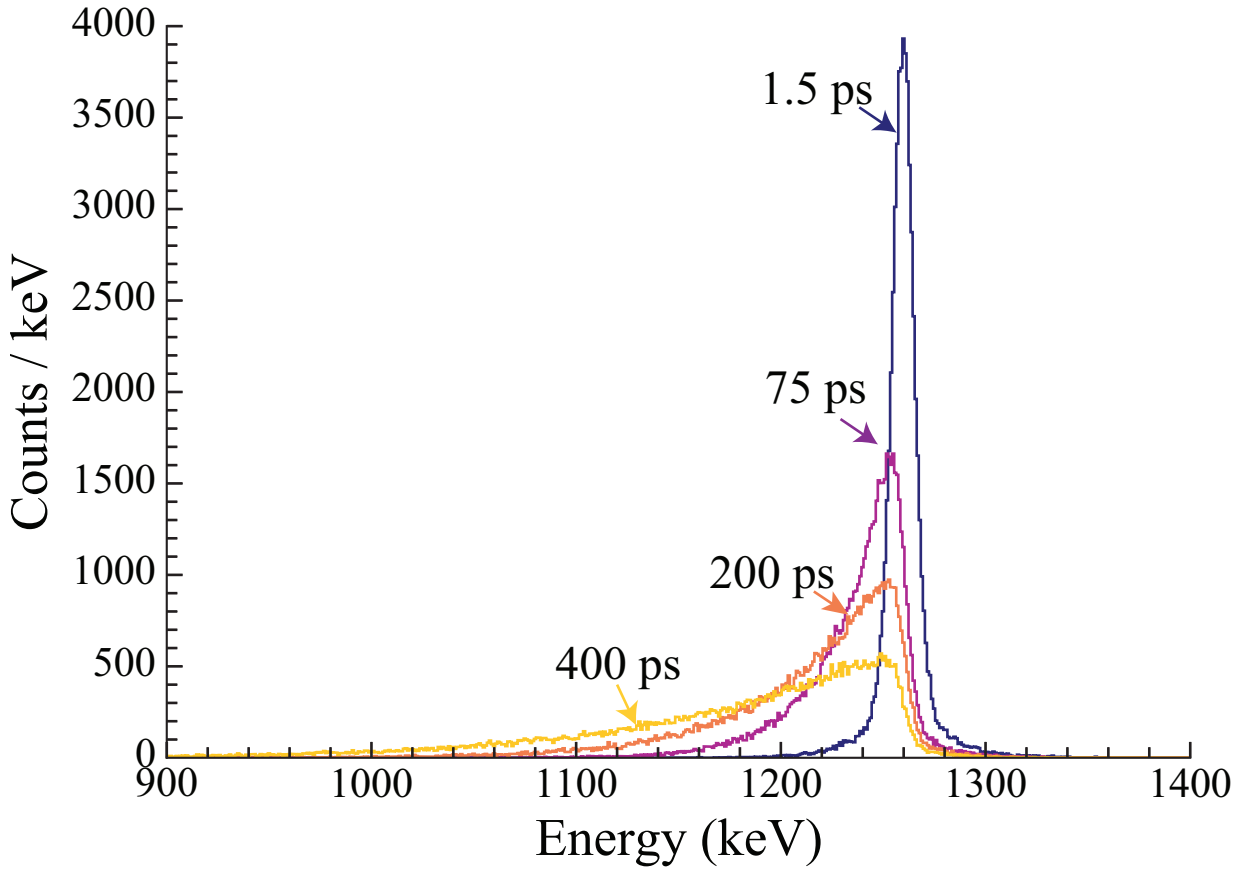

Figure 2.9: The full energy peak for a 1260-keV transition simulated with various different lifetimes. The peak is Doppler reconstructed using the expected velocity for the 1260-keV transition in ^{70}Ni, which has a known lifetime of $\tau = 1.5$ ps. There are clear shifts at relatively low lifetimes and the peaks become increasingly wider towards lower energies as the lifetime increases.

towards smaller values and a low-energy tail extending from the peak. Beyond $\tau \approx 100$ ps, the peak shape widens substantially. This is shown in Fig. 2.9, where a 1260-keV decay was simulated assuming a number of different lifetimes, and then Doppler-corrected as if it was the same lifetime ($\tau = 1.5$ ps [11]) as the 1260-keV state in ^{70}Ni. This change in peak shape and centroid position will be important to arguments later in Chapter 4.

2.3.6 Energy calibration and efficiency determination

To identify peaks in γ-ray spectra, it is important to perform an energy calibration. The energy calibration for GRETINA in this work was performed prior to the experiment using radioactive sources. It was set prior to the experiment for every segment and crystal, with the signal decomposition outputting calibrated energies.

Ultimately, after identifying peaks in the spectra, it was important to determine peak areas and then correct these for the detection efficiency to deduce the transition intensities. The quality of the spectra produced by GRETINA at the low γ-ray multiplicity for fast-beam experiments is sufficient to determine the peak areas for the detected γ rays. It is then possible to determine the γ-ray transition intensities from the experimental efficiency curve (see Figure 2 in Ref. [38]), which was determined using radioactive sources and was corrected here for the Lorentz boost using simulation. The γ-ray transition intensities determined in this work are all presented in Chapter 4.

Chapter 3

Data analysis: calibrations and corrections

In the following chapter, examples of the necessary corrections and calibrations mentioned in Chapter 2 will be discussed in more detail with specific examples from the analysis of the setting centered on incoming ^{71}Cu. The analysis proceeded in similar ways for the ^{9}Be(^{71}Ni, ^{70}Ni+γ)X and ^{9}Be(^{72}Zn, ^{70}Ni+γ)X settings.

3.1 Particle identification in the entrance and exit channel for the one-proton knockout setting

The following provides an example of the particle identification process for the one-proton knockout from ^{71}Cu to ^{70}Ni. The ^{71}Cu is delivered as part of a "cocktail" beam of 95% purity, with primary contaminants being ^{69}Ni and ^{73}Zn, and first must be identified. The incoming beam spectrum for the one-proton knockout reaction setting with a red contour drawn around the ^{71}Cu component for a subset of the experimental data is shown in Fig. 3.1. Plotting the *obj* and xfp flight times against each other separates the different constituents of the incoming beam by their velocity difference. Some of the ^{69}Ni and ^{73}Zn beam contaminants remain in this contour.

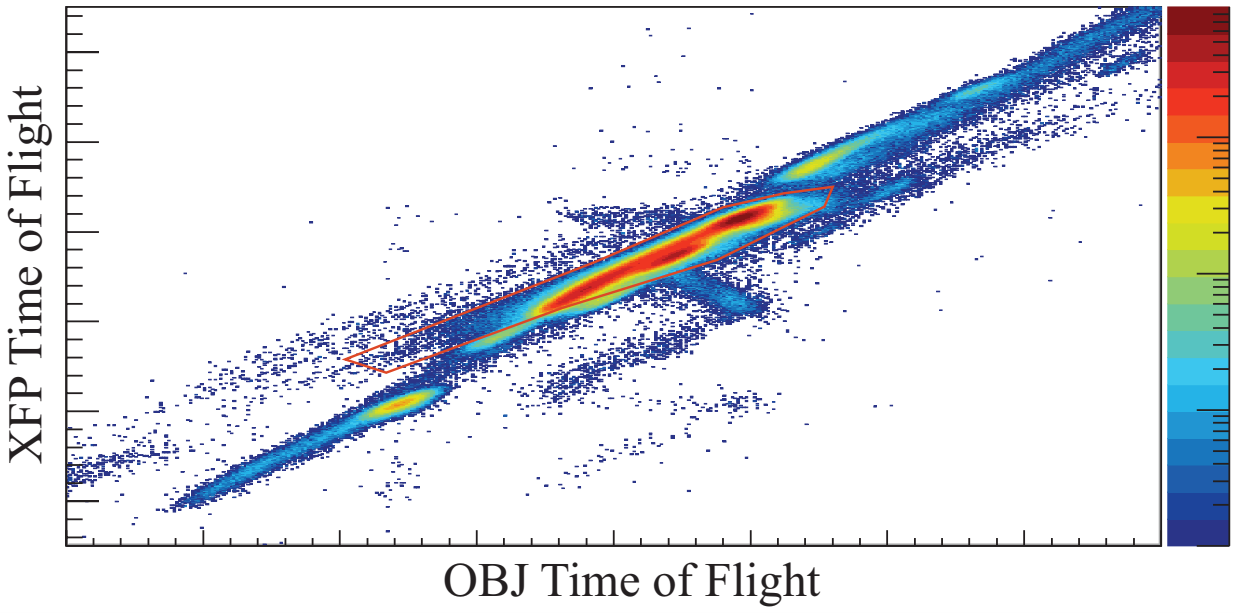

Figure 3.1: Incoming particle identification plot for the S800 setting centered on one-proton knockout from ^{71}Cu showing the xfp and obj time-of-flight distributions discussed in more detail in Section 2.2.1. Outlined in red is the contour around incoming ^{71}Cu projectiles. Also contained in the contour are some ^{69}Ni and ^{73}Zn incoming beam contaminants.

After identifying the incoming ^{71}Cu projectiles, the goal was to discern the ^{70}Ni knockout residues exiting the target from the other reaction products that enter the large-acceptance focal plane of the S800 spectrograph. To this end, the obj time of flight had to be corrected for the angle and position in the focal plane for each particle to be able to cleanly separate the outgoing beam components. This trajectory correction for events gated on ^{70}Ni projectile-like knockout residues and ^{71}Cu incoming projectiles is shown in Fig. 3.2. In this figure, the correlation between the obj-E1 time-of-flight difference and the position in the first CRDC (top) and angle in the focal plane (bottom) of the beam-like reaction product is shown. This correction accounts for the fact that particles that are, for example, on trajectories with larger angles will have a longer flight time. The corrected time-of-flight difference provides a measurement of $\frac{A}{Z}$ for completely stripped fragments in the spectrograph.

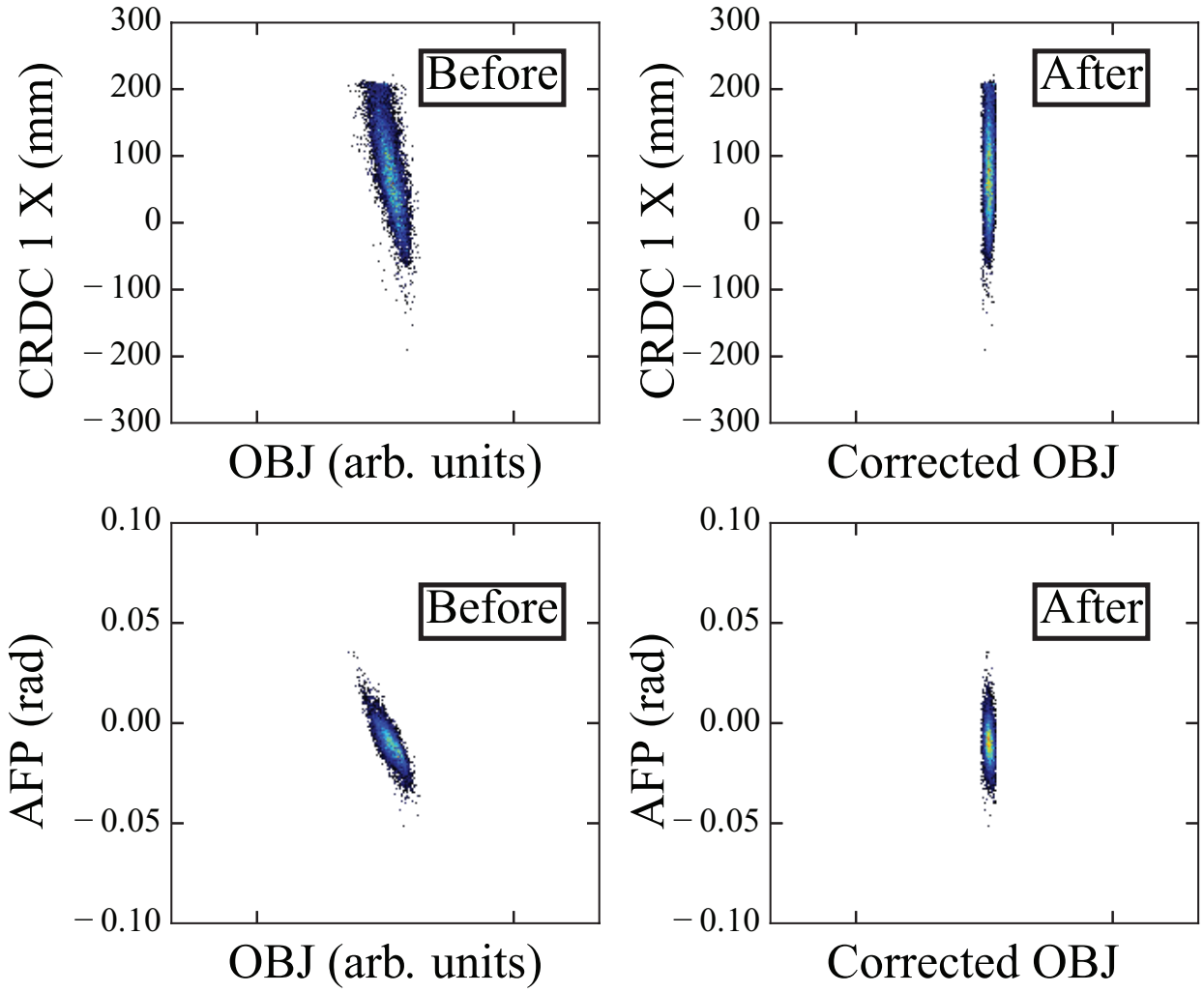

Figure 3.2: Time-of-flight correction for position in the focal plane (top row) and angle in the focal plane (bottom row), before and after corrections. This corrects for the path-length dependence of the time-of-flight as discussed in Section 2.2.1. Note this spectrum was already restricted to events containing incoming ^{71}Cu projectiles and outgoing ^{70}Ni knockout residues for illustrative purposes. A projection of the time-of-flight axis can quantify the gain, which is very visible already in the two-dimensional plot.

After correcting the time of flight, the outgoing particles were identified using the standard $\Delta E - ToF$ technique to separate particles based on Z^2, from the energy loss measured in the ionization chamber [32] in the focal plane of the S800 spectrograph, and $\frac{A}{Z}$, from

the aforementioned time-of-flight difference. The outgoing particle identification spectrum is shown in Fig. 3.3, where a red contour is drawn around the ^{70}Ni outgoing reaction products.

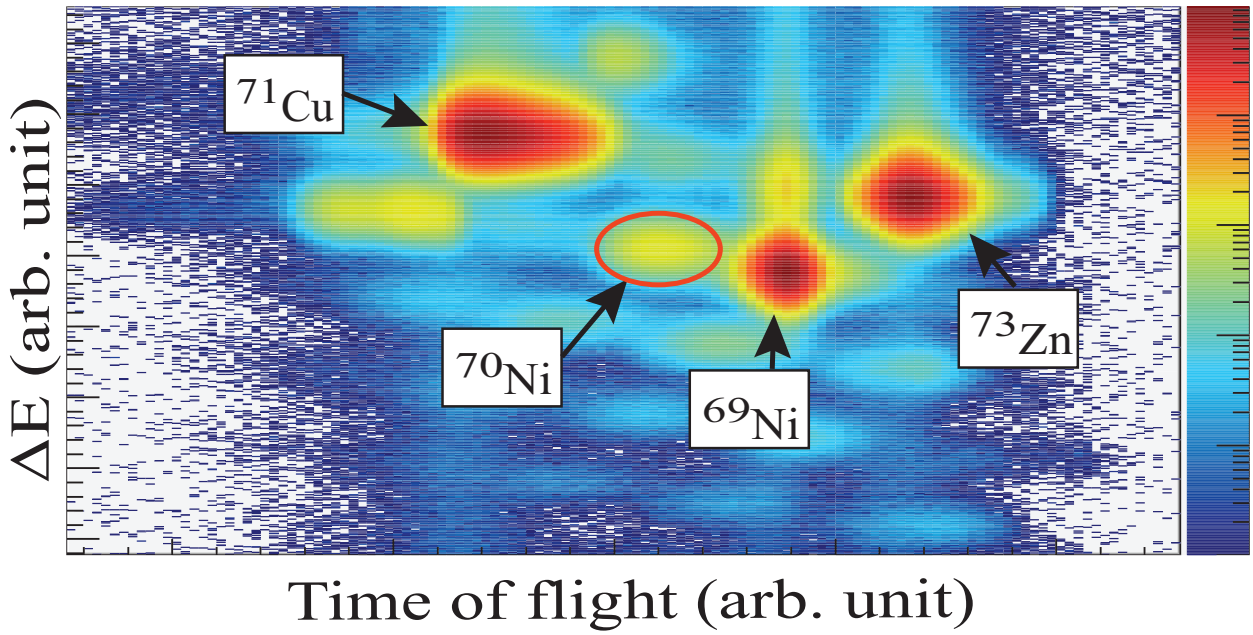

Figure 3.3: Outgoing particle identification plot presenting $\Delta E \propto Z^2$ and $ToF \propto \frac{A}{Z}$ gated on incoming ^{71}Cu projectiles. The *obj*-E1 time of flight shown here has been corrected for the angle and position of the knockout residue in the focal plane. The presence of the hot spots to the right of the ^{70}Ni reaction products is due to incoming beam contaminants.

A small amount of contamination from neighboring nuclei was present even after gating on the projectile-like ^{70}Ni knockout residues for each knockout setting. This contamination is evident as increased intensity at the edge of the distributions of angle and position in the focal plane, as in Fig. 3.4, where the position distribution in the focal plane as measured by the CRDCs as a function of time of flight are shown in (a)-(c) and the angle distribution measured between the CRDCs restricted to the contamination in (a)-(c) is shown in (d). The hot spots signaling the contamination are highlighted with red arrows in each spectrum. To remove this contamination, which is primarily localized at the edge of the focal plane, gates on the position and angle in the focal plane were necessary. Events that satisfy a

combination of cuts on the contaminants are removed from the analysis. In this way, it was possible to remove selectively the contaminants and to determine the amount of ^{70}Ni knockout residues detected. This process was repeated for both the ^{71}Ni and ^{72}Zn incoming beams.

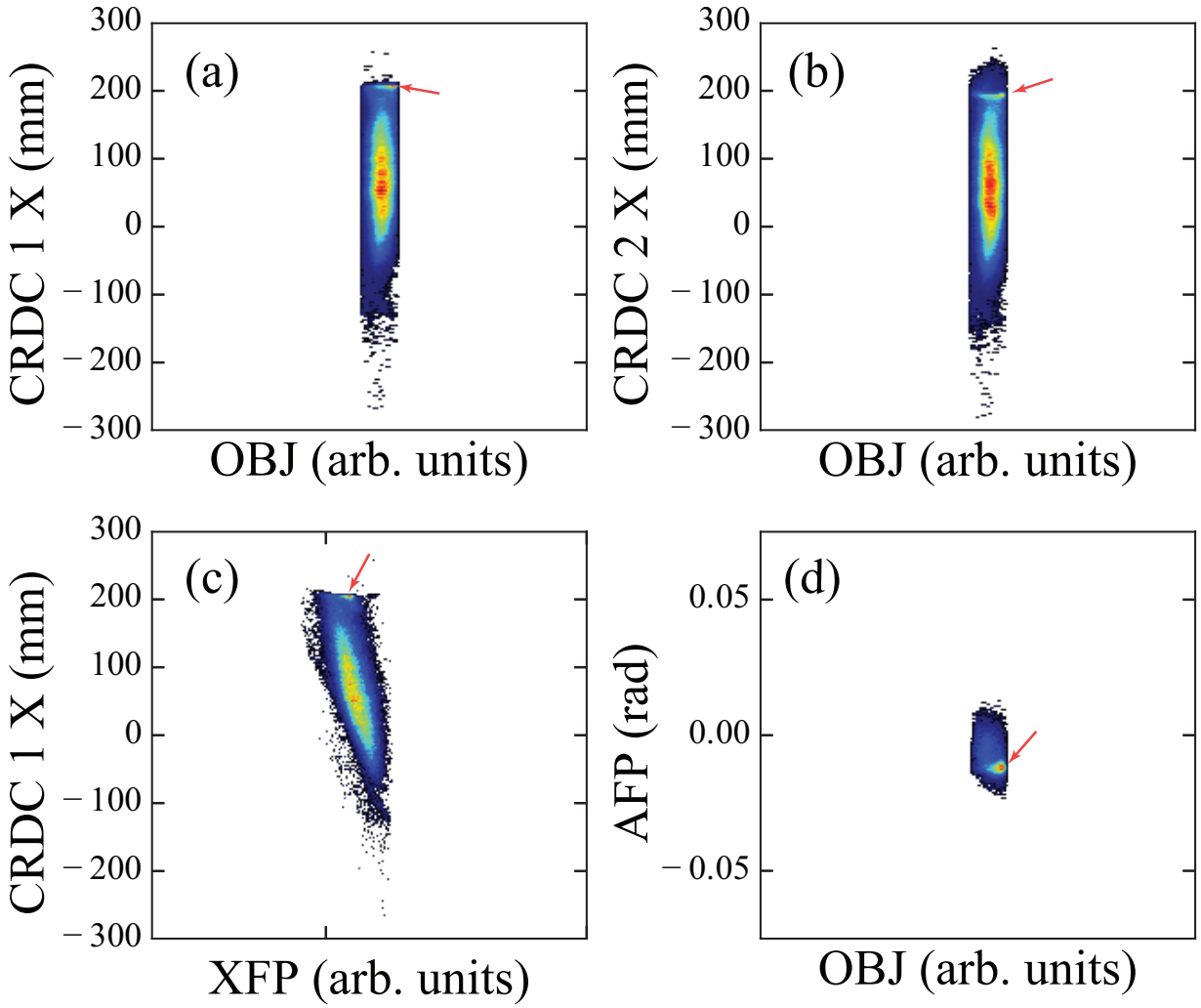

Figure 3.4: Spectra used for removing outgoing beam contaminants, which are highlighted by the red arrows. It is clear that the contaminants are localized at the edge of the focal plane based on the measured x position in the CRDCs shown in panels (a-c). Gating on these hot spots leads to the distribution of dispersive angles in the focal plane in panel (d), where there is a clear excess of counts related to the contamination.

After successfully identifying the ^{70}Ni knockout residues, it is then possible to observe the γ rays tagging de-excitation from excited states of ^{70}Ni using GRETINA.

3.2 Doppler reconstruction example for one-proton knockout setting

As discussed in Section 2.3, significant Doppler shifts are observed for the γ rays emitted in-flight at mid-target velocities of $v/c = 0.38$, $v/c = 0.37$, and $v/c = 0.35$ for the one-proton, one-neutron, and two-proton knockout reactions, respectively. To measure the intensities and identify peaks in the spectrum, it is necessary to perform a Doppler reconstruction.

The Doppler correction formula is given in Eqn. 2.3. In the following, the Doppler correction process is explored using the ^{70}Ni spectrum from one-proton knockout. The Doppler correction process starts by using the expected particle velocity v/c at the mid-target position and the γ-ray emission angle θ determined event-by-event by the angle between the main interaction point, the interaction point associated with the largest energy deposition, and a vector pointing straight downstream from the target; i.e., the optical beam axis. The following corrections rely on the aforementioned reconstructed trajectory from COSY Infinity. The corrections are described in order from largest effect on resolution to smallest.

The first correction that is applied takes into account the dispersive and non-dispersive angles of the particle at the target position. Instead of determining the emission angle relative to a vector pointing along the optical beam axis, the angle is determined relative to the reconstructed particle trajectory at the target. The emission angle θ is corrected event-by-event based on the determined *ata* and *bta*, the dispersive and non-dispersive angles at the target position (see Section 2.2.2). In practice, this means the emission angle is determined

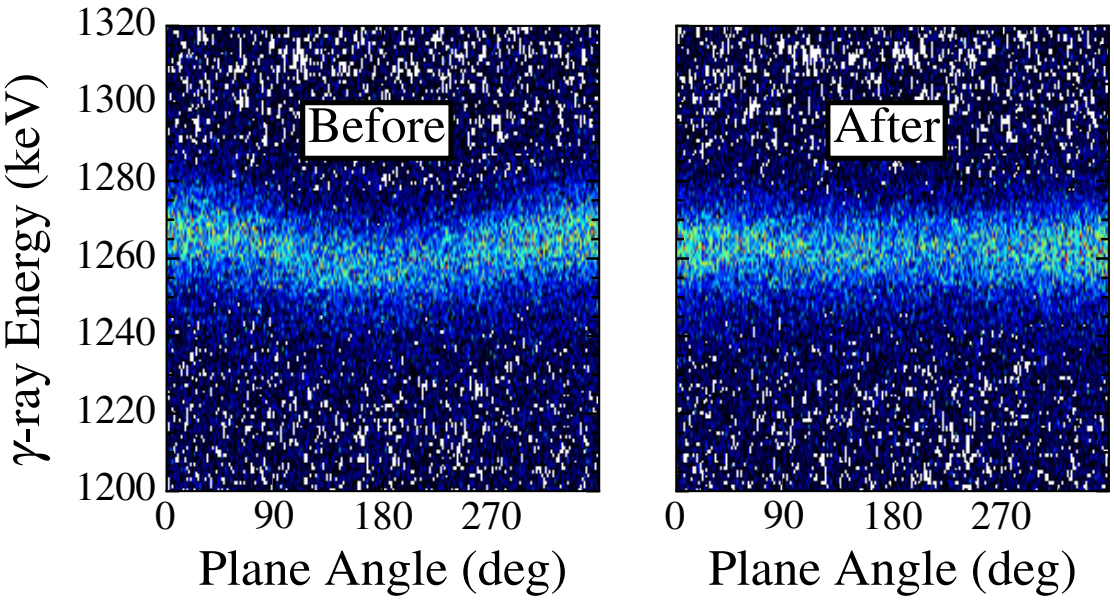

Figure 3.5: Before (left) and after (right) the ϕ correction, which is the correction for the trajectory of the particle at the target position. The x axis is the angle between the reaction plane and the detection plane, while the y axis is the detected γ-ray energy assuming the mid-target velocity.

relative to a vector:

$$\vec{u} = \left(\sin(ata), -\sin(bta), \sqrt{1 - \sin^2(ata) - \sin^2(bta)}\right), \tag{3.1}$$

rather than the initial choice of $\vec{v} = (0, 0, 1)$, where $\hat{z}$ is chosen to go along the optical beam axis. The negative sign on the second component is due to the change in coordinate systems between the S800 focal plane and GRETINA.

To visualize this correction, one can look at the Doppler-corrected energy as a function of the angle between the detection plane and the reaction plane, as shown in Fig. 3.5. The detection plane is defined by the optical axis and a vector determined by the coordinate of

the first interaction point in GRETINA (see Section 2.3.2). The reaction plane is defined by the incoming particle trajectory, assumed to be the optical axis, and the outgoing particle trajectory as determined with the S800 inverse map and Eqn. 3.1. This correction is often referred to as the ϕ correction. This plane angle ϕ_P can be determined by determining the azimuthal angle ϕ_T of the particle at the target position using the inverse map of the S800 and the azimuthal angle of the detector ϕ_D in which the γ ray was detected as follows:

$$\phi_P = 2\pi - \phi_T - \phi_D. \tag{3.2}$$

Because the reconstructed trajectory from the S800 is accurate to the order a few mrad, the dominant remaining uncertainty in determining the emission angle stems from the $\sigma \approx 10$ mrad uncertainty from the position resolution of GRETINA.

So far, the point of γ ray emission is considered to be a fixed point for all events. In reality, the beam spot size of the incoming beam on the target exhibits a sizable spread, especially in the non-dispersive direction. The width of the *yta* distribution for the ^{71}Cu setting was $\sigma \approx 3$ mm, which is considerable when compared to the $\sigma = 2$ mm spatial resolution of GRETINA. This non-dispersive position is measured event-by-event using the inverse map of the spectrograph as *yta*, which can be used to further refine the emission angle determination for the Doppler shift correction.

Figure 3.6, in which each pane corresponds to an individual crystal, clearly shows the correlation between the non-dispersive position on the target and the Doppler reconstructed energy after the ϕ correction for the forward detectors. The panes are ordered ring-by-ring in the GRETINA coordinate system from smallest polar angle to largest, and within rings from smallest azimuthal angle to largest, where $\phi = 90^\circ$ and $\phi = 270^\circ$ correspond to the

non-dispersive direction. Note that this effect is most prominent on the forward detectors; i.e., the first fifteen panels. This is because the detectors at 90° are not sensitive to the non-dispersive position on the target, as shifts in the non-dispersive position will not have a significant impact on the polar angle determining the Doppler shift for the 90° detectors. The spectra after correcting for this correlation are shown in Fig. 3.7.

After this correction, the *dta* value is used to correct the velocity of the particle. As noted previously, this is a measurement of the kinetic energy after the target, and therefore cannot correct for the uncertainty in the velocity due to the energy loss through the target. The *dta* value is $\frac{dT}{T}$, where $T = E - mc^2$ is the kinetic energy. The velocity is corrected event-by-event by an amount (see the derivation in Appendix B):

$$d\beta = \frac{dT}{T}\frac{\beta}{\gamma(\gamma+1)}, \tag{3.3}$$

where $\beta = \frac{v}{c}$ and γ is the Lorentz factor. Figure 3.8 and Figure 3.9 show before and after the correction in Eqn. 3.3 is applied.

Finally, after the event-by-event corrections based on the inverse map are completed, the resolution of the transitions in the spectrum can be further improved by a set of global parameters to correct for the incoming beam not being perfectly aligned with the optical beam axis; i.e., correcting for offsets in the xy position of the beam spot and the beam angle offsets a_0 and b_0. These offsets are systematically varied until the correlation between Doppler-corrected energy and crystal position is minimized. The magnitude of the offsets were determined to be $x_0 = 2.5$ mm, $y_0 = 0.1$ mm, $a_0 = 6.8$ mrad, and $b_0 = 2.3$ mrad. The spectra following the different steps of the Doppler correction process is shown in Fig. 3.10.

The final $\frac{v}{c}$ used for reconstruction was chosen to optimize the resolution of the high-

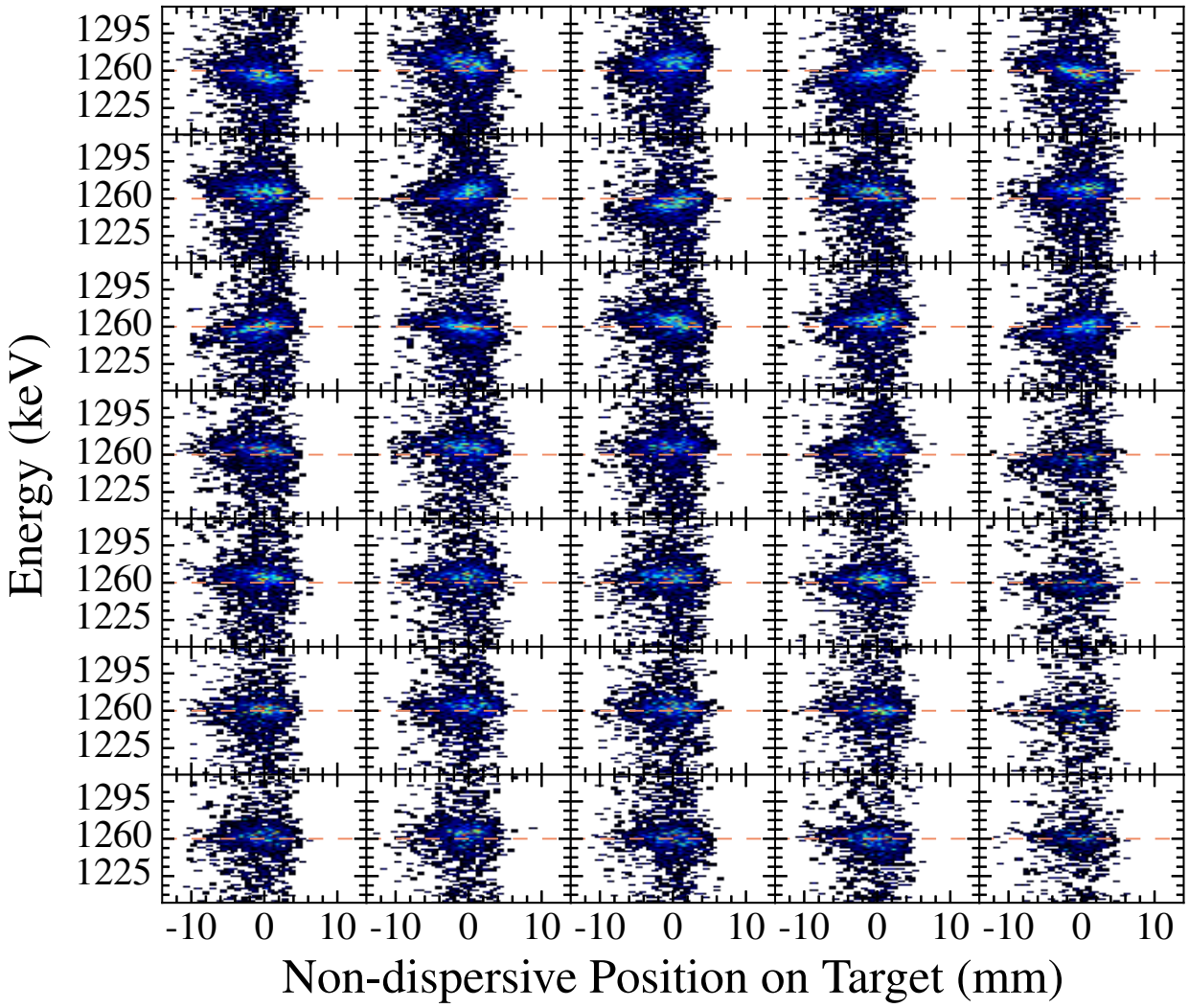

Figure 3.6: Before correction to remove correlation between γ-ray energy following the ϕ and *yta* corrections. Each panel corresponds to a different crystal. Crystals are ordered ring-by-ring, from smallest to largest polar angle, and then within rings from smallest to largest azimuthal angle.

intensity 1260-keV $2_1^+ \rightarrow 0_1^+$ transition in ^{70}Ni. Combining all of these corrections made it possible to achieve energy resolutions of 0.9%, 1.1%, and 1.2% FWHM for the high-intensity 1260-keV peak in the one-proton, one-neutron, and two-proton knockout reactions, respectively. The worse resolution for one-neutron and two-proton knockout was due to the

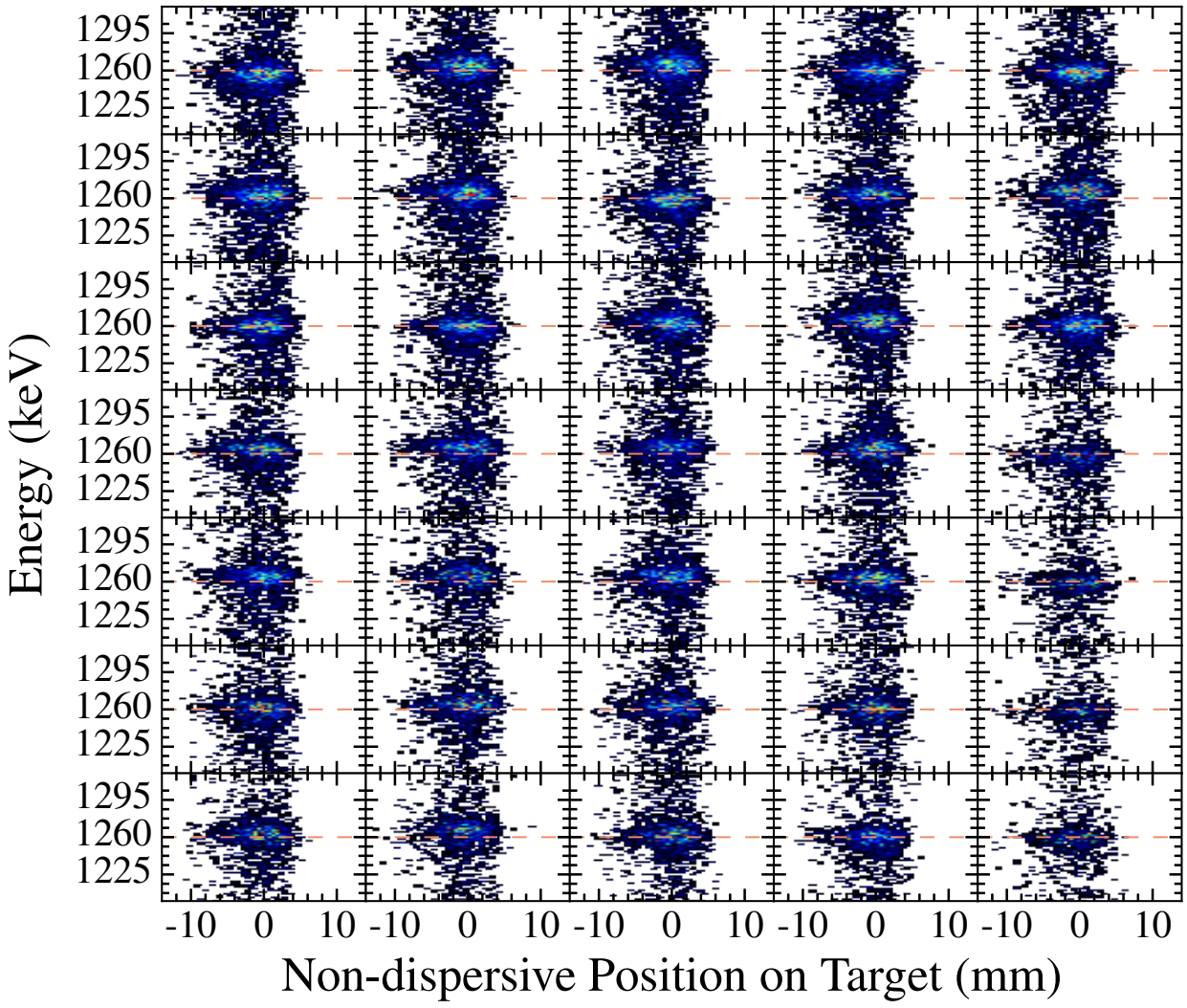

Figure 3.7: After correction to remove correlation between γ-ray energy following the ϕ and *yta* corrections. Each panel corresponds to a different crystal. Crystals are ordered ring-by-ring, from smallest to largest polar angle, and then within rings from smallest to largest azimuthal angle.

use of a thicker 188 mg/cm^2 ^{9}Be target. The use of the thicker target leads to increased luminosity, but also increases the energy loss through the target, which is the largest source of uncertainty in the determination of the velocity of the particle at the γ-ray emission point. Now that the particles are identified and the Doppler reconstruction is complete, it

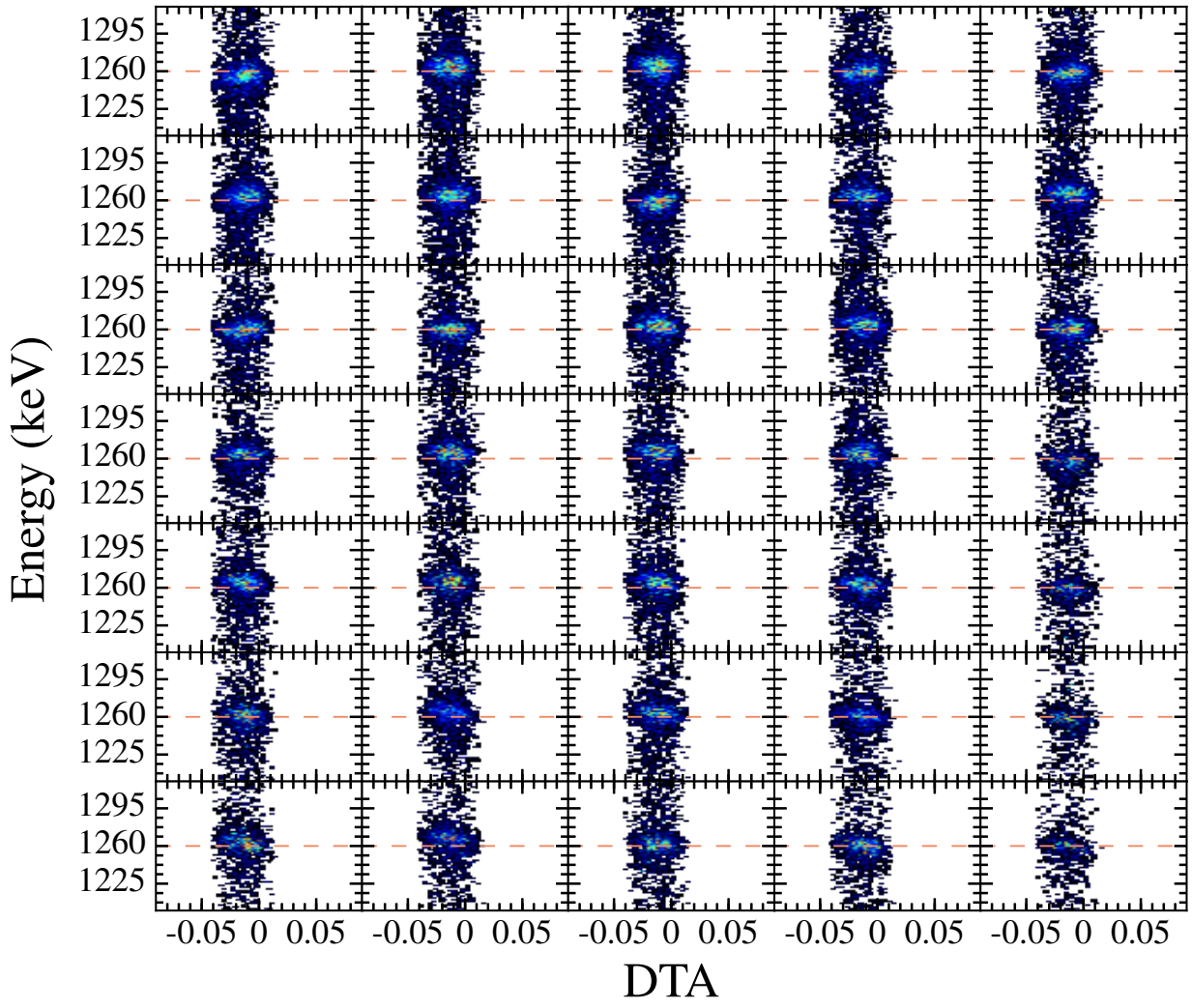

Figure 3.8: Before correction to remove correlation between γ-ray energy following the ϕ and *yta* corrections and the particle's kinetic energy after the target. Each panel corresponds to a different crystal. Crystals are ordered ring-by-ring, from smallest to largest polar angle, and then within rings from smallest to largest azimuthal angle.

is reasonable to start identifying more transitions and measuring their intensities.

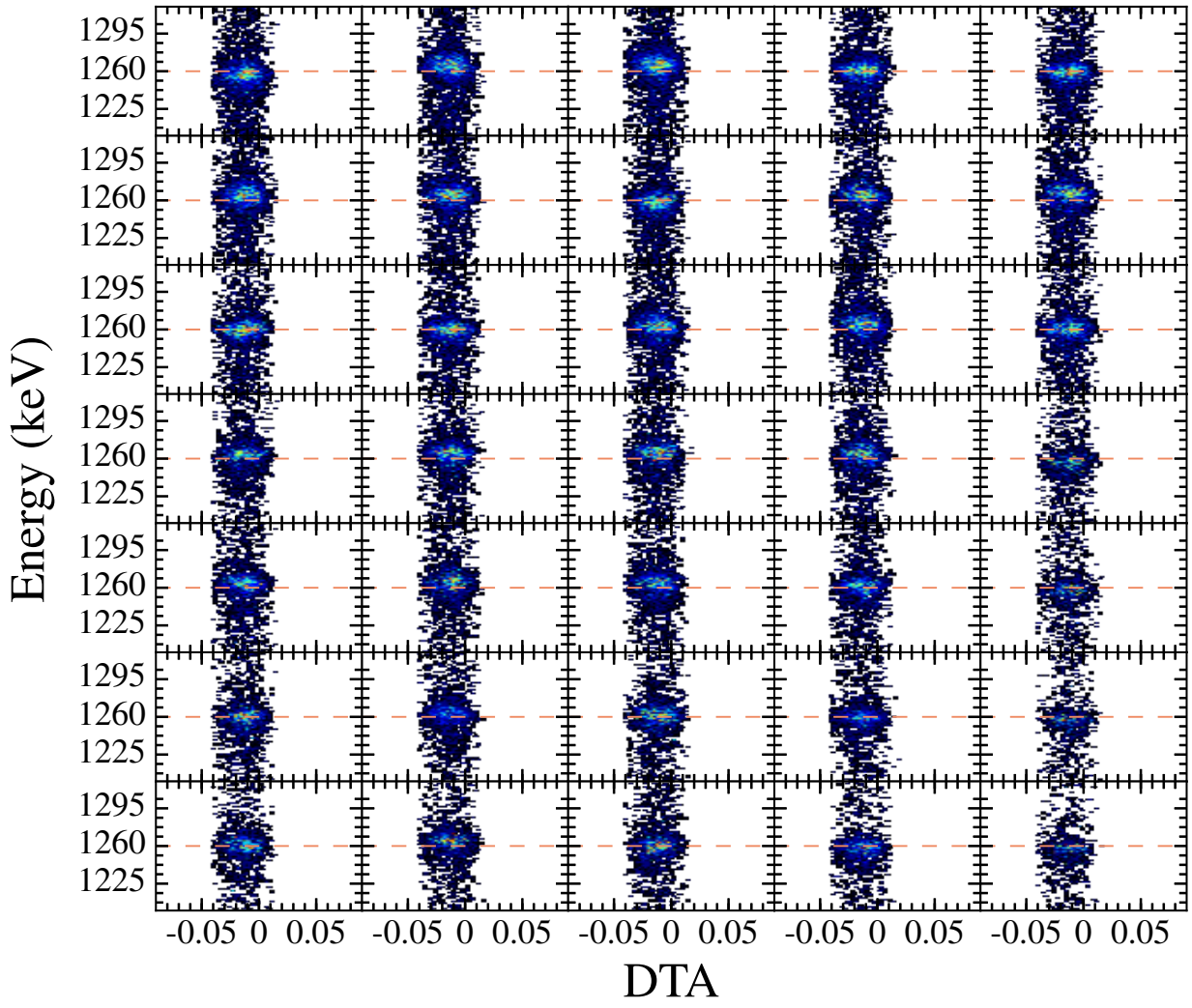

Figure 3.9: After correction to remove correlation between γ-ray energy following the ϕ and *yta* corrections and the kinetic energy after the target. Each panel corresponds to a different crystal. Crystals are ordered ring-by-ring, from smallest to largest polar angle, and then within rings from smallest to largest azimuthal angle.

3.3 Determining transition intensities

To measure the transition intensities for ^{70}Ni, it was necessary to fit the spectrum with a fit template including the peak response for all observed transitions as well as a background template, composed of both an exponential to model the beam-correlated background [34] as

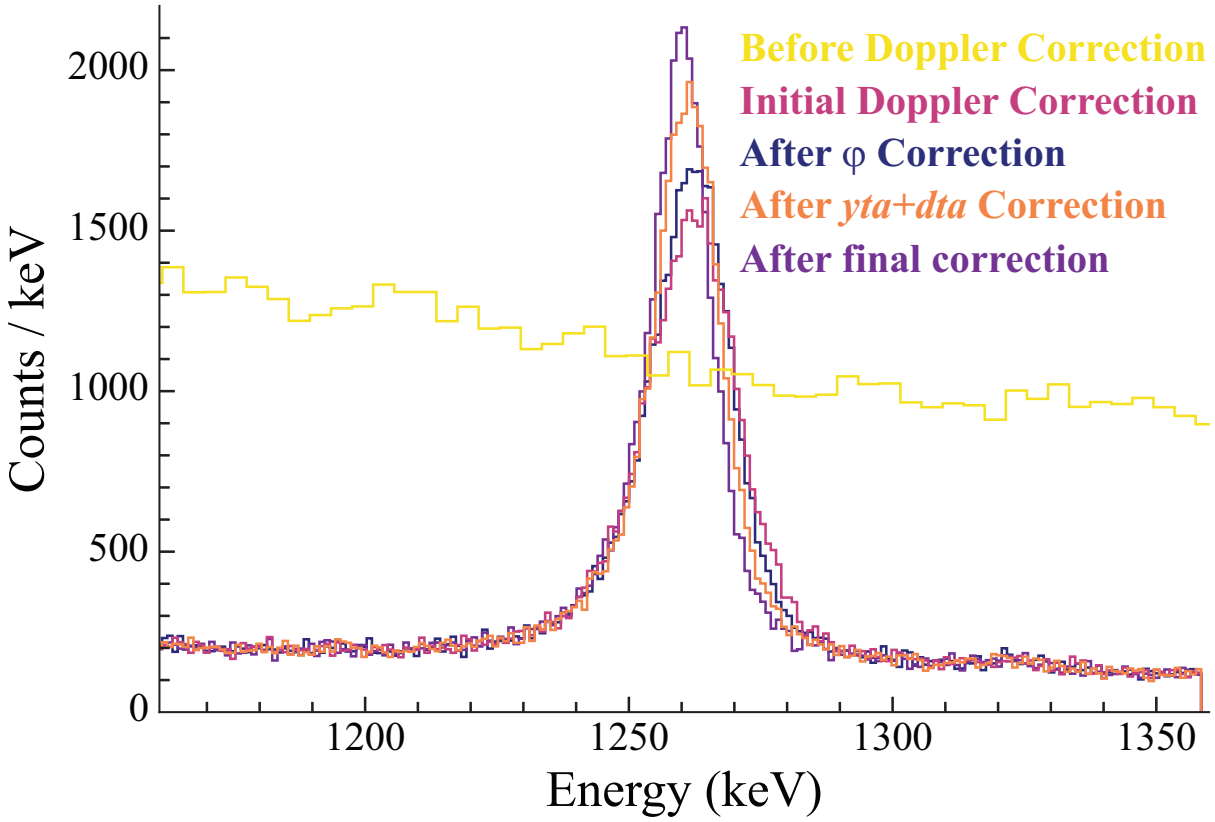

Figure 3.10: Spectra showing the gradual improvement of the resolution of the Doppler-corrected 1260-keV γ ray in ^{70}Ni following each of the different corrections described in the text.

well as simulated stopped background lines, which are present due to the inelastic reactions between neutrons and other light particles with both the germanium detectors and the aluminum beam pipe. These stopped lines had a considerably smaller effect compared with the exponential background and the peak response of observed transitions in ^{70}Ni. The scaling factor for each stopped line was fixed by fitting each individual transition in the non-Doppler reconstructed spectrum, and the resulting sum of the spectra from each stopped line was included as a fixed part of the background model.

Shown in Fig. 3.11 is the region between 1500 and 2000 keV, where there were a number of γ rays observed in the one-proton knockout setting. This fit template included all the

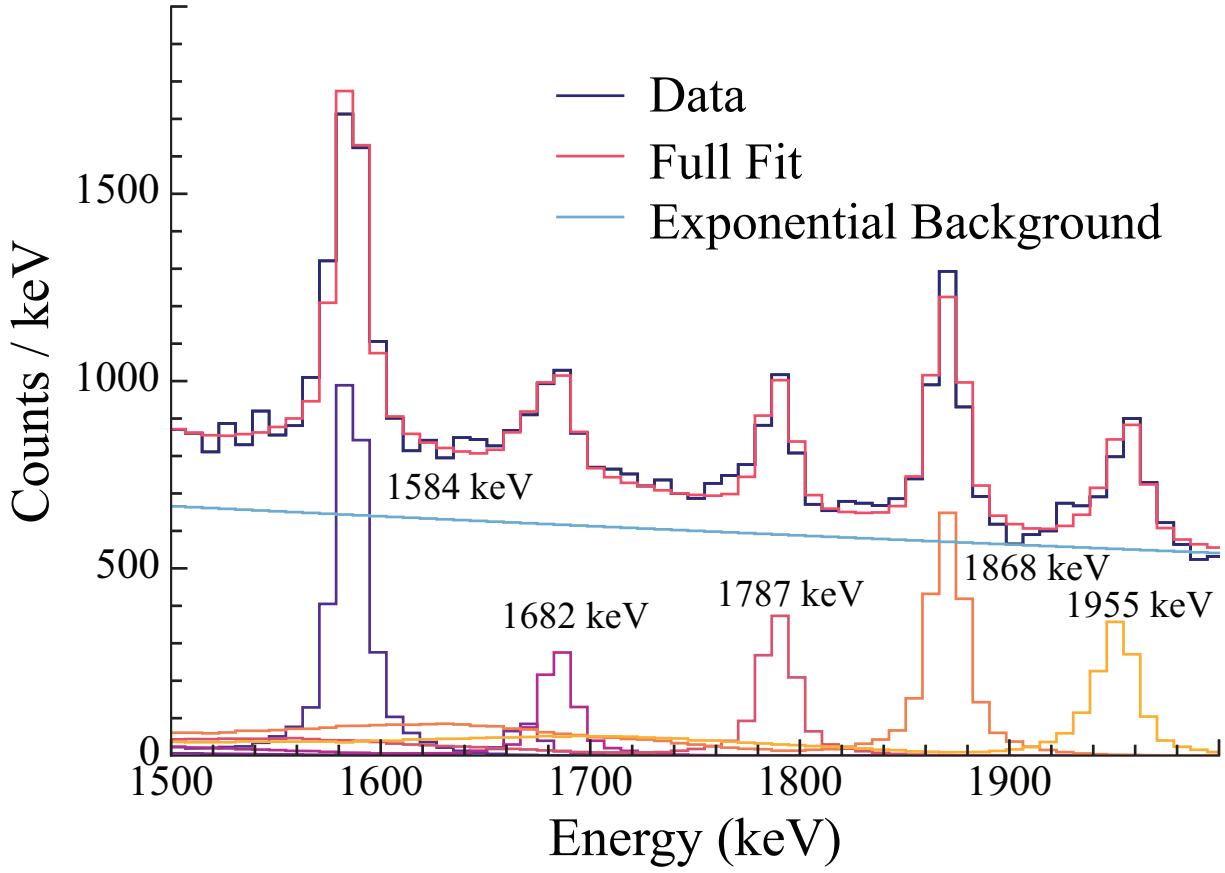

Figure 3.11: Spectrum observed in coincidence with ^{70}Ni knockout residues showing different components of the fit template in the region 1500-2000 kev.

peaks shown and an exponential background. The scaling factor for each peak included in the template as well as the scaling and decay parameters for the exponential were allowed to vary. It was important to utilize multiple different fitting ranges when determining the peak areas, because the Compton background of peaks at higher energies with significant intensity contribute background to peaks at lower energies. By varying this fitting range and including other transitions, one can determine a systematic fitting uncertainty for each determined peak area by observing the change in peak areas.

After fitting the spectrum, the full-energy-peak response from simulation was scaled by the scaling factor determined by the fit and integrated in a region of width 4 FWHM centered

on the peak, as described in Section 2.3.4. After determining this peak area, it was divided by the efficiency, which is discussed in Section 2.3.6, to deduce the measured transition intensity. The final-state populations can then be determined by summing up the γ-ray transition intensities for all decay branches from a given state and then subtracting any intensity feeding into that state from de-excitations of higher-lying levels.

To compare the results of the different knockout reactions, it is important to ensure that the deduced populations are not affected by the existence of long-lived states in the incoming beams. This is important because these isomeric states will likely exhibit different single-particle configurations than the ground-state and this can lead to drastically different final-state populations following nucleon knockout. Hence, the isomeric content of the incoming beams needed to be measured.

3.4 Isomeric content of incoming beams

Because both ^{71}Cu and ^{71}Ni are known to exhibit isomers in their level schemes, it was necessary to determine the amount of isomeric content for states with lifetimes exceeding a few hundred nanoseconds in the incoming beams, which would reach the reaction target of the S800 before decaying. This is necessary because knockout from the incoming projectile's excited states, which will have configurations different from the ground state, will lead to different final-state populations in ^{70}Ni, and may even access states that are not directly accessible via nucleon knockout from the ground state. To determine the isomeric content, a 5.1 mm thick Al stopper was placed at the center of GRETINA, which was used to measure the γ rays emitted from the long-lived states. GRETINA is *free running* during these measurements, such that every γ ray in GRETINA is recorded and the coincidence between

implantation and the detected γ ray is accomplished by comparing event time stamps.

For these measurements, the particle trigger is switched from the E1 scintillator in the S800 focal plane to the *obj* scintillator, so that each *incoming* particle triggers the data acquisition system. The *xfp-obj* time-of-flight difference can be used to identify the incoming particle of interest, and the number of incoming particles corrected for the beam purity within this time-of-flight difference gate determines the number of implanted particles.

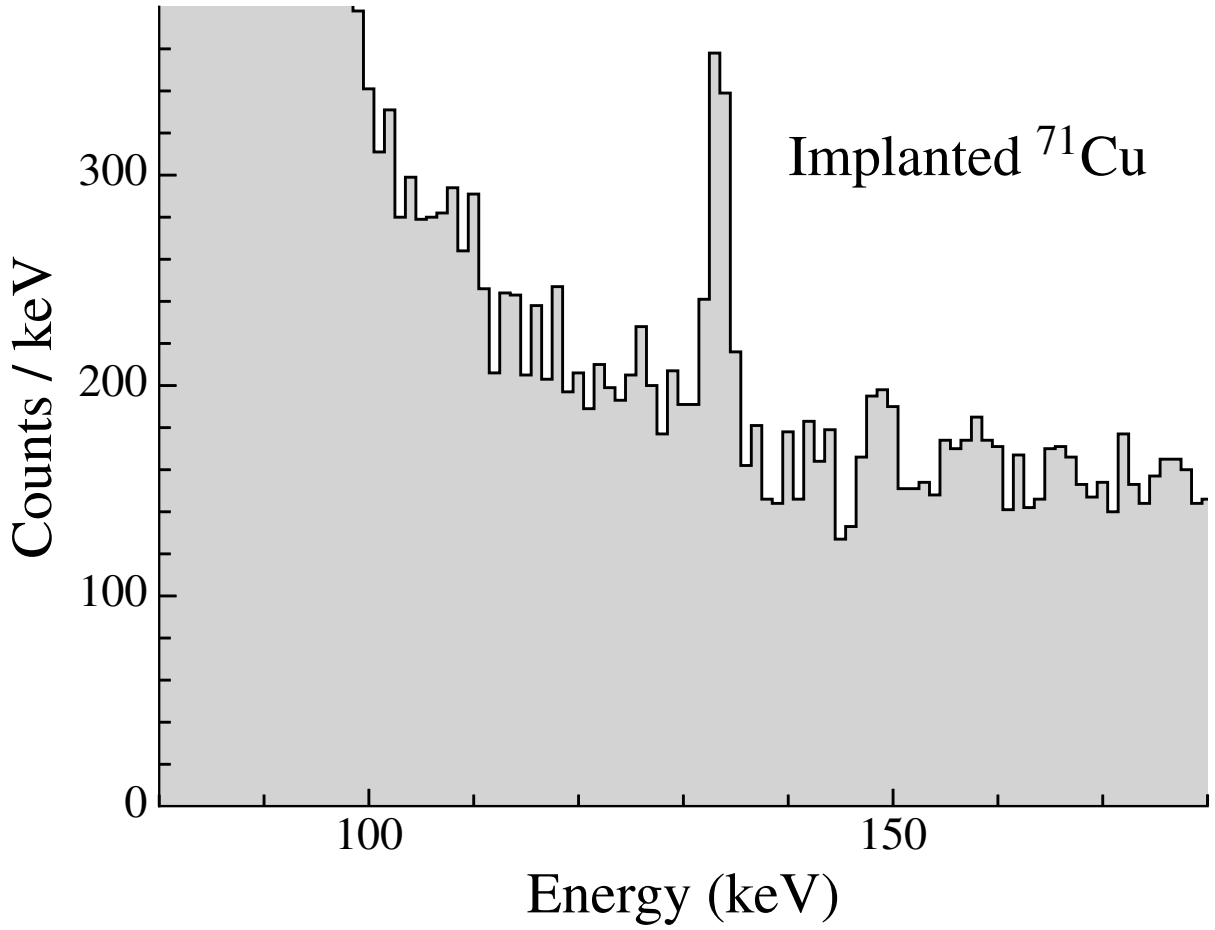

Figure 3.12: Spectrum in coincidence with ^{71}Cu projectiles implanted into an aluminum stopper at the center of GRETINA. The area of the peak at 133 keV, which corresponds to the de-excitation from the long-lived $(19/2^-)$ state in ^{71}Cu, was measured relative to the number of implants to estimate the isomeric content in the beam.

In the case of ^{71}Cu, there is a known $(19/2^-)$ state at 2756 keV with mean lifetime

$\tau = 391(20)$ ns [11]. First, the number of particles was determined by the number of triggers from the *obj* scintillator, corrected for the 95% beam purity for this setting. No time-of-flight difference restriction was possible, because the ^{69}Ni and ^{73}Zn components of the incoming cocktail beam largely overlapped in time of flight with the ^{71}Cu.

The incoming beam rate was on the order of 1.1 kHz, meaning that the resulting low γ-ray decay activity would compete with natural background radiation. To reduce the natural background in order to measure the number of decays from the $(19/2^-)$ isomer, only γ-ray events within 1 μs of implantation were considered. The intensity of the 133-keV γ ray tagging the de-excitation from this state in Fig. 3.12 is determined by fitting the peak with a simple Gaussian peak shape and a linear background to determine the peak area and then correcting this for the detection efficiency of GRETINA.

Because the 133-keV γ ray was low in energy, the absorption inside the 5.1 mm aluminum stopper needs to be taken into consideration. To account for this, a simulation was performed with UCGretina (see Section 2.3.4) including the aluminum plate at the center of GRETINA. The γ ray was assumed to be emitted at the center of the aluminum plate, which is the position that would maximize absorption, to estimate the number of transitions that would be absorbed and correct the measured transition intensity. The transition intensity corrected for loss in the aluminum stopper is then divided by the number of implanted particles to determine the isomeric content, which for incoming ^{71}Cu was $I_c = 0.47(7)\%$.

The isomeric content for the ^{71}Ni cocktail beam is more difficult to measure, because the long-lived $(1/2^-)$, 499-keV state, which has a mean lifetime of $\tau = 3.3(4)$ s [11], does not γ decay. Instead, it β decays into either the $3/2^{(-)}$ ground state or the $(1/2^-)$ excited state at 454 keV of ^{71}Cu [41]. The intensity of the 454-keV γ ray tagging the de-excitation from this state in Fig. 3.13 is determined by fitting the peak with a simple Gaussian peak shape and

a linear background to determine the peak area and then correcting this for the detection efficiency of GRETINA.

The *xfp-obj* time difference was particularly important for this setting in determining the number of ^{71}Ni ions implanted, because there is a large amount of ^{72}Cu in the incoming cocktail beam. After applying a gate to the *xfp-obj* time-of-flight difference, the beam purity satisfying the gate was determined to be 88%, compared to 63% without any time-of-flight restriction. The number of particle triggers determined with the *obj* scintillator within this gate was corrected for this beam purity.

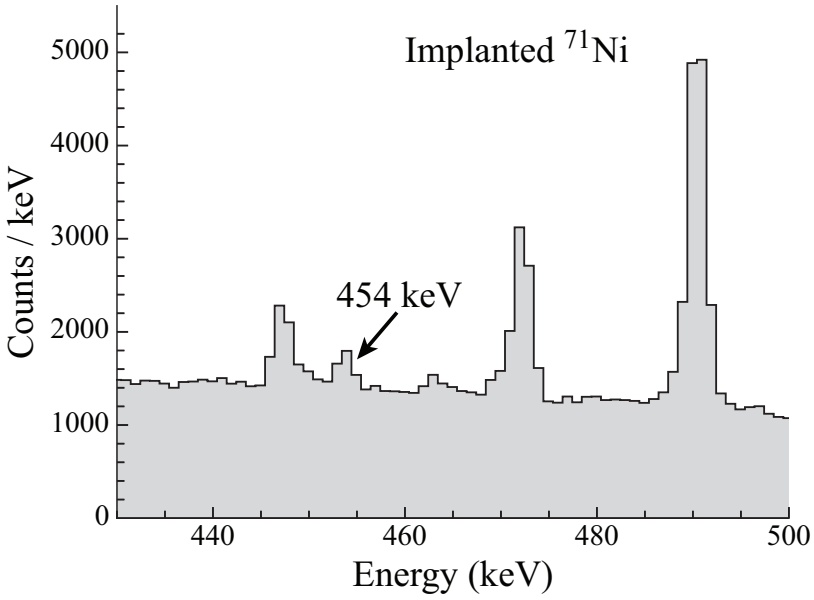

Figure 3.13: Spectrum in coincidence with ^{71}Ni projectiles implanted into an aluminum stopper at the center of GRETINA. The area of the peak at 454 keV, which corresponds to the de-excitation from the long-lived $(1/2^-)$ state in ^{71}Cu to which the isomeric $(1/2^-)$, 499-keV level in ^{71}Ni β-decays, was measured relative to the number of implants to estimate the isomeric content in the beam.

Unlike the case of ^{71}Cu, the long $\tau = 3.3(4)$ s lifetime of the isomeric state in ^{71}Ni meant that using a timing restriction to minimize natural background was impossible, so the 454-keV peak had to be discriminated on top of the natural background. Analysis was limited

to events occurring after the first 6.9 s, three mean lifetimes of the decaying state, which reduces the amount of background in the spectrum from other shorter-lived decays.

Because the adopted NNDC β-decay branching ratio to the excited $(1/2^-)$ state is an upper limit of 40%, the lower limit of the isomeric content of the incoming ^{71}Ni beam based on the observed intensity of the 454-keV, $(1/2^-) \rightarrow 3/2^{(-)}$ transition is $I_c > 6\%$. This value takes into account the absorption of the γ ray in the thick aluminum stopper in the same manner as described above for ^{71}Cu.

Chapter 4

Results: γ-ray spectroscopy of ^{70}Ni following nucleon knockout

In the following chapter, the results for each knockout reaction will be presented, including $\gamma\gamma$ coincidence spectra used for placing transitions into the level scheme and measured intensities for both placed and unplaced transitions. The results for the measured transition intensities relative to the number of detected ^{70}Ni knockout residues for each reaction are shown in Table 4.1 for placed transitions and Table 4.2 for transitions that remain unplaced, respectively. All intensities are determined from γ-ray singles spectra unless otherwise noted. The number of ^{70}Ni was determined for each setting based on the number of triggers satisfying the particle identification gates corrected for the dead time of the data acquisition system.

All fits to γ-ray spectra used to extract transition intensities included the simulated peak responses determined with GEANT4 [39] (see Sec. 2.3.4), along with an exponential used to model the beam correlated background and simulated stopped background lines, which are present due to the inelastic reactions between neutrons and other light particles with both the germanium detectors and the aluminum beam pipe. The quoted uncertainties are described in more detail in the caption for Table 4.1. A systematic energy uncertainty of 2.2 keV was determined by comparing known transition energies from the NNDC database [11]

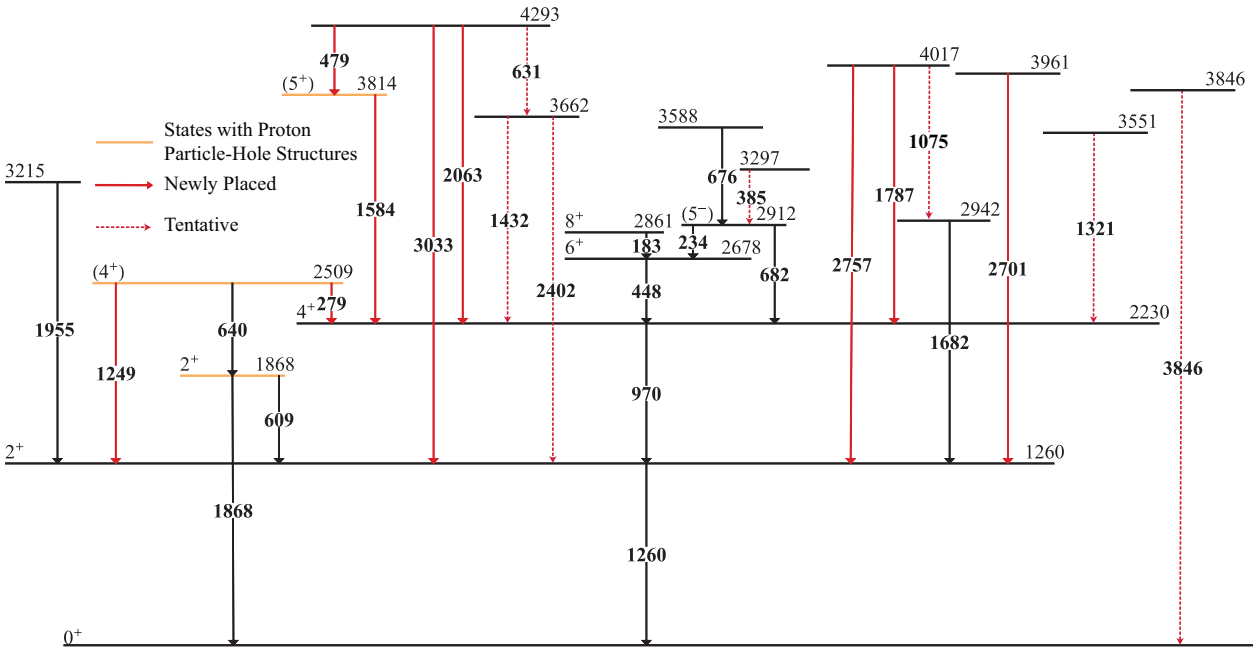

Figure 4.1: The level scheme for ^{70}Ni based on the transitions observed in each reaction channel for this experiment. Transitions that are placed for the first time into the level scheme are shown in red, while dashed lines indicate tentative placements. The levels highlighted in orange are expected to exhibit proton-particle hole configurations.

to the peak energies observed in the experiment. The level scheme for ^{70}Ni based on the observed transitions in each reaction channel is given in Fig. 4.1.

To determine the coincidence relationships between different transitions in the spectra, nearest-neighbor add-back was utilized. This is described in more detail in Section 2.3.3. All $\gamma\gamma$ coincidence spectra presented in this chapter exploited nearest-neighbor addback to improve the peak-to-total ratio and therefore make it possible to place more transitions.

4.1 One-proton knockout from ^{71}Cu

In the one-proton knockout reaction, states in the yrast band and the suspected prolate sequence are populated, along with several higher-lying states of undetermined spin-parity. A total of 26 previously unplaced transitions were observed in this reaction channel, and

Table 4.1: Measured intensities for all observed, placed ^{70}Ni transitions relative to the number of detected ^{70}Ni residues in the specific reaction channel expressed as a percentage. The error includes both statistical uncertainties and systematic contributions from varying the fit assumption for peak shapes and backgrounds, and a 2.1% uncertainty from the efficiency determination. Note that no feeding subtraction is attempted here.

State Energy (keV)	Transition Energy (keV)	Rel. Intensities (%) 1p Knockout	Rel. Intensities (%) 1n Knockout	Rel. Intensities (%) 2p Knockout
1260(2)	1260(2)	44(2)	14.5(8)	21(1)
1868(2)	609(2)	3.6(4)	1.9(3)	2.4(4)
	1868(2)	3.5(6)	1.3(5)	2.5(5)
2230(3)	970(2)	16.5(9)	5.7(7)	7.8(8)
2508(4)	279(3) [a]	0.5(2)	0.3(2)	0.5(2)
	640(2)	2.2(3)	1.2(6)	2.2(4)
	1249(3) [b]	2.4(4)	1.7(3)	1.0(6)
2912(4)	234(4) [c]	0.4(1)	1.5(4)	0.6(2)
	682(3) [d]	1.1(3)	3.9(6)	1.6(5)
2942(4)	1682(3)	1.3(3)	-	1.0(9)
3215(4)	1955(3)	2.1(2)	0.8(3)	0.7(5)
3297(5)	385(3)	1.3(2)	2.6(7)	1.3(5)
3551(5)	1321(4)	0.7(1)	-	-
3588(6)	676(4)	0.12(3)	-	0.16(5)
3662(4)	2402(3)	0.8(2)	-	-
	1432(4)	0.3(2)	-	-
3814(3)	1584(2)	4.4(4)	-	-
3846(5)	3846(5)	0.7(1)	-	-
3961(4)	2701(3)	1.6(3)	-	-
4017(4)	1075(3) [e]	0.9(5)	0.4(3)	1.2(6)
	1787(3)	1.8(6)	-	-
	2757(3)	1.4(2)	-	-
4293(4)	479(3)	0.7(2)	-	-
	631(4)	0.9(2)	-	-
	2063(3)	0.75(16)	-	-
	3033(5)	1.2(2)	-	-

[a] The expected intensity for the 279-keV transition is below the detection sensitivity in the one-neutron and two-proton reaction channels, so the intensity for these channels was estimated based on the branching ratio measured in one-proton knockout

[b] The discrepancy between the different measurements of the 1249-keV transition intensity relative to the 640-keV one is due both to the difficulty of determining the intensity in a self-coincident doublet and to possible lifetime effects as discussed in Section 4.2.

[c] The intensities given for the 234-keV γ ray for the one-proton and two-proton knockout are determined based on the NNDC adopted branching ratio [11].

[d] The splitting between the self-coincident 676-682 keV doublet is determined based on add-back coincidences for the one-proton knockout. This splitting was then used for the two-proton knockout as well.

[e] The non-observation of the 1787- and 2757-keV transitions in the one-neutron and two-proton reactions is understood based on the small, highly uncertain intensity observed for the 1075-keV γ ray.

Table 4.2: Measured intensities for all observed, unplaced ^{70}Ni transitions relative to the number of detected ^{70}Ni residues in the specific reaction channel expressed as a percentage. See the caption to Table 4.1 for more information.

Transition Energy (keV)	Rel. Intensities (%) 1p Knockout	Rel. Intensities (%) 1n Knockout	Rel. Intensities (%) 2p Knockout
424(5)	-	0.6(3)	0.7(3)
660(3)	0.6(4)	1.2(11)	1.2(4)
714(4)	-	-	1.4(9)
915(5)	0.9(3)	1.5(4)	-
930(5)	0.33(25)	0.9(3)	-
958(5)	0.6(3)	1.8(5)	-
1212(5)	-	-	1.1(5)
1225(5)	-	1.7(4)	-
1440(3)	0.8(3)	-	-
1467(3)	0.5(2)	-	-
2026(3)	1.2(2)	-	2.2(5)
2114(3)	0.8(2)	0.6(3)	-
2342(5)	0.5(2)	-	-
2980(4)	0.4(3)	-	-

16 of these transitions were placed into the level scheme for ^{70}Ni in Fig. 4.1. There was a combination of insufficient statistics, resolution, or coincidence relationships to place the remaining transitions. The fit used to extract the intensities of the transitions is presented in Fig. 4.2. This fit was composed of simulated peak responses for all peaks in the spectrum as well as a background composed of double-exponential component to model the beam-correlated background and simulated stopped background lines, which are present due to the inelastic reactions between neutrons and other light particles with both the germanium detectors and the aluminum beam pipe.

The levels populated in the proton-knockout channel are presumably positive parity ones based on the available orbitals from which protons can be removed from ^{71}Cu. Population of negative-parity states at low excitation energies in the proton knockout reaction would require indirect feeding from higher-lying positive parity ones. This is because negative-parity

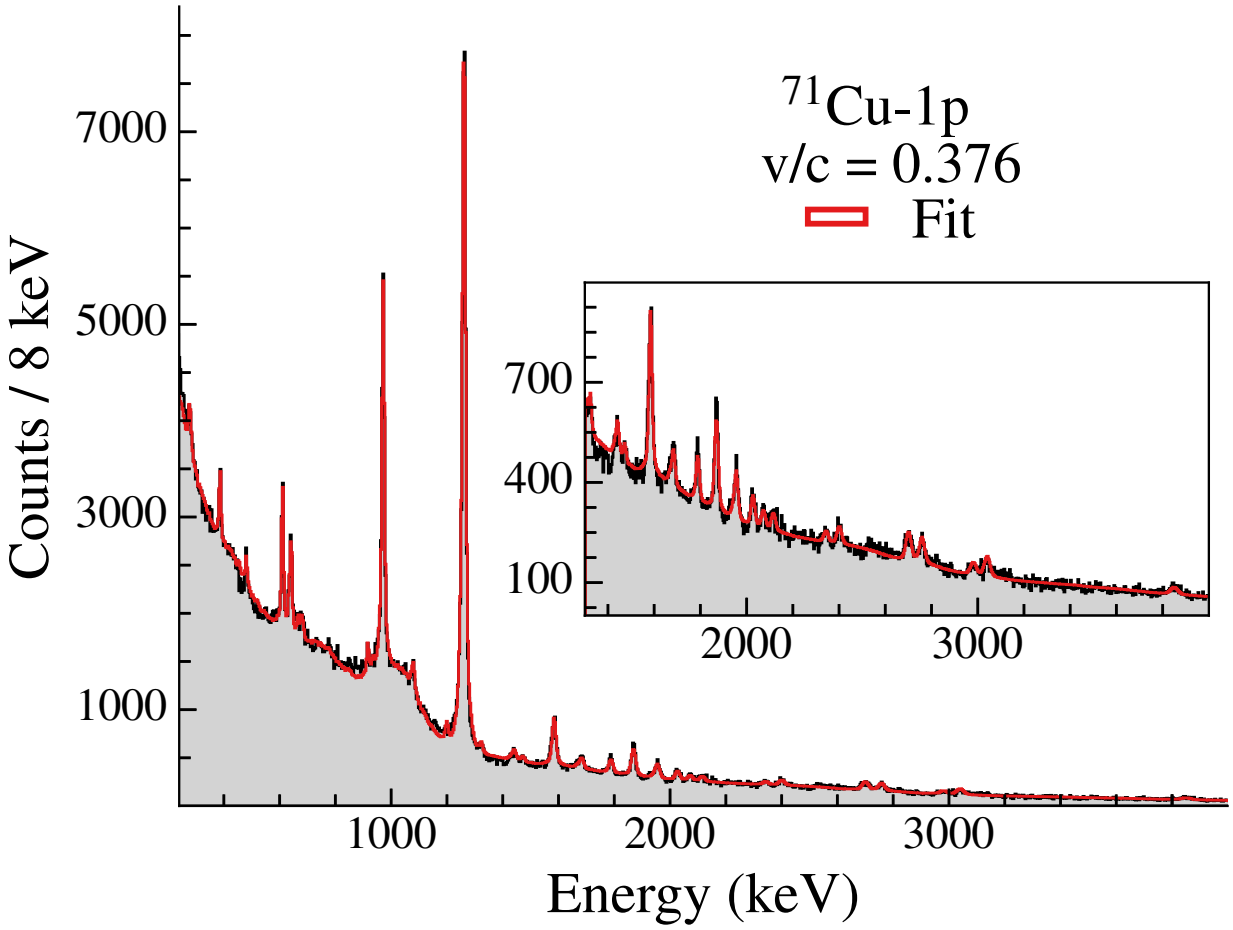

Figure 4.2: An example of a fit used to extract intensities from the ^{70}Ni spectrum populated via one-proton knockout from ^{71}Cu. The fit consisted of simulated line shapes for all peaks observed in the spectrum as well as a background composed of a double exponential to model the beam-correlated background in addition to stopped background lines from both inelastic reactions of neutrons and other light particles with the aluminum beam pipe or Ge detectors as well as annihilation radiation. Clearly present in the spectrum are the 970-keV, $4_1^+ \rightarrow 2_1^+$ and 1260-keV, $2_1^+ \rightarrow 0_1^+$ transitions in the yrast sequence along with many other transitions discussed in the text.

levels would imply knockout from the *sd* shell for the proton knockout reaction channels. The states populated via the knockout of *sd*-shell protons would be expected to appear at energies above 6 MeV in the spectrum [42].

Within the suspected prolate structure, the majority of previously known transitions were observed, with the notable exception of any transitions into or out of the (0_2^+) isomeric

state. Unfortunately, the measured lifetime [17] of the suspected 0_2^+ level excluded any possibility of measuring the $(0_2^+) \rightarrow 2_1^+$, 307-keV transition, as it would decay after entering the S800 entrance quadrupole but well before implanting within the aluminum plate in front of the hodoscope. In addition to the previously known transitions, two new transitions were observed and placed in the possible prolate sequence: a $(4_2^+) \rightarrow 2_1^+$, 1249-keV transition and a $(4_2^+) \rightarrow 4_1^+$, 279-keV transition. The coincidences between the yrast transitions and these two new transitions in the prolate structure are present in the coincidence spectra in Fig. 4.3(a) and (b), respectively. Also present in Fig. 4.3(a) are other previously reported transitions within the prolate structure: the 640-keV, $(4_2^+) \rightarrow 2_2^+$ transition and the 609-keV, $(2_2^+) \rightarrow 2_1^+$ one. The 1868-keV, $(2_2^+) \rightarrow 0_1^+$ decay was also observed both in the γ-ray singles spectrum and in the spectrum of γ rays in coincidence with the $(4_2^+) \rightarrow 2_2^+$ transition (Fig. 4.4(c)). The spectra in coincidence with the transitions in the prolate structure is presented in Fig. 4.4. The 279-keV and 1249-keV transitions were not previously observed in the two-neutron knockout [3] reaction that detected the 640-keV de-excitation from the same state. This is possibly because, in the case of the 279-keV transition, there is a poor peak-to-background ratio in this low-energy region of the spectrum. The 1249-keV de-excitation is part of a self-coincident doublet with the high-intensity 1260-keV one, making it difficult to observe without a large amount of statistics. While the 1260-keV transition appeared to be self-coincident in Ref. [3] in the two-neutron knockout reaction channel, they were unable to determine the exact energy of the self-coincident γ ray. No evidence of the 1256.8-keV self-coincident transition observed in β decay from the low-spin isomer of ^{70}Co in Ref. [43] was observed in this experiment.

The majority of the new 16 transitions placed into the level scheme de-excited higher-lying states of unknown spin-parity into states in the yrast sequence. The strongest of

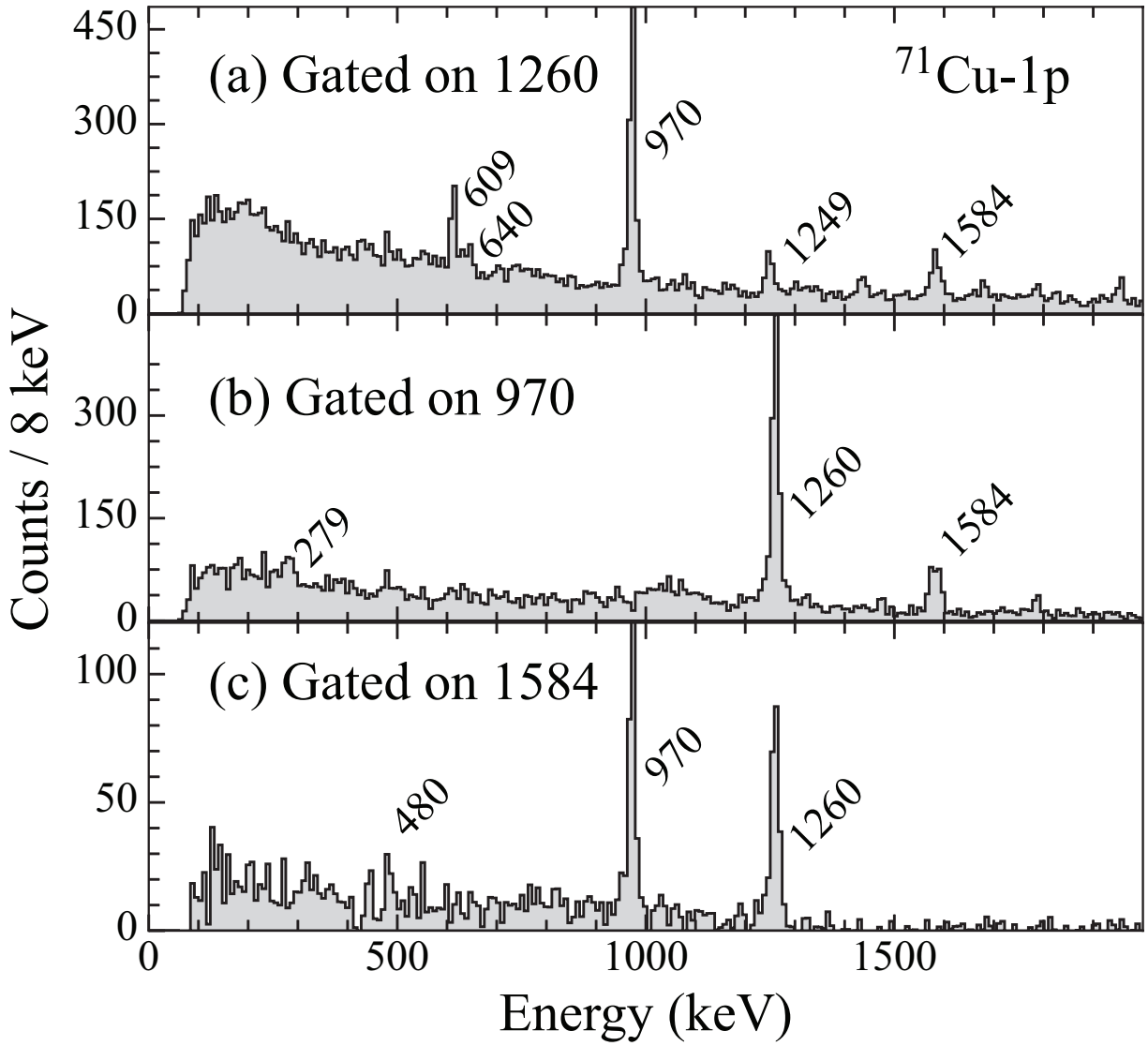

Figure 4.3: Sample of coincidence spectra used for placing transitions into Fig. 4.1 for the one-proton knockout reaction. Clear coincidences between the 1260-970-1584 keV transitions are observed, making it possible to place the 1584 keV transition in the level scheme. Also shown are a weaker 480 keV transition believed to feed into the newly placed 3814-keV state as well as several of transitions in the suspected prolate structure at 279 keV, 609 keV, 640 keV, and 1249 keV.

these transitions was a 1584-keV one, which de-excited a newly-placed 3814-keV level. The coincidence relationships used to place this transition are presented in Fig. 4.3. The spectrum in coincidence with the 1260-keV, $2_1^+ \rightarrow 0_1^+$ ground-state transition in panel (a) exhibits a

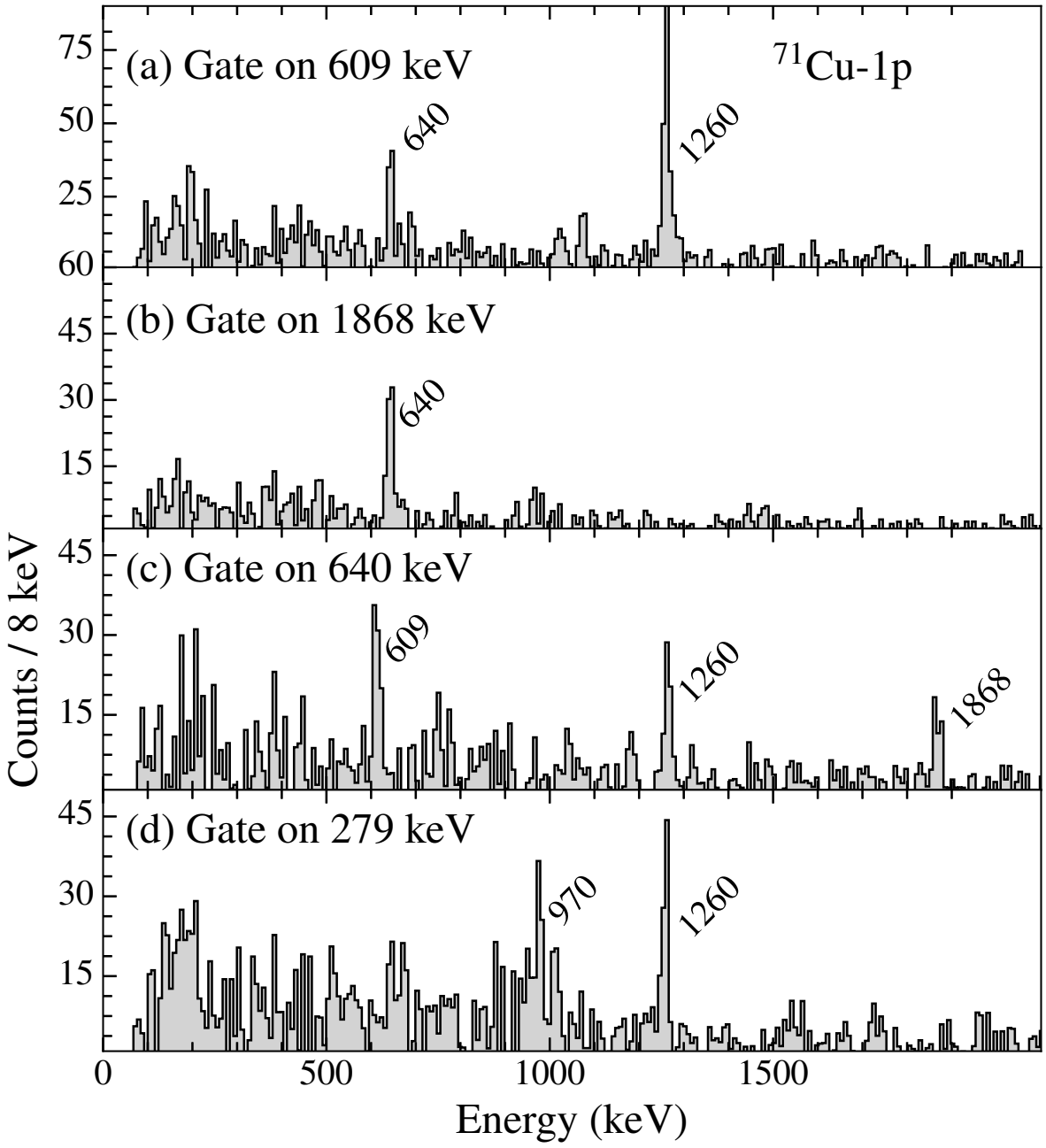

Figure 4.4: Coincidence spectra used for placing transitions in the suspected prolate structure in the ^{71}Cu one-proton-knockout reaction channel. Fig. 4.3 contains the associated spectra in coincidence with transitions in the yrast sequence.

clear coincidence between this transition and the 1584-keV transition. The 970-keV, $4_1^+ \rightarrow 2_1^+$ is also clearly coincident with the 1584-keV transition based on panels (b) and (c). Placing this 1584-keV de-excitation as feeding into the long-lived 6_1^+ state can be ruled out because the 1.51(4) ns lifetime [44] of this yrast state would make it impossible to observe the $4_1^+ \rightarrow 2_1^+$ and $2_1^+ \rightarrow 0_1^+$ de-excitations below it in the cascade in coincidence with the 1584-keV one if it did feed the 6_1^+ level. The 3814-keV state appears to only decay to the 4_1^+ state, as seen in Fig. 4.1. Because of the large amount of direct feeding to the 4_1^+ state and the available orbitals from which protons can be removed, it is possible that the 3814-keV level is a (5_1^+) state with a $\pi 1p_{3/2}^{+1} 0f_{7/2}^{-1}$ particle-hole configuration. A weaker, 480-keV de-excitation was observed in coincidence with the 1584-keV transition (see Fig. 4.3(c)), and was placed into the level scheme as being one of four possible decay branches from a newly placed 4293-keV state.

The 4293-keV and 4017-keV states are two newly proposed levels observed in the one-proton knockout. These exhibit considerably more branching to other states when compared to the aforementioned 3814-keV one, including strong, direct transitions to the 2_1^+ state. These possible decay branchings suggest that these states have spin $I \leq 4$.

The coincidence spectra for transitions from the 4293-keV and 3662-keV states are shown in Fig. 4.5. The strongest decay branch from the 4293-keV state is to the 2_1^+ level, with three marginally weaker transitions to the (5^+) level, the 4_1^+ level, and a 3662-keV one of unknown spin-parity. This suggests that the 4293-keV state has possible spin-parities of $(3^+,4^+)$. Based on similar arguments, the spin-parities of the 3662-keV and 4017-keV levels could be $(2^+,3^+,4^+)$, because in this case no transition connecting the (5^+) and these states is present to rule out the possibility of a 2^+ assignment. The spectra coincident with transitions from the 4017-keV and 2942-keV levels are shown in Fig. 4.6. The 2942-keV level

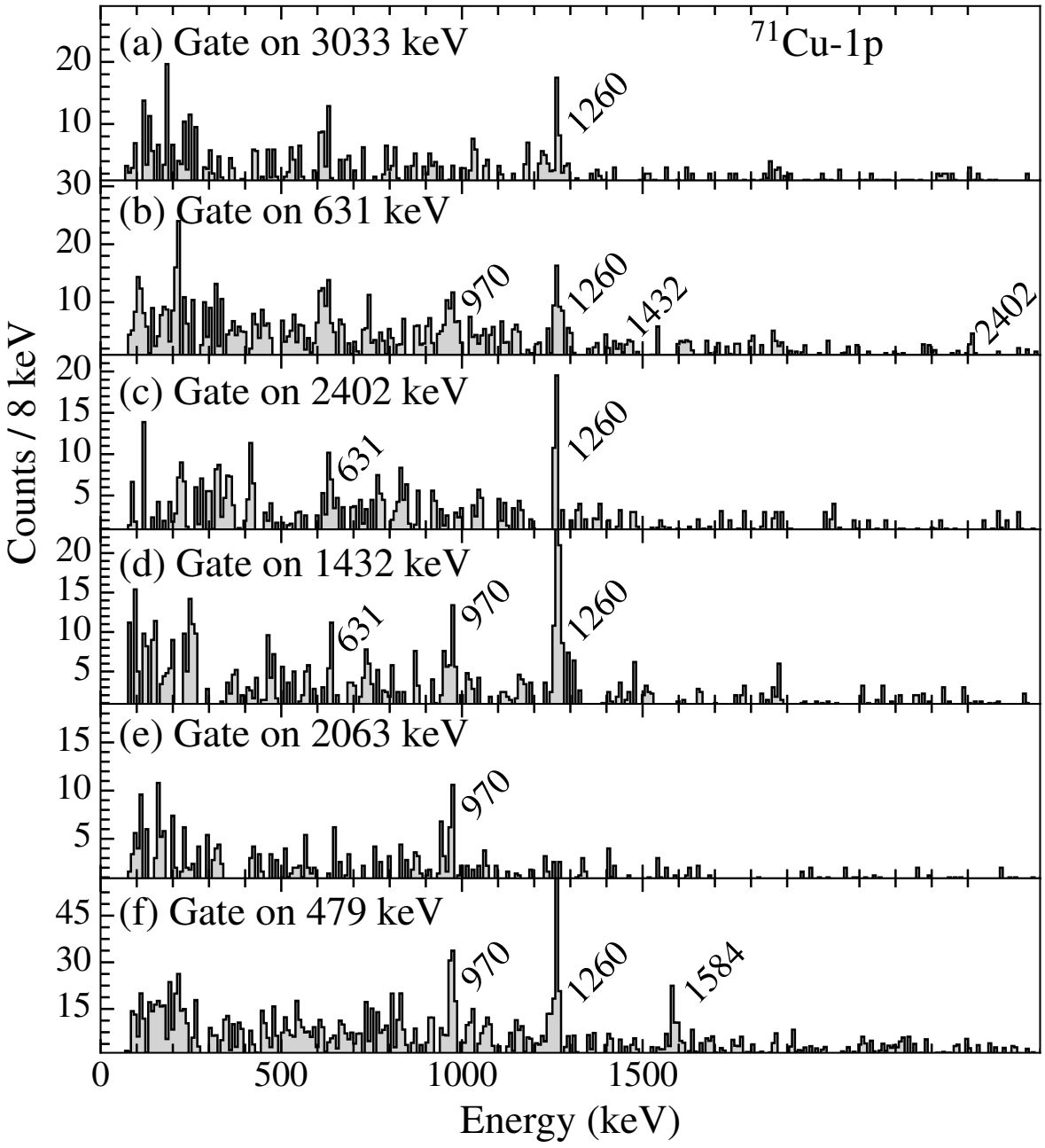

Figure 4.5: Coincidence spectra used for placing decays from the 4293-keV and tentative 3662-keV levels in the level scheme of Fig. 4.1 for the ^{71}Cu one-proton-knockout reaction channel.

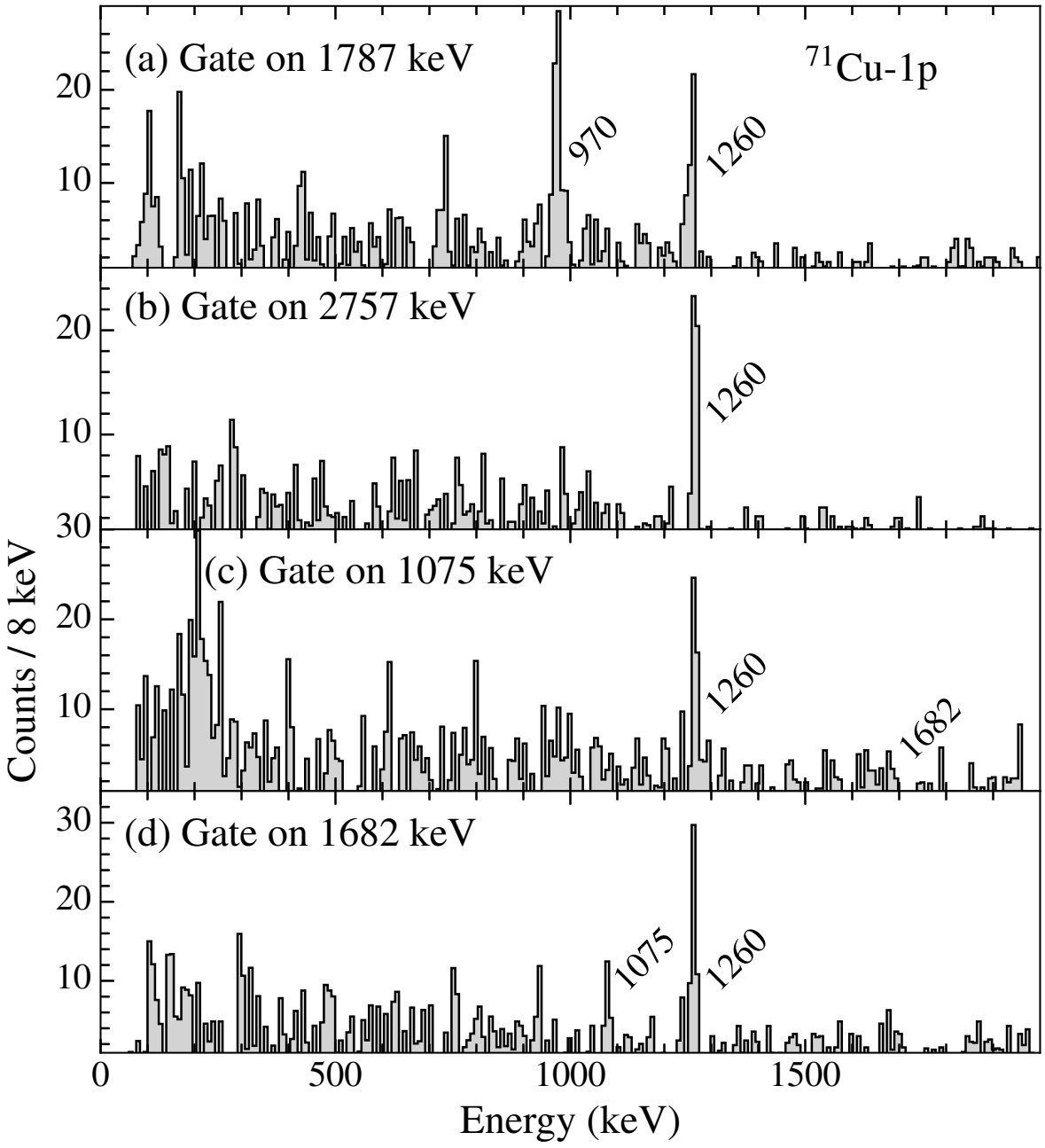

Figure 4.6: Coincidence spectra used for placing decays from the 4017-keV and 2942-keV levels in the level scheme of Fig. 4.1 for the ^{71}Cu one-proton-knockout reaction channel.

de-excites by a 1682-keV transition, which may correspond to a previously observed 1676-keV transition in the β decay of the $(1^+, 2^+)$ state of ^{70}Co [18, 45]. The source of the discrepancy

between the measured centroids is unclear. The 631-keV, 1075-keV, 1432-keV, and 2402-keV transitions are admittedly tentative placements due to the small measured intensities and weak coincidence relationships. Further complicating the placement of the 1075-keV γ ray is its position near the Compton edge of the high-intensity 1260-keV line.

The 1955-keV transition only appears to exhibit a coincidence relationship (see Fig. 4.7(a)) with the 1260-keV ground-state transition. This decay appears in all reaction channels, though it is strongest in the one-proton knockout reaction. It has been previously observed in a β decay measurement [45] following decay from the (1^+, 2^+) state of ^{70}Co and from two-neutron knockout [3]. Similar to the 1955-keV transition, the 2701-keV γ ray appears only in coincidence with the 1260-keV transition, as seen in Fig. 4.7(b). The 1321-keV transition exhibits a weak coincidence relationship with both the 970-keV and 1260-keV transition, as shown in Fig. 4.7(c). The 1321-keV and 2701-keV transitions had not been previously observed.

The 3846-keV transition was previously reported following the β decay of the low-spin isomer in ^{70}Cu, and was tentatively placed as feeding into the suspected prolate, 1868-keV, 2_2^+ state [46]. No coincidence relationships with this 3846-keV state were observed in this experiment. In fact, this transition was observed almost exclusively in events with detector multiplicity-1. Fig. 4.8 shows the spectra for events with detector multiplicity-1, -2, and -3 or higher. This absence of coincidence information and dominance in the detector multiplicity-1 spectrum supports the placement of this state as feeding into the ground state; however, it is possible that this state could decay into the isomeric (0_2^+) state at 1567 keV. It is unlikely that it would decay into the other known, higher-spin long-lived states, the 6_1^+ and 8_1^+ yrast levels, as the 3846-keV transition was observed in the β decay of the (1^+, 2^+) state of ^{70}Co. For comparison, presented in Fig. 4.9 is the 1260-keV transition with this same breakdown by

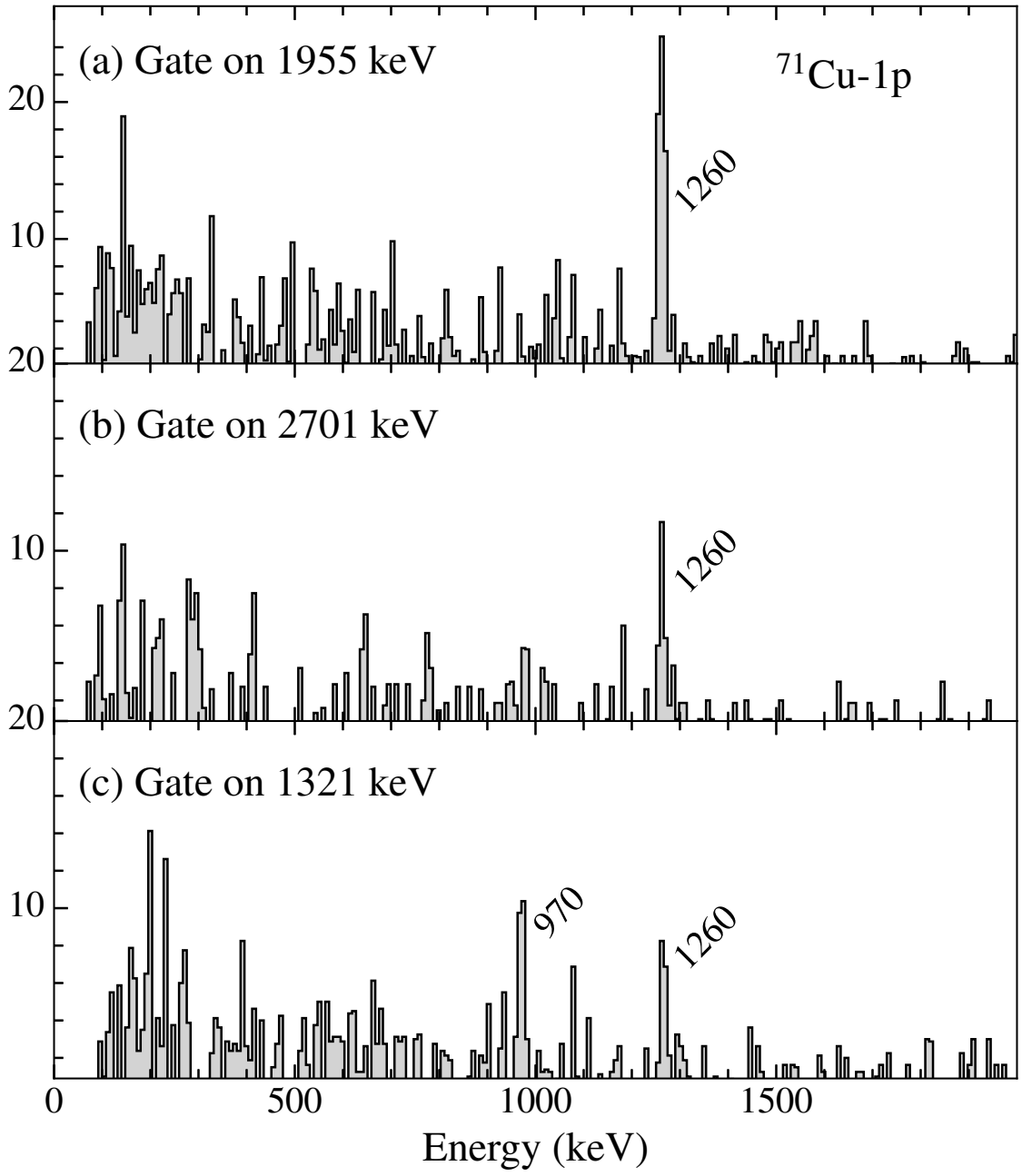

Figure 4.7: Coincidence spectra used for placing decays the 1955-keV, 2701-keV, and 1321-keV transitions in the level scheme of Fig. 4.1 for the ^{71}Cu one-proton-knockout reaction channel.

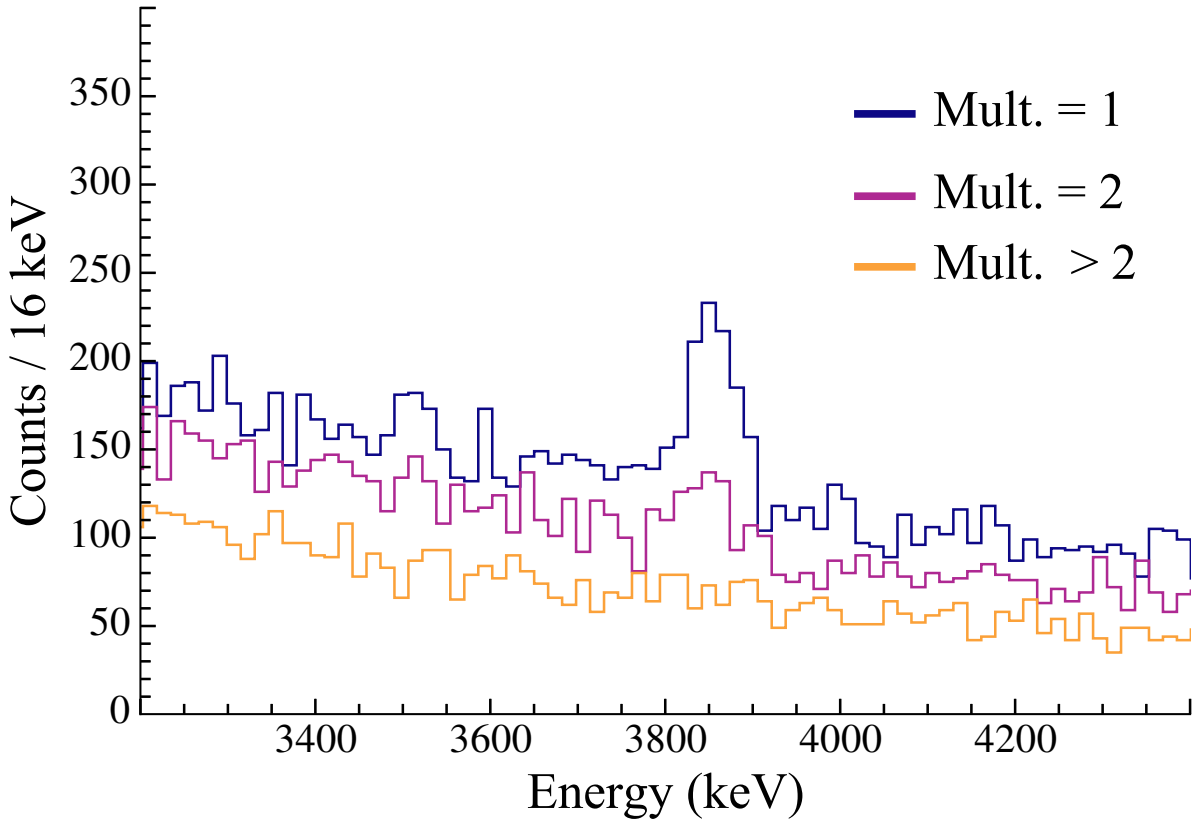

Figure 4.8: Spectra utilizing nearest-neighbor add-back from the one-proton-knockout reaction where the different lines correspond to different detector multiplicities. Note that the multiplicity is the corrected multiplicity after add-back; i.e., if an event only contains two hits and these are combined, it is a detector multiplicity-1 event. The dominance of the 3846-keV transition in the detector multiplicity-1 spectrum suggests that it could be a transition directly into the ground state, or some long-lived, low-spin state, as discussed in the text.

detector multiplicity. Because the 1260-keV transition is expected to appear in each possible detector multiplicity here, it is unsurprising that it is observed clearly in Fig. 4.9 in each.

As mentioned previously, all the transitions discussed so far for the one-proton knockout have been assumed to be from positive parity states, as negative-parity states are expected to be populated at much higher energies in this reaction channel. Surprisingly, a transition near 682 keV corresponding to the decay from the (5^-), 2912-keV state was observed in the proton-knockout reaction channel. As discussed in Section 4.2, this is possible due to

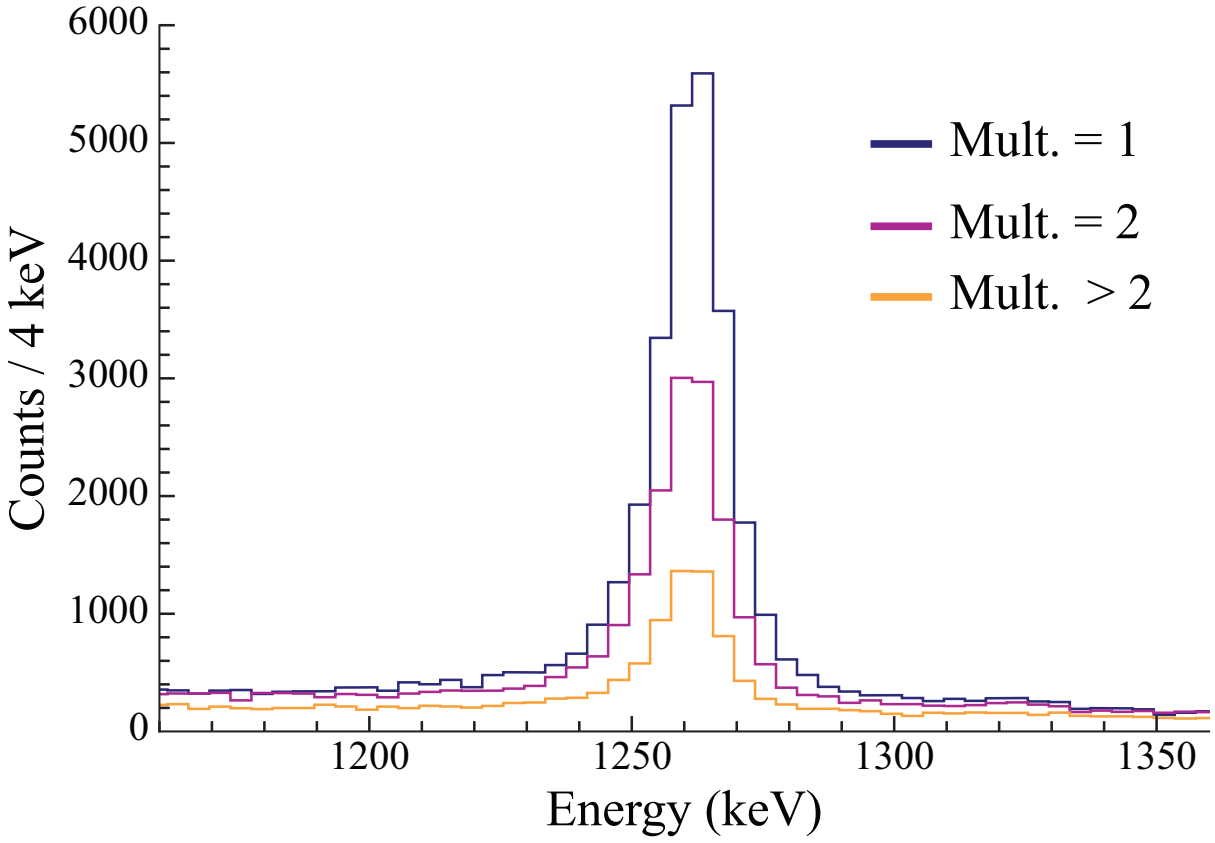

Figure 4.9: Spectra utilizing nearest-neighbor add-back from the one-proton-knockout reaction where the different lines correspond to different detector multiplicities. Note that the multiplicity is the corrected multiplicity after add-back; i.e., if an event only contains two hits and these are combined, it is a detector multiplicity-1 event. The appearance of the 1260-keV transition in each detector multiplicity spectrum is expected based on the number of different ways it can be populated in the one-proton knockout (see Fig. 4.1).

feeding from higher-lying states. This explanation is consistent with the aforementioned expectation that negative-states populated in the proton-knockout reaction at excitation energies below 6 MeV must be fed by positive-parity levels. The 682-keV transition appears to be a self-coincident doublet with a 676-keV transition. This was previously observed in the β decay of the high-spin (6^-, 7^-) state in ^{70}Co [18]. Only the sum of the counts in each peak could be determined by fitting the γ-ray singles spectrum because of insufficient resolution to resolve the peaks. Instead, the number of coincident transitions between the

two is determined utilizing nearest-neighbor addback by fitting the spectrum in coincidence with the two transitions and correcting for the NNDC adopted branching ratio [11] from the (5^-) state. The add-back factor was determined by simulating the 683-keV transition and determining the efficiency gain in nearest-neighbor addback compared to γ-ray singles. Because of the poor peak-to-background in the region, the intensity of the 234-keV decay branch could not be measured directly in the proton-knockout reactions. Instead, the aforementioned branching ratio was used to estimate the intensity of the 234-keV γ ray based on the measured 682-keV transition intensity. It was necessary to determine this intensity to determine the feeding-subtracted state populations used later in Section 5.1 to compare the different knockout reaction channels.

As noted in the previous paragraphs, the one-proton-knockout reaction can only populate negative-parity states at energies below 6 MeV, such as the 2912-keV (5^-) level, through indirect feeding from positive-parity states. Assuming the 676-keV transition and the 385-keV transition, which will be discussed in the following section, de-excite positive parity states, the population of the (5^-) level can be entirely attributed to indirect feeding in the proton-knockout reaction channels.

4.2 One-neutron knockout from ^{71}Ni

The one-neutron knockout reaction channel exhibited a different distribution of strength among final states than the proton-knockout one. The most interesting differences relative to the one-proton knockout are the decrease in the relative intensity of decays associated with the prolate structure, which is clear from Table 4.1, and increase both in the feeding-subtracted state population of the previously discussed (5^-) level and in the relative intensity

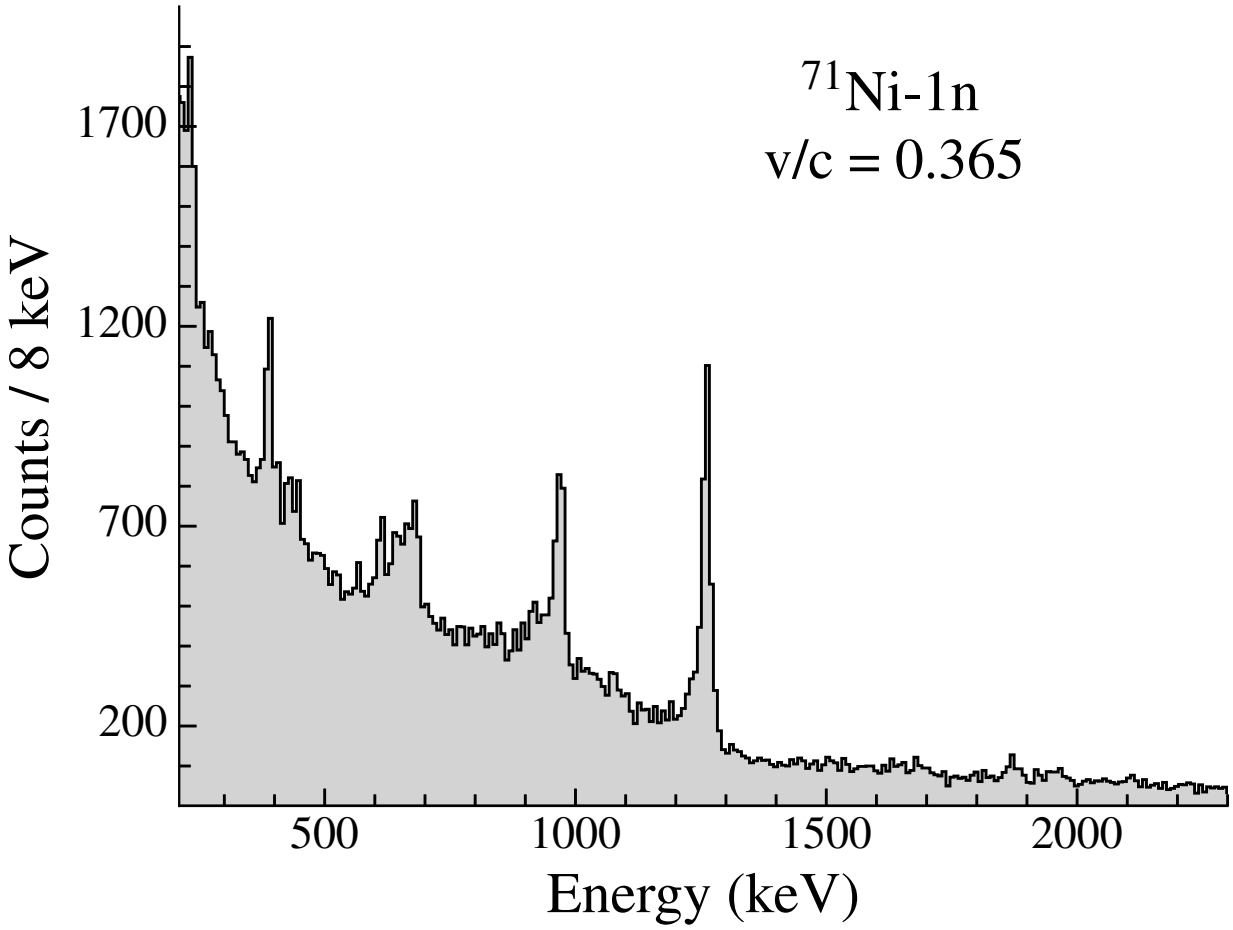

Figure 4.10: The Doppler-corrected γ-ray spectrum observed in coincidence with the ^{70}Ni residues after one-neutron knockout from ^{71}Ni. Clearly present in the spectrum are the 970-keV, $4_1^+ \rightarrow 2_1^+$ and 1260-keV, $2_1^+ \rightarrow 0_1^+$ transitions in the yrast sequence. Also visible are the previously unplaced 385-keV transition as well as the 682-keV γ ray associated with decay from the (5^-) state.

of the previously-unplaced 385-keV transition. These feeding-subtracted state populations are discussed in more detail in Section 5.1. The Doppler-corrected γ-ray spectrum observed for the one-neutron knockout reaction is shown in Fig. 4.10.

The 385-keV transition is the strongest unplaced peak in the one-neutron knockout reaction. It was present in both proton-knockout reaction channels, albeit weakly in the two-proton knockout one, and in the two-neutron knockout channel in a previous measure-

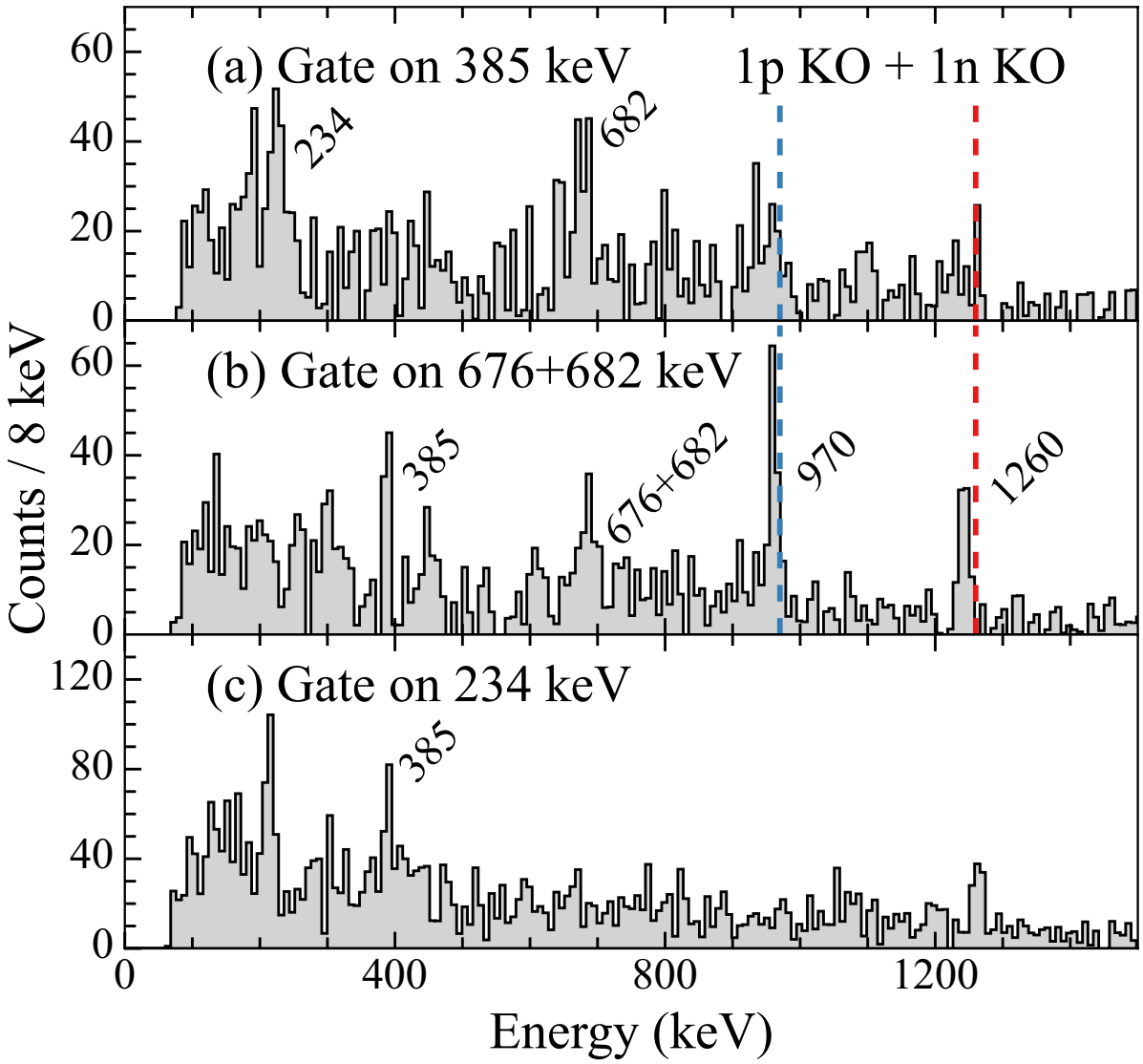

Figure 4.11: Coincidence spectra for the 385-keV, the 676-682 keV doublet, and the 234-keV transitions from the sum of the one-proton and one-neutron knockout reaction channels. Due to low statistics, it is only possible to tentatively place the 385-keV transition. The displacement of the yrast energies in panel (b), as indicated by the dashed lines at the expected yrast energies, is discussed in the text.

ment [3]. The 385-keV transition is placed based on the coincidence spectra in Fig. 4.11, where the coincident spectra from the one-proton and one-neutron knockout reactions are added together. The two-proton knockout channel was not included in the sum as the 385-keV intensity was considerably smaller for that reaction. In Fig. 4.11(a), the spectrum in

coincidence with the 385-keV transition appears to be coincident with the 234-keV and 682-keV transitions from the (5^-) state. The 676-keV transition, which is part of a self-coincident doublet with the 682-keV transition in the one-proton knockout reaction, is not observed in the one-neutron knockout channel.

The limited statistics in the coincidence spectra in Fig. 4.11 as well as the position of the 957-keV and 1247-keV peaks in Fig. 4.11(b), which are suspected to be the 970-keV and 1260-keV transitions in the yrast sequence, complicated the placement of the 385-keV transition. This shift of roughly 13 keV for these suspected yrast transitions from their expected energies is shown by the dashed lines at the expected transition energies in Fig. 4.11(b). Offsets in energy for Doppler-corrected γ-ray spectra can be caused by lifetime effects, as discussed in Section 2.3.5. To explore this possibility, a simulation of a cascade from the (5^-) state in ^{70}Ni through the 4_1^+ and 2_1^+ levels to the ground state was performed. The lifetime of the (5^-) state was varied and the resulting γ-ray spectrum was observed. To account for such an energy shift by a lifetime effect would require $\tau(5^-) \geq$ 75 ps. These offsets can account for some of the intensity of unplaced transitions such as the 957-keV transition in Table 4.2 as well as part of the intensity of the 1249-keV transition, which was placed into the prolate structure based on the self-coincidence in the one-proton knockout reaction channel (see Fig. 4.3). The statistics in the one-neutron reaction channel was insufficient to observe the expected coincidence relationship between the 1249-keV and the 1260-keV transitions.

Due to the presence of isomeric states in the level scheme for ^{70}Ni, some coincidence relationships cannot be observed. This is likely the reason some of the unplaced transitions in Table 4.2 remain unplaced. For example, the 915-keV de-excitation observed is the same energy as a known transition into the isomeric 6_1^+ state; however, there are insufficient statistics to identify any coincidence relationships. This is because the 2678-keV, 6_1^+ ($\tau =$

1.51(4) ns [44]) state decays within the bounds of GRETINA, but considerably after the target. As discussed in Section 2.3.5, this leads to a deformation of the Doppler-corrected γ-ray spectrum due to incorrect determination of velocity and emission angle. For states with even longer lifetimes, like the 2861-keV, 8_1^+ ($\tau = 335(1)$ ns) [11] state, the reaction residue would not decay before entering the S800 focal plane, making detection with GRETINA of the γ ray tagging the de-excitation impossible. Instead, it would be necessary to rely on gating on the detection of the 183-keV γ ray that signals the de-excitation from the isomer in the hodoscope (see Sec. 2.2.3). The hodoscope spectrum taken for the one-neutron knockout reaction channel is shown in Fig. 4.12. Unfortunately, although the 183-keV γ ray and subsequent cascade from the aforementioned isomeric state are observed, there were insufficient statistics to measure any coincidences between decays from the long-lived state in the hodoscope and prompt decays in GRETINA indicating feeding into this state.

A shell-model calculation was performed using the jj44pna [6] interaction for ^{70}Ni with a model space allowing only neutron excitations. The model space included the neutron $0f_{5/2}, 1p_{3/2}, 1p_{1/2},$ and $0g_{9/2}$ orbitals with the restriction that there were a minimum of two neutrons in the $0g_{9/2}$ orbital. The comparison between the experimental level scheme in Fig. 4.1 restricted to states observed in the one-neutron knockout and the results of the calculation are shown in Fig. 4.13. Listed to the right of the states is the shell-model spectroscopic factor for the knockout of a neutron from ^{71}Ni for all states with energies less than 4.5 MeV satisfying the restrictions on C^2S noted in the figure caption. The absence of the predicted prolate structure in the calculation is expected due to the absence of proton cross-shell excitations in the model space. The spectroscopic strength is highly fragmented to higher-lying, negative-parity levels, with minimal strength to positive parity states above the 8_1^+ yrast level. Due to this fragmentation of higher-lying strength primarily to negative-parity

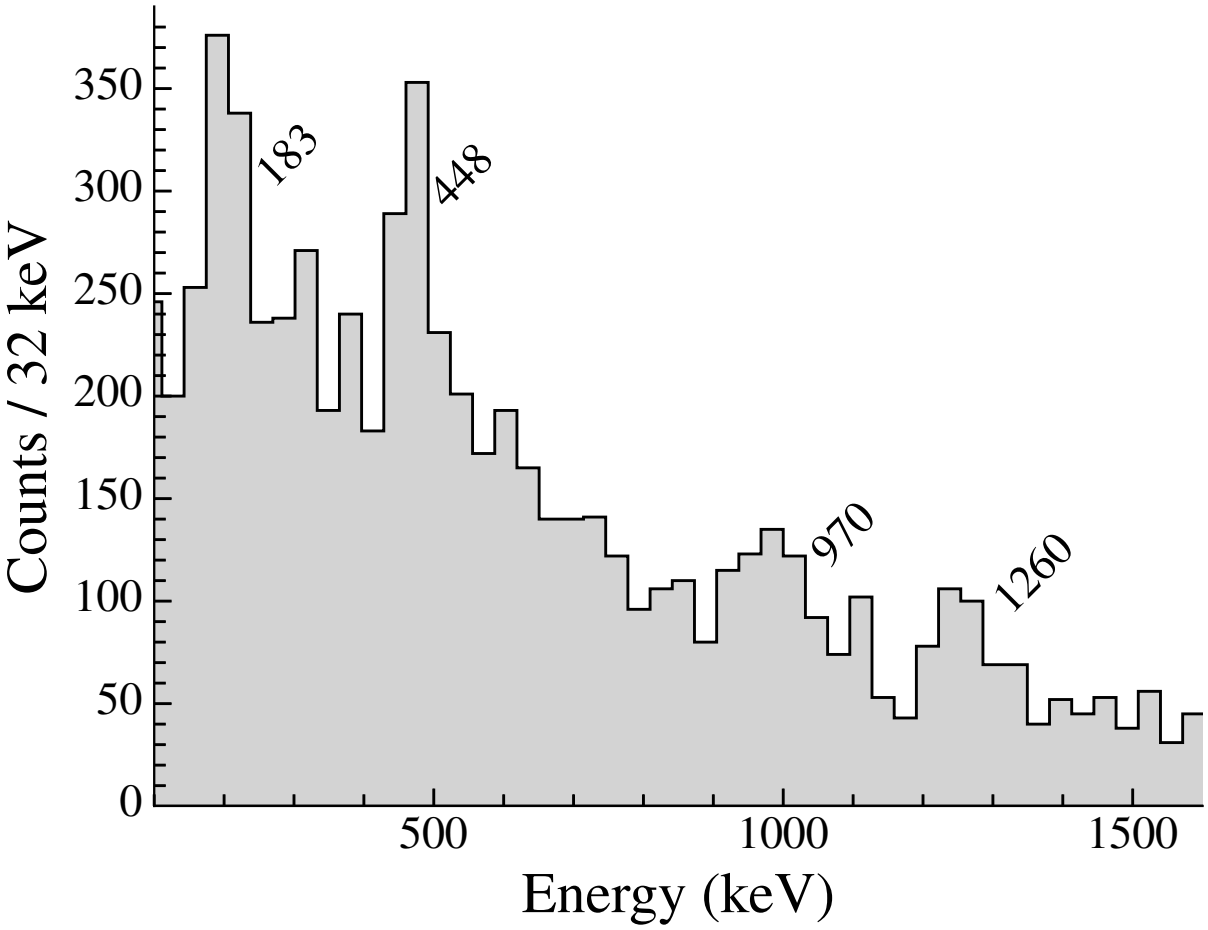

Figure 4.12: Gamma-ray spectrum from the hodoscope taken in coincidence with outgoing ^{70}Ni reaction residues following one-neutron knockout from ^{71}Ni.

states, it is possible that the unplaced transitions observed in the one-neutron knockout channel are de-excitations from negative-parity levels.

4.3 Two-proton knockout from ^{72}Zn

Because of the existence of isomeric states in the level schemes of the ^{71}Cu and ^{71}Ni beams that would affect the comparison between the final-state populations, the two-proton knockout reaction channel from ^{72}Zn, which exhibits no known long-lived level, was utilized. The

population distribution was similar to the one-proton knockout, as primarily decays from the yrast sequence and the suspected prolate levels were observed. The Doppler-corrected γ-ray spectrum from this reaction channel is shown in Fig. 4.14.

The 682-keV and 676-keV transitions cannot be separated in this reaction channel, similar to the situation in one-proton knockout (see Section 4.1). Furthermore, due to the considerable decrease in statistics relative to the one-proton knockout channel, the splitting between the two transitions cannot be determined in this setting using the coincidence relationship between the two decays. Instead, the splitting observed in the one-proton knockout channel is utilized. It is possible that this estimate of the intensity splitting is incorrect for this reaction channel. Using this splitting between the two decays, the expected intensity of the 676-keV transition in coincidence with the 682-keV transition would be below the experimental sensitivity for this reaction. Assuming there were no 676-keV decays in this setting would only increase the intensity for the 682-keV transition by 10%. Therefore, results reported in Table 4.1 utilize the assumption that the splitting between the intensities of the 676-keV and 682-keV is the same as that from the one-proton reaction.

A difficulty unique to the two-proton reaction channel in determining the intensity of the 682-keV transition is the presence of a structure with a large excess of counts near 700 keV, which is visible in Fig. 4.14. Based on the line shape, it is possible that this structure corresponds to either a 714-keV decay from a state with a significantly long lifetime or a number of unresolved transitions. Assuming this structure is a de-excitation from a state with a 75-ps lifetime leads to a 21% decrease in the measured intensity of the 682-keV transition compared to assuming that the 714-keV peak is a prompt transition. This large uncertainty is reflected in the measured intensities in Table 4.1 and Table 4.2 of the 682- and 714-keV transitions, as well as the that of the 676- and 234-keV lines, which are derived

from the intensity of the 682-keV de-excitation.

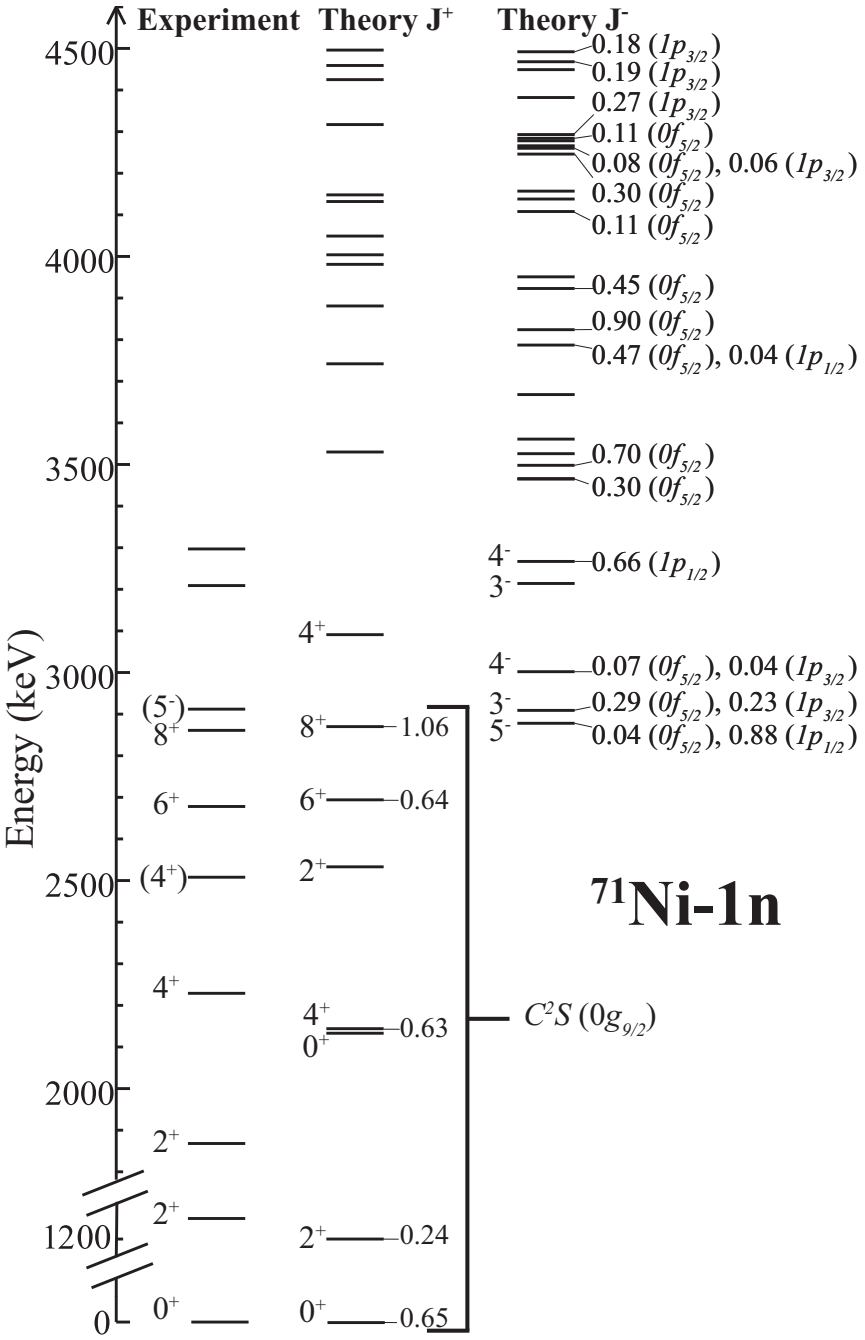

Figure 4.13: Comparison of experimental level scheme for states populated in the one-neutron knockout reaction channel to results of a traditional shell-model calculation only allowing neutron excitations using the jj44pna [6] effective interaction. For the positive-parity states, $g_{9/2}$ shell-model spectroscopic factors C^2S for one-neutron knockout from the ^{71}Ni ground state to individual ^{70}Ni final states are listed when $C^2S(0g_{9/2}) > 0.1$. For the negative-parity levels, the $0f_{5/2}, 1p_{3/2}, 1p_{1/2}$ shell-model spectroscopic factors are listed when $C^2S > 0.02$ for states where the sum $C^2S(0f_{5/2}) + C^2S(1p_{3/2}) + C^2S(1p_{1/2}) > 0.1$.

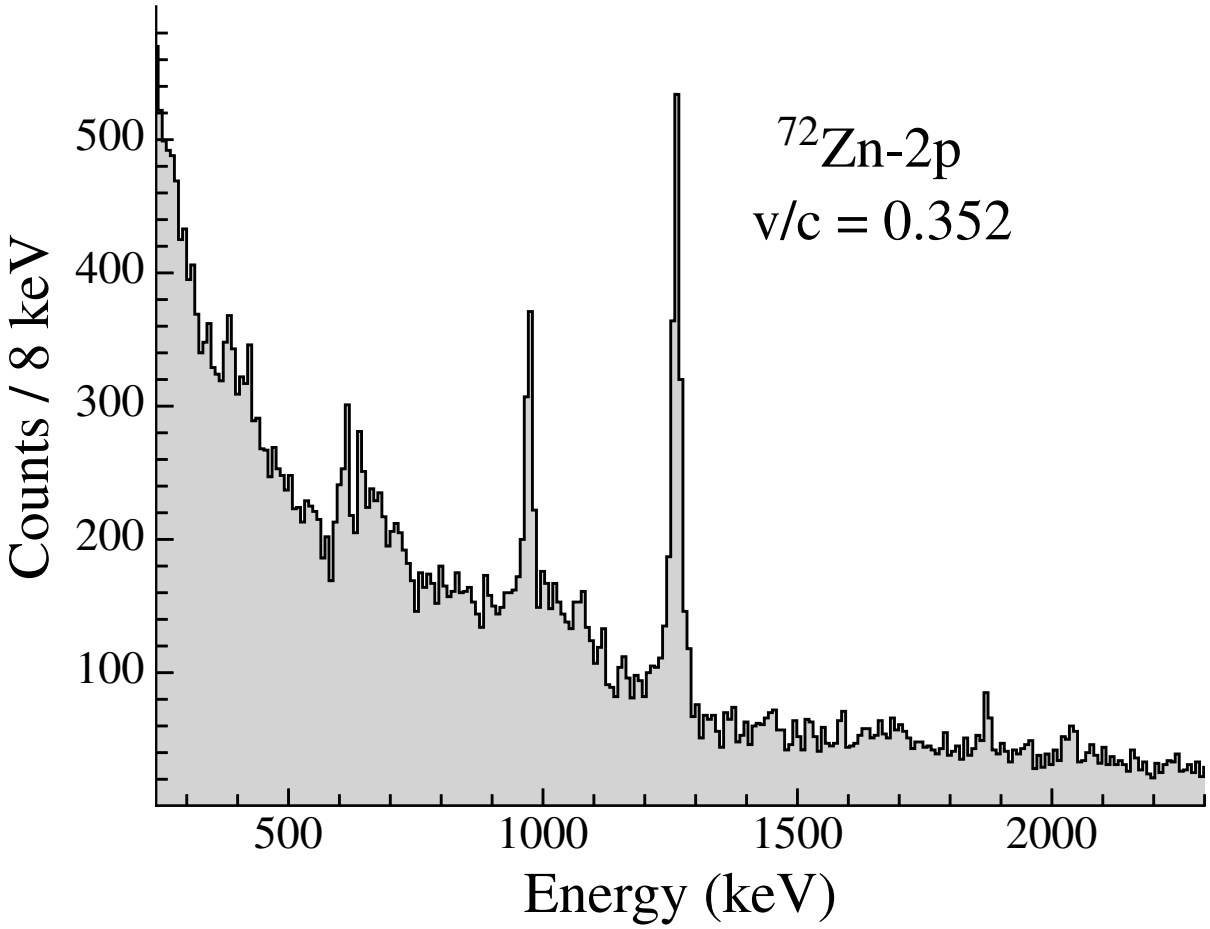

Figure 4.14: The Doppler-corrected γ-ray spectrum observed in coincidence with the ^{70}Ni residues after two-proton knockout from ^{72}Zn. Clearly present in the spectrum are the 970-keV, $4_1^+ \rightarrow 2_1^+$ and 1260-keV, $2_1^+ \rightarrow 0_1^+$ transitions in the yrast sequence. Also visible are the 609-keV, 640-keV, and 1868-keV γ rays associated with the predicted prolate structure.

Chapter 5

Comparison of reaction channels

The primary aim of this work was to probe the underlying single-particle configurations for excited states in ^{70}Ni by comparing the final-state population distributions following different reaction mechanisms. To this end, the γ-ray spectra and final-state, feeding-subtracted state populations will be compared in the following sections.

5.1 Comparison of γ-ray spectra

The Doppler-corrected γ-ray singles spectra detected in coincidence with ^{70}Ni beam-like knockout residues are compared in Fig. 5.1, where the Doppler-corrected singles spectra are presented normalized by the ratio of reaction residues in each setting to that of the two-proton knockout. There are clear differences between the spectra following the different knockout reactions, signaling differences in the in the population of excited final states following the different reactions. There is a much stronger relative intensity of the 385-keV transition in the one-neutron knockout channel compared to the proton-knockout ones. Multiple peaks, such as the 479- and 1584-keV γ rays, are only present in the spectrum from the one-proton knockout. The region between 600-700 keV exhibits structures with considerably different intensity distributions between the different reaction channels. While the behavior near 200 keV is dramatically different in the one-proton knockout, it was not possible to determine any coincidence relationships with the structure here due to the poor peak-to-background

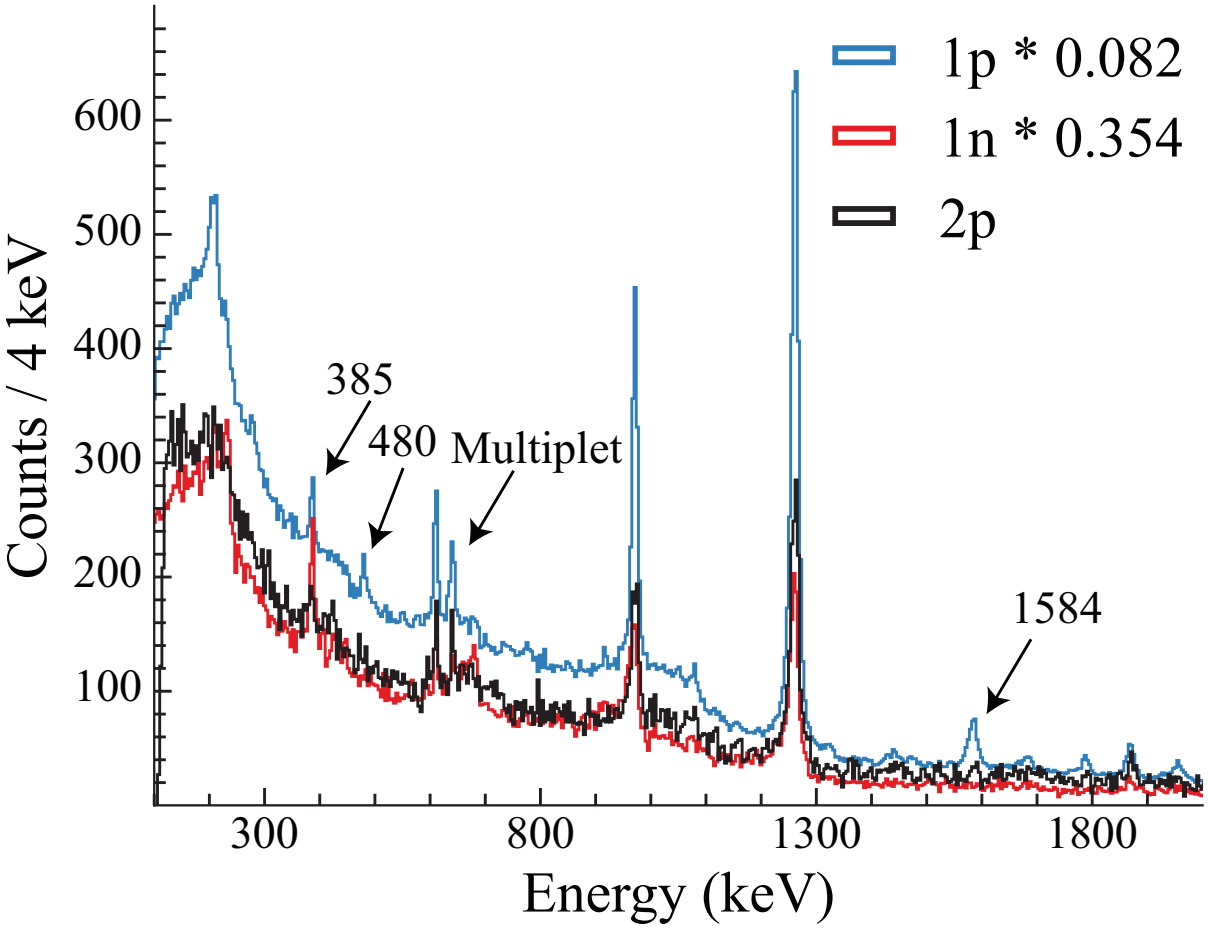

Figure 5.1: Comparison of Doppler-corrected γ-ray singles spectra in coincidence with detection of ^{70}Ni knockout residues. The spectra are scaled based on the detected number of ^{70}Ni residues in each setting relative to the number detected in the two-proton knockout channel. The scaling factors are listed in the legend.

ratio at this energy. The peak-like structure lines up with the energy expected to be in coincidence with the Compton edge of the strong 1260-keV transition.

5.2 Comparison of feeding-subtracted state populations

To probe the differences in the single-particle configurations of the states associated with the prolate structure, the direct population of states is explored in Fig. 5.2. In this figure, the intensities were first corrected for observed feeding from higher-lying levels. Then, these were turned into relative intensities by dividing by the number of ^{70}Ni reaction residues detected in the reaction channel being considered. Finally, the differences in these feeding-subtracted relative intensities divided by their sum was used to compare the one-proton and one-neutron channels (circles) and the two-proton and one-neutron ones (squares). In this way, points above (below) the line correspond to states which exhibited more direct feeding from proton (neutron) knockout. Note that only levels that were populated in each reaction channel are shown in Fig. 5.2. One notable exclusion is the 3214-keV level, which was dominantly populated in the one-proton knockout.

Figure 5.2 suggests that the prolate states were populated more strongly in the proton knockout channels, which is consistent with the picture that the prolate levels are associated with cross-shell proton excitations. Although states in the yrast sequence also appear to have a larger direct population following proton knockout, this can also be explained by either incomplete feeding subtraction due to unplaced transitions or neutron knockout populating both long-lived positive parity states, such as the 6_1^+ and the 8_1^+ levels, and higher-lying negative-parity states which decay into these isomeric ones. Furthermore, the populations are consistent with the expectation that the negative-parity states, such as the (5^-) one, can

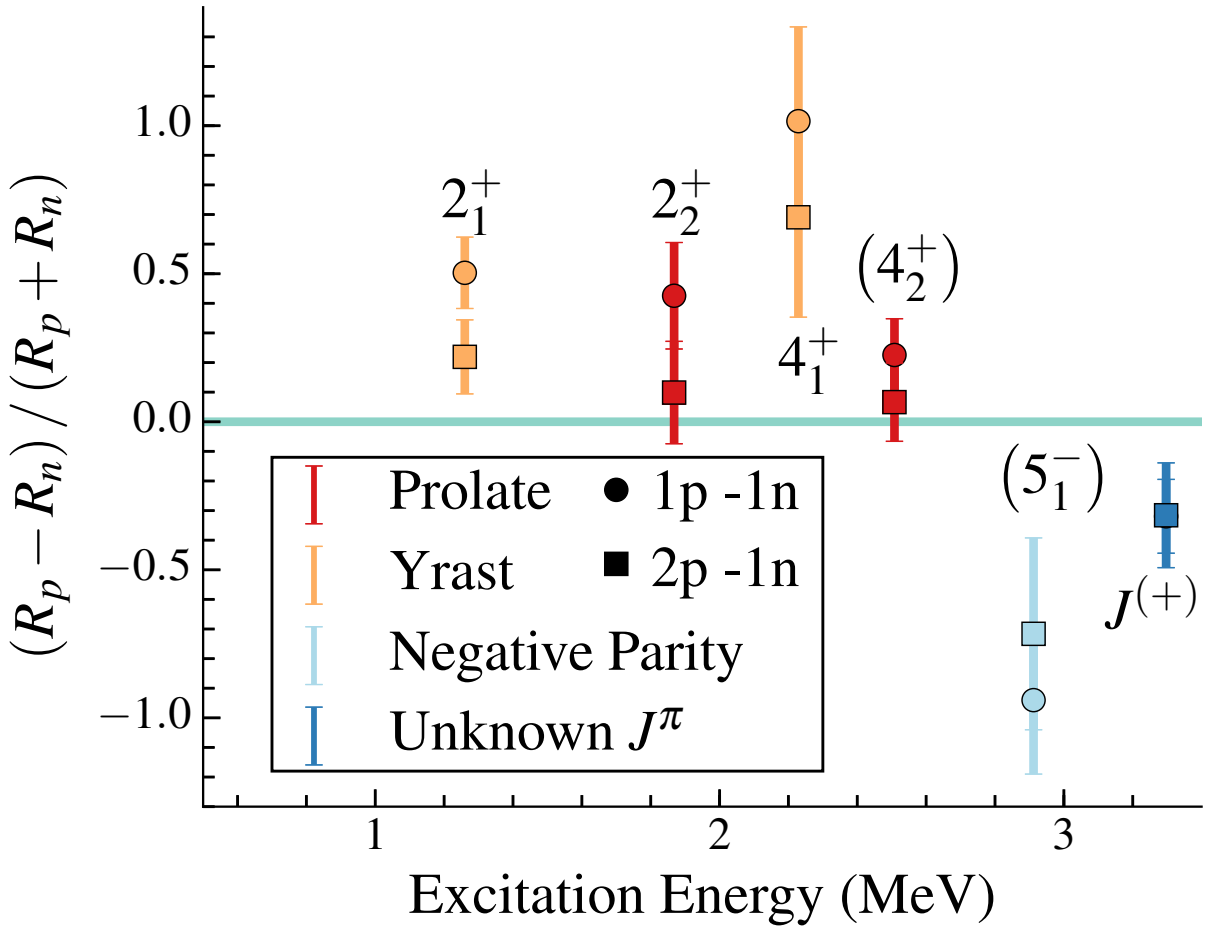

Figure 5.2: Comparison of feeding-subtracted state populations between the proton knockout and neutron knockout. The populations were divide by the number of ^{70}Ni knockout residues detected in the channel under consideration. Plotted is the difference over the sum of these relative populations comparing both proton knockout reactions with neutron knockout.

only be directly populated in the neutron knockout reaction.

Marked as the $J^{(+)}$ state in Fig. 5.2, the newly-placed, 3297-keV level, which de-excites by the 385-keV transition, appears to be populated primarily in the neutron-knockout reaction. This transition, as well as a 676-keV one, were previously speculated in Ref. [3] to be candidates for the $2_2^+ \rightarrow 0_2^+$ transition because these γ rays were observed in the two-neutron knockout reaction channel but absent in the deep-inelastic scattering data. The placement of the 385-keV transition as feeding the (5^-) state contradicts this idea. Furthermore, the 676-keV reconstructed transition energy observed in Ref. [3] is compatible with a 682-keV γ ray emitted from a long-lived ($\tau \geq 75$ ps) state. Reference [18] placed the the (0_2^+) state at 1567 keV, resulting in an expected energy of 301 keV for the $2_2^+ \rightarrow 0_2^+$ transition. These observations along with the observed coincidence relationships with the 682-keV, $(5^-) \rightarrow 4_1^+$ transition makes the association with the proposed prolate structure unlikely. Unfortunately, at this level of statistics, the suspected small branching ratio due to competition with the higher-energy 1868-keV and 609-keV transitions precluded any detection of the $2_2^+ \rightarrow 0_2^+$ one in this measurement.

Chapter 6

Summary and future work

In agreement with expectations, the population of the observed levels in ^{70}Ni following one- and two-nucleon knockout reactions was found to depend on the reaction channel. By observing the difference in final-state populations following the different nucleon knockout reactions, it was possible to determine which states exhibited configurations dominated by either proton or neutron excitations. As previously suggested [3], the proposed prolate structure appears to be dominantly populated through cross-shell proton excitations across the $Z = 28$ shell gap. Based on its relatively high intensity feeding the 4_1^+ state and the available orbitals from which protons can be removed, the level at 3813 keV also appears to exhibit proton particle-hole character, and has been tentatively assigned a spin-parity of (5^+).

The previously observed [3] (5^-) level as well as the newly-proposed tentative 3297-keV one that decays through the 385-keV γ ray are populated more strongly in the one-neutron knockout, suggesting that these are associated with neutron excitations. Two γ rays, the 676- and 385-keV transitions, which were previously speculated [3] as possible candidates for the $(0_2^+) \rightarrow 2_1^+$ decay based on their appearance in two-neutron knockout and absence in deep-inelastic scattering, appear to be unrelated to the suspected prolate structure based on the results of this work. There were 14 observed yet unplaced transitions, which may feed into the several isomeric states of ^{70}Ni. In total, 16 transitions, including two transitions within

this proposed prolate structure, and 7 levels were added to the level scheme of ^{70}Ni. Due to the high level densities involved, the presence of several isomers in the level scheme of ^{70}Ni, the mostly unknown or tentative final-state quantum numbers, and the complex associated configurations, it was unfortunately not feasible to probe the spectroscopic factors in this measurement.

For the determination of the isomeric content in the incoming ^{71}Ni beam, the precision of the result will be improved when more precise results on the β-decay branching ratio from the isomeric state of ^{71}Ni are available. Because the current values from the NNDC database [11] are only upper limits on this branching ratio, it is only possible to determine the lower limit of the isomeric content of the incoming ^{71}Ni secondary beam (see Section 3.4). A more precise measurement would make it possible to definitively determine the amount of isomeric content, and therefore determine the amount that long-lived states in the incoming ^{71}Ni beam can affect the final-state populations.

The prolate nature of the previously-mentioned states is inferred solely from shell-model calculations [16], and therefore one avenue for future inquiries would be a direct, experimental determination of the quadrupole properties of the suspected prolate states; e.g., using sub-barrier Coulomb excitation. Sub-barrier Coulomb excitation, which involves inducing nuclear excitations through the electromagnetic field acting between nuclei, makes it possible to measure the quadrupole moment. The magnitude of the quadrupole moment quantifies the amount of deformation and its sign determines whether a state is oblate or prolate. This measurement will require next-generation facilities like the Facility for Rare Isotope Beams (FRIB), as reaccelerated ^{70}Ni can currently only be produced at a rate of a few particles per second, many orders of magnitude less than for the fast-beam experiments described in this work.

Another complementary approach for probing the structure of the low-spin states in ^{70}Ni would be to use the two-neutron transfer reaction (t,p) in inverse kinematics as was recently done for ^{68}Ni [47]. It would be possible to determine the angular momentum transfer of the reaction based on the observed angular distribution for the protons. Therefore, because the excitation energy of ^{70}Ni would be accessible based on the energy and detection angle of the recoiling proton, the underlying configurations of different excited states in ^{70}Ni could be probed. In particular, it may be possible to observe population of the 0_3^+ state near 2.5 MeV, which was predicted with traditional shell-model calculations [3] with a model space only permitting neutron excitations. Such an experiment will likely only be possible at FRIB due to the required beam intensity of reaccelerated ^{68}Ni.

Determining the properties of nuclei with more extreme neutron-proton asymmetry will be a major goal of nuclear physics moving forward. Approaching the limits of nuclear stability, the doubly-magic nucleus ^{78}Ni will be one major focus of future investigations. Already, it is predicted that ^{78}Ni exhibits shape coexistence, with a first excited state of spin-parity 0^+, and acts as a "portal" to a new island of inversion at $N = 50$ [20]. These predictions have been supported by experimental results from (p, 2p) and (p, 3p) reactions [21]. Performing experiments to probe the properties of nuclei beyond ^{78}Ni at the extremes of the nuclear chart will become possible with FRIB.

APPENDICES

APPENDIX A

INTERMEDIATE-ENERGY COULOMB EXCITATION OF ^{88,90}KR AND ^{86}SE

Using nucleon knockout, it was possible to probe shape coexistence and the configurations associated with the excited states in ^{70}Ni using the single-particle degree of freedom. A complementary approach to this type of problem is Coulomb excitation, which looks at the *collective* degree of freedom directly. Collectivity refers to the participation of multiple nucleons to excitation modes in nuclei, with the most common examples of collective motion in nuclei being vibrational or rotational. Two indicators of quadrupole collectivity for even-even nuclei are the energy of the first excited 2^+ state and, more importantly, the electric quadrupole transition strength from the ground state to the first excited 2^+ state; i.e., $B(E2; 0_1^+ \rightarrow 2_1^+)$, introduced in Section 1.1.2. A low 2_1^+ state energy or a large $B(E2)$ value compared to neighboring nuclei along an isotopic chain signals the onset of deformation. In an effort to probe collectivity beyond the $N = 50$ shell closure in neutron-rich krypton and selenium isotopes, an intermediate-energy Coulomb excitation was performed to measure the $B(E2; 0_1^+ \rightarrow 2_n^+)$ values in ^{88,90}Kr and ^{86}Se. The results of this measurement were published in Physical Review C [48].

This measurement resulted in considerably reduced uncertainties for the quadrupole transition strength in ^{90}Kr and ^{86}Se, as well as the first published result for this value in ^{88}Kr. There was considerable fragmentation of the strength to higher-lying 2^+ levels observed for the krypton isotopes. This fragmentation confirmed the results of a shell-model calculation in the $\pi(fpg) - \nu(sdgh)$ shell with an only minimally-tuned effective interaction based on a nucleon-nucleon interaction derived from effective field theory and effective charges adjusted to reproduce the $B(E2)$ value in singly-magic ^{86}Kr.

Experimental motivation

Neutron-rich nuclei in the Se, Kr, Sr, and Zr isotopic chains all exhibit an onset of deformation when charting their properties from $N = 50 - 60$; however, this onset manifests differently for the different chains. For $_{38}$Sr and $_{40}$Zr, there is a rapid increase in collectivity at $N = 60$, which is evident in Fig. A.1 by the large increase in the transition strength and in Fig. A.2 by the noticeable decrease in the 2_1^+ level energy. In the context of ^{100}Zr, the phenomena has been referred to as a quantum phase transition [49–51]. This rapid onset of deformation can be explained by the downsloping $\pi g_{9/2}$ intruder orbit, which becomes more bound due to the proton-neutron tensor force as neutrons are added above the $N = 50$ shell closure.

In comparison, the $_{34}$Se and $_{36}$Kr isotopic chains were expected to exhibit a more gradual evolution of collectivity; however, in the case of ^{90}Kr, the large uncertainties for the measured values precluded making definitive statements concerning collective behavior. For ^{88}Kr, the adopted value suggested a slight decrease in collectivity with two neutrons added above the shell closure, which is a surprising result. Comparably little is known concerning

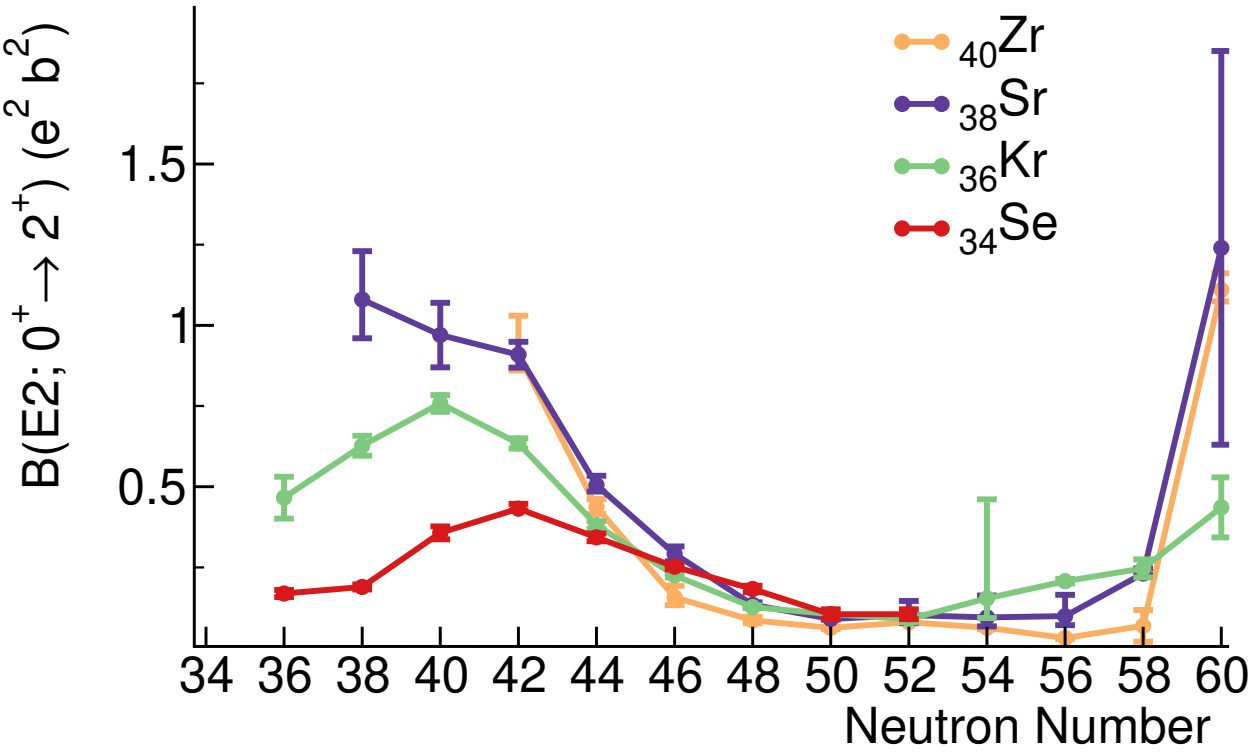

Figure A.1: Adopted $B(E2; 0_1^+ \rightarrow 2_1^+)$ values from Ref. [8], except for the value for ^{98}Zr and ^{86}Se. In the case of the former, the value is based on a more recent Coulomb excitation experiment [9] that determined the upper bound for the strength, where previously only a lower limit had been reported. In the case of the latter, the value is taken from a recoil-distance Doppler shift measurement [10].

the collective properties of neutron-rich Se beyond $N = 50$, with information limited to excitation energies in $^{86-94}$Se [52–54], a measurement of the $B(E2\uparrow)$ value in ^{84}Se using Coulomb excitation [55], and lifetimes of excited states in ^{84,86}Se measured using the recoil-distance Doppler shift technique [10]. To determine $B(E2)$ values with considerably lower uncertainties compared to previously measured values and investigate the possible decrease of collectivity in ^{88}Kr, we used intermediate-energy Coulomb excitation. Before discussing this, we will do a quick aside on the units and conventions used for reporting $B(E2)$ values.

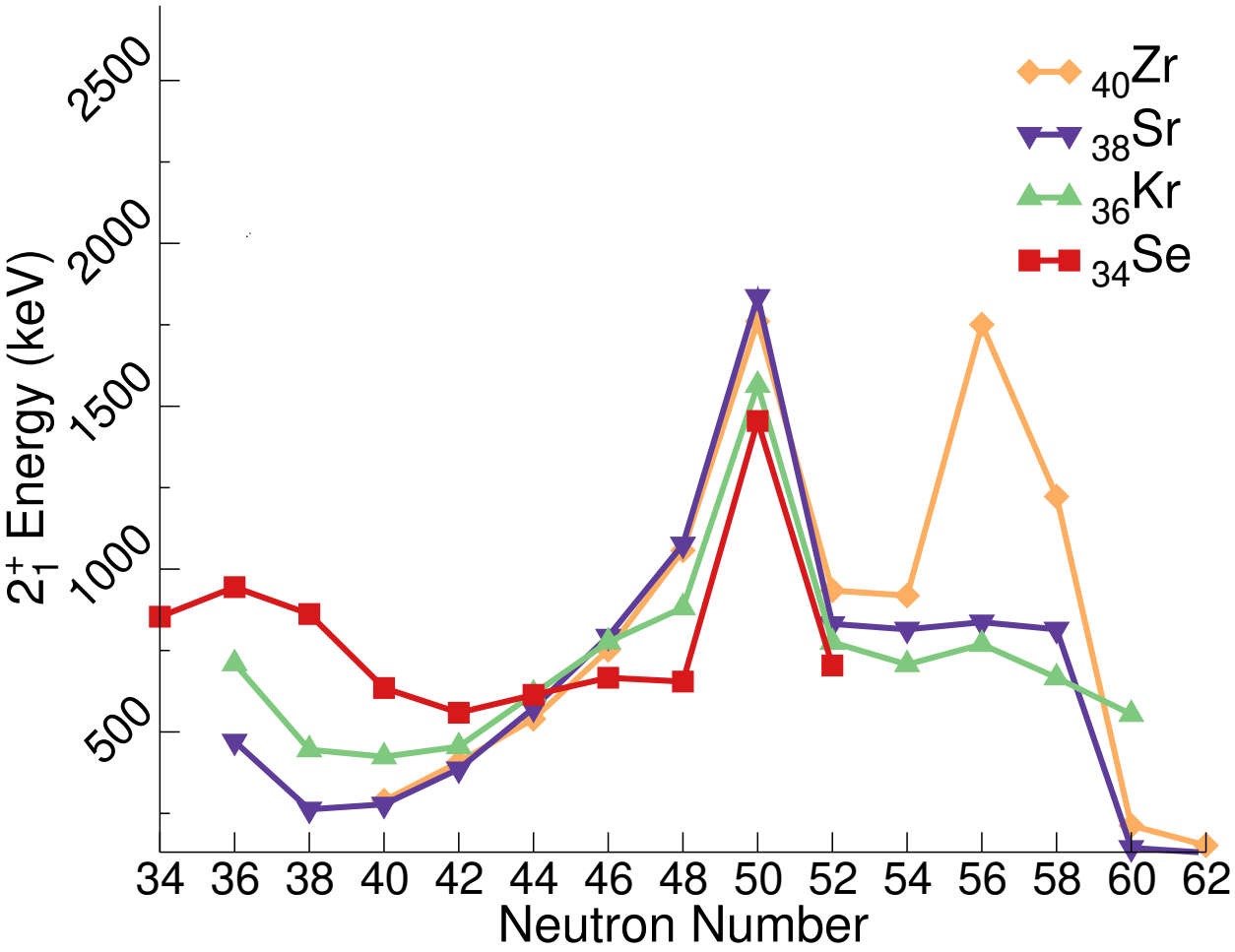

Figure A.2: Adopted energies from the NNDC database [11] for the 2_1^+ level for the discussed even-even nuclei.

Units and conventions for $B(E2)$ values

It is important to note that electromagnetic transition strengths $B(\pi\lambda)$, where $\pi \in E, M$ and $\lambda = 0, 1, 2, 3...$ and which are also known as reduced transition probabilities, are often reported using a variety of different units and conventions. Focusing on $B(E2)$ values, which are the most relevant quantities when discussing intermediate-energy Coulomb excitation of even-even nuclei, these will be covered briefly here. For more detail, see Ref. [13].

First, it is important to note that the strengths can be written in terms of either excitation

($B(E2\uparrow)$) or decay ($B(E2\downarrow)$), and the relationship is:

$$B(J_1 \rightarrow J_2) = \frac{2J_2+1}{2J_1+1} B(J_2 \rightarrow J_1) \tag{A.1}$$

Therefore,

$$B(E2; 0_1^+ \rightarrow 2_1^+) = 4B(E2; 2_1^+ \rightarrow 0_1^+) \tag{A.2}$$

In this work, all transition strengths are reported as excitations; i.e. $B(E2) = B(E2; 0_1^+ \rightarrow 2_1^+)$. In terms of units, two types will be used in this work: in the case of Fig. A.1, the units used are e^2b^2, which can be converted to other commonly used unit e^2fm^4 by noting that 1 barn = 100 fm^2, and therefore 1 b^2 = 10000 fm^4. Weisskopf units (W.u.), also called single-particle units, are commonly used units that are an estimate of the mass-dependent decay strength for a single neutron or proton. Although it is at best an approximation, one can think about the number of Weisskopf units as the number of nucleons contributing to a decay. So a large number of Weisskopf units suggests a highly collective decay, while a smaller number would suggest single-particle behavior. One $B(E2)$ Weisskopf unit for a nucleus of mass A is defined as:

$$B_{s.p.}(E2) = \frac{9}{100\pi} \left(1.2A^{1/3}\right)^4 e^2fm^4 \tag{A.3}$$

So, to determine the number of Weisskopf units for a given measured $B(E2\downarrow)$, simply calculate $B(E2\downarrow)/B_{s.p.}(E2)$. Note that these units are only used for decays, not excitations.

Intermediate-energy Coulomb excitation

Intermediate-energy Coulomb excitation [56–58] involves sending a projectile of interest at a high-Z target. The projectile is excited in the strong electric field of the target, and then de-excites by emitting a γ ray. By measuring the intensity of the γ rays tagging the electromagnetic interaction, the angle-integrated Coulomb excitation cross section can be determined. The electric quadrupole transition strength is then determined using the Alder-Winther theory of relativistic Coulomb excitation [12], which relates $B(E2)$ values to the cross section.

It is important to note that the energies used in intermediate-energy Coulomb excitation are above the Coulomb barrier. Because of this, analysis must be restricted to peripheral collisions to avoid nuclear contributions to the cross section. This is accomplished experimentally by restricting analysis to events with a sufficiently small scattering angle; i.e., a large impact parameter. The choice of the touching-spheres approximation + 2 fm has been shown to be sufficient to ensure that the nuclear contribution is minimized [58–60]. The touching spheres approximation is given by:

$$b_{\text{min}} > R_0(A_{\text{targ}}^{1/3} + A_{\text{proj}}^{1/3}) \tag{A.4}$$

where $R_0 = 1.25$ fm is the nuclear radius factor. Through kinematics [12], the minimum impact parameter b_{min} is translated into a maximum scattering angle and used to restrict the data.

At the relativistic beam energies used for intermediate-energy Coulomb excitation, multistep excitations are greatly hindered, unlike in classic low-energy Coulomb excitation. This results in only 2^+ states connected to the ground state by a sufficiently strong branch being

populated in the experiment. Typically, this means only the 2_1^+ level is populated; however, in this experiment, we observed significant strength to higher-lying 2^+ states in ^{88,90}Kr. We determine the angle-integrated Coulomb excitation cross sections for each state based on the γ-ray intensities of the de-exciting transitions relative to the number of projectiles and number density of the target. This complicates the typical intermediate-energy Coulomb excitation analysis, in which only the first 2^+ state is observed, because the feeding through $2_n^+ \rightarrow 2_1^+$ transitions has to be subtracted to determine the cross section to the 2_1^+ one, and branching ratios for the decays to the ground state and to the 2_1^+ level from the 2_n^+ levels have to be taken into account.

Experimental details and devices

The experiment was performed at the Coupled Cyclotron Facility in the National Superconducting Cyclotron Laboratory [27] at Michigan State University. A stable ^{96}Zr primary beam was accelerated to 120 MeV/nucleon by the K500 and K1200 coupled cyclotrons. The primary beam impinged on a 364, 374, or 255 mg/cm^2 ^{9}Be production target to produce ^{88}Kr at 67 MeV/nucleon, ^{90}Kr at 68 MeV/nucleon, and ^{86}Se at 79 MeV/nucleon, respectively, through projectile fragmentation. An aluminum wedge degrader with areal density 200 mg/cm^2 located at the mid-acceptance position of the A1900 fragment separator [29] was used to select the fragments of interest from the secondary beam cocktails.

The S800 spectrograph

The selected fragments were delivered to the analysis line of the S800 spectrograph [30]. At the target position of the spectrograph, a 246 mg/cm^2 ^{209}Bi foil was used to induce

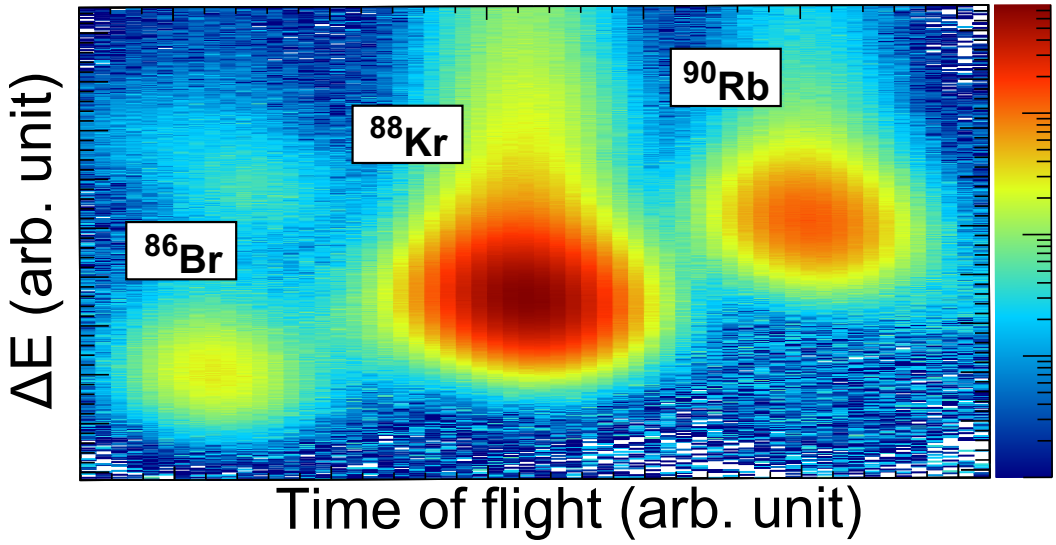

Figure A.3: Particle identification plot for the setting centered on $^{88}Kr^{35+}$ in the focal plane. The beam components are cleanly separated and identifiable.

projectile Coulomb excitation. Projectile identification and trajectory reconstruction were accomplished using the focal plane detectors of the S800 [32]. Particle identification was accomplished using the standard $\Delta E - ToF$ technique. Trajectory reconstruction was particularly important to measure the scattering angle of the projectiles, which is necessary as noted above to ensure there is no nuclear contribution to measured cross sections. The S800 focal plane detectors are described in more detail in Section 2.2. The outgoing scattered particle identification plot for the ^{88}Kr secondary beam is shown in Fig. A.3, where the energy loss is plotted versus the flight time from the *obj* scintillator. It was possible to select the ^{88}Kr outgoing projectiles separately from the other components of the cocktail beam, namely ^{86}Br and ^{90}Rb. The scattered ions assumed a charge-state distribution following passage through the bismuth target. In the case of the Kr isotopes, the H-like charge state was the most intense and was centered in the S800 focal plane, in contrast to ^{86}Se, in which case the fully-stripped charge state was strongest and centered in the spectrograph. The

typical S800 focal-plane rates were 1350 particles per second (pps) for $^{88}Kr^{35+}$, 350 pps for $^{90}Kr^{35+}$, and 20 pps for the fully stripped ^{86}Se particles, with incoming A1900 momentum acceptances of 0.5%, 1%, and 1%, respectively.

Refining the maximum scattering angle cut

The scattering angle was determined event-by-event using the position information in the focal plane of the S800 and an inverse map generated with COSY Infinity [35]. A significant, asymmetric angle emittance was observed in this experiment, and it was necessary to account for this in the determination of the maximum-scattering angle. For each isotope, the maximum scattering angle determined from the touching sphere + 2 fm minimum impact parameter served as a starting point. These initial maximum scattering angles were $\theta_{\max} = 56, 53,$ and 45 mrad in the laboratory frame for ^{88}Kr, ^{90}Kr, and ^{86}Se, respectively.

We performed Monte Carlo simulation of the angular distribution for inelastic scattering by using the Alder-Winther [12] formalism to generate the input probability distribution over the range $0 \leq \theta \leq \theta_{\max}$ with the assumption of a sharp angle cutoff in a simplistic black-disk model; i.e., all events with angles beyond $\theta_{\max}$ are assumed to be absorbed. Figure A.4 shows the simulated angular distribution assuming either no angular emittance (red curve) or the experimental angle emittance and straggling determined with LISE [61] from at-most elastically-scattered projectiles passing through the target. Close to the initial maximum-scattering-angle cutoff, it is clear that one loses a fraction of counts corresponding to the difference between the red and blue curves.

Comparing the simulated results with the experimental data (black histogram), which was restricted to events in which only a $2_1^+ \rightarrow 0_1^+$ decay was observed, the simulation including the realistic beam emittance and straggling shows good agreement. To avoid

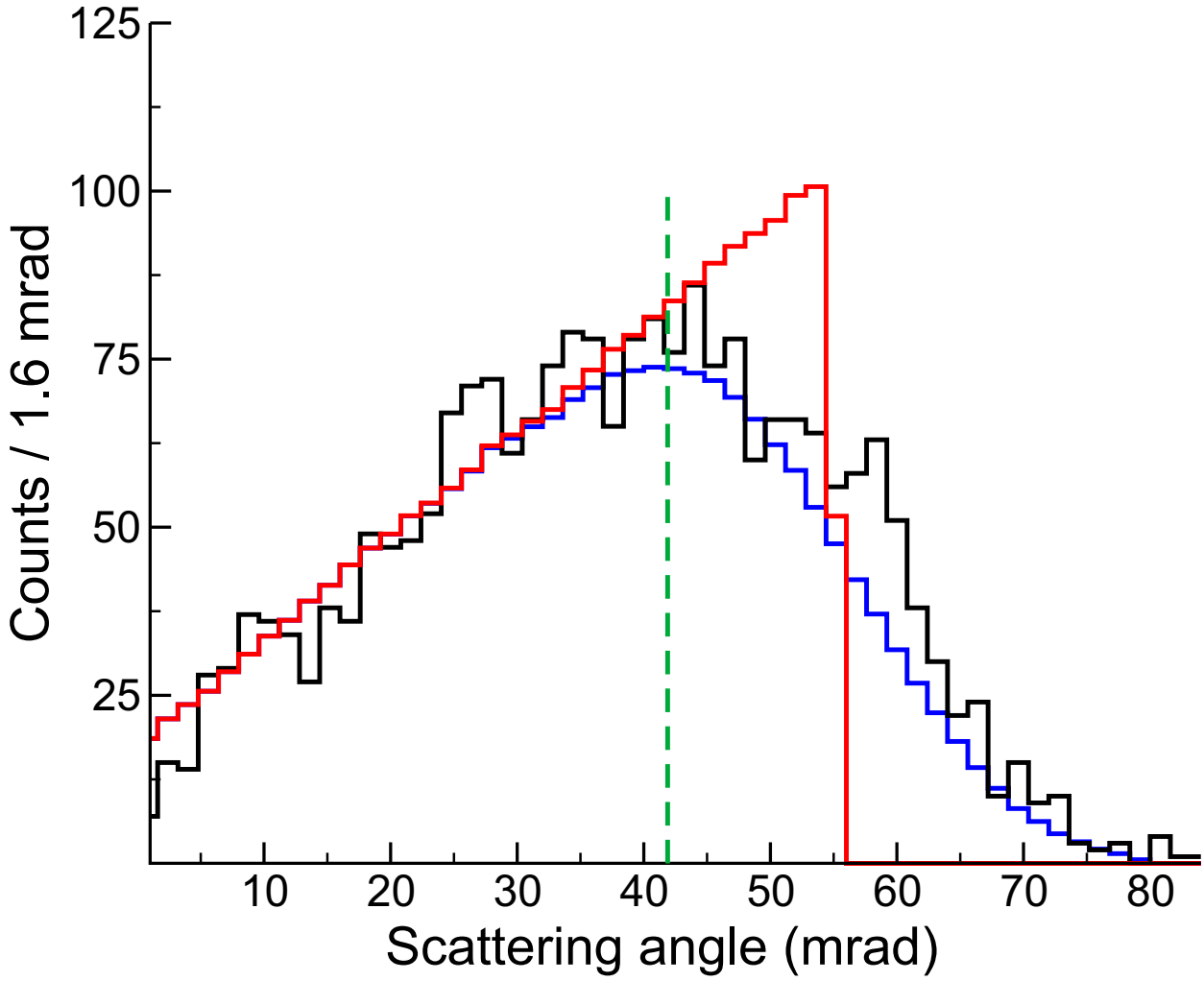

Figure A.4: Inelastic scattering distribution in the case of ^{88}Kr. The red and blue lines are Monte Carlo simulations of the inelastic scattering process based on an input probability distribution from the Alder-Winther relativistic Coulomb excitation model [12], either with (blue) or without (red) the effects of angle emittances and angular straggling. The dashed green line shows the chosen, more restrictive scattering-angle cut for the analysis of ^{88}Kr.

potentially underestimating the angle-integrated cross sections, and the resulting $B(E2)$ value, a more conservative maximum-scattering-angle cut, indicated by the dashed green line, was employed. This lead to maximum-scattering angles of 42 mrad, 35 mrad, and 30 mrad in the laboratory frame for ^{88}Kr, ^{90}Kr, and ^{86}Se, respectively. This was similar to a previous analysis [62], where it was shown that, away from the maximum-scattering angle

corresponding to impact parameters where flux was removed from the (in)elastic channel, the effect of angle emittance and straggling was minor due to an approximate balance of events that scattered into and out of the angle cut applied to the data.

CAESAR: the CsI(Na) scintillator array

Surrounding the ^{209}Bi target was CAESAR [63], the high-efficiency CsI(Na) scintillator array. CAESAR is composed of 192 closely packed scintillation crystals that cover almost 4π in a cube-like geometry. Because of its high granularity, the array allowed for an event-by-event Doppler reconstruction of the γ rays emitted in flight by the scattered projectiles. The γ ray emission angle for the Doppler reconstruction is deduced using the position of the CsI(Na) crystal that registered the largest energy deposition.

Compared to GRETINA, which is discussed in Section 2.3, CAESAR has a much higher in-beam detection efficiency, exceeding 35%, at the cost of a considerably worse energy resolution of approximately 10% FWHM for 1 MeV γ rays emitted in flight at $v/c = 40\%$ [63]. The corrections utilizing the inverse map beyond the ϕ correction described in Section 3.2 were not utilized, as they would have a negligible effect due to the thickness of the target. The energy-dependent photopeak efficiency of the setup was determined using ^{88}Y, ^{22}Na, ^{60}Co, and ^{137}Cs standard calibration sources. A GEANT4 simulation was used to model the in-beam response of the array, including the Lorentz boost of the emitted γ-ray distribution. The GEANT4 efficiency curve was scaled to the measured efficiencies. Taking into account the uncertainties in the activity of each sources, an overall efficiency uncertainty of 5.4% was determined.

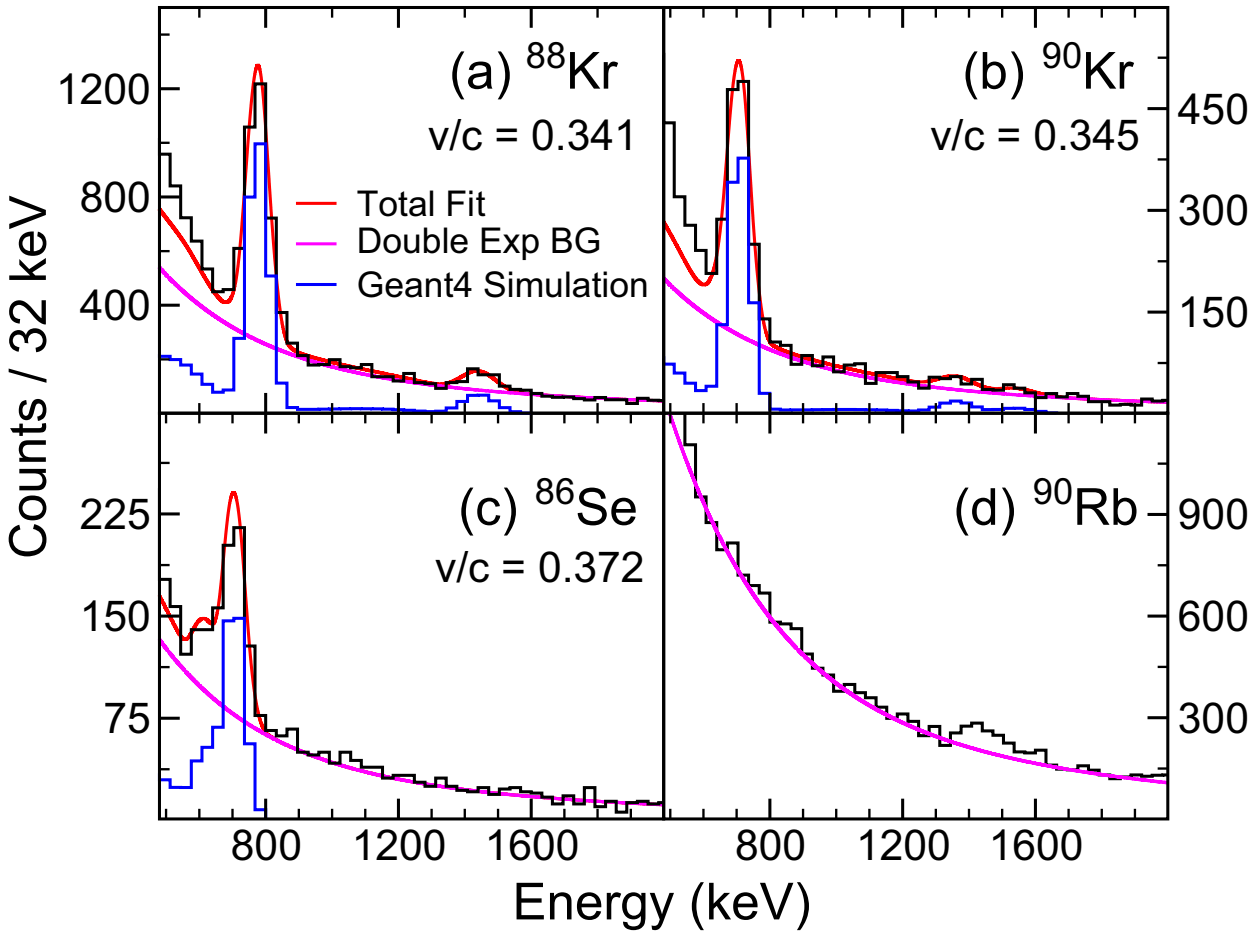

Figure A.5: (a)-(c) Doppler corrected γ-ray spectra including the fits to extract the angle-integrated Coulomb excitation cross sections for each isotope. The fit template based on the GEANT4 simulations is described in the text. (d) The spectrum of the beam contaminant ^{90}Rb with a double exponential fit to model the prompt, beam-correlated background, using an exclusion region in the fit around the peaks near 500 and 1400 keV. The resulting double exponential adequately reproduces the behavior in the region of interest, which is from 600 keV to 1.7 MeV.

The Doppler-corrected γ-ray spectra observed with CAESAR are presented in Fig. A.5. The final results for the measured angle-integrated Coulomb excitation cross sections and $B(E2)$ strengths for all isotopes and transitions observed in this work are presented in Table A.1. In the following sections, the results are discussed isotope-by-isotope, including

the observed level schemes and assumptions that underlie the fitting process.

Table A.1: Measured cross sections, σ, and transition strengths, $B(E2)$, for all isotopes studied in this work, as well as transition strengths from the shell-model calculation described in Section IV are shown. The uncertainty includes both statistical uncertainties and systematic contributions from varying the background model, as well as a 5.4% uncertainty from the efficiency determination.

				$B(E2; J_i \rightarrow J_f)$ $(e^2\text{fm}^4)$	
^{A}Z	J_i	J_f	σ (mb)	measured	shell model
^{88}Kr	0_1^+	2_1^+	210(30)	1310(190)	1450
	0_1^+	2_2^+	14(3)	90(20)	80
	2_2^+	2_1^+	-	$\leq$ 2010(450)	440
	0_1^+	2_3^+	50(8)	320(50)	450
	2_3^+	2_1^+	-	$\leq$ 71 [1]	69
	0_1^+	(2_4^+)	11(3)	70(20)	170
^{90}Kr	0_1^+	2_1^+	180(30)	1500(230)	1740
	0_1^+	2_2^+	40(10)	330(90)	580
	2_2^+	2_1^+	-	360(110)	280
	0_1^+	(2_3^+)	17(13)	150(110)	230
^{86}Se	0_1^+	2_1^+	230(30)	2110(320) [2]	1910
	0_1^+	2_2^+	-	-	150
	0_1^+	2_3^+	-	-	340

^{88}Kr

The primary fit template for ^{88}Kr was composed of two simulated peak responses: the 775 keV transition from the 2_1^+ state to the ground state and the 1440-keV transition from the 2_3^+ level at 2216 keV to the 2_1^+ one, both of which are visible in Fig. A.5(a). Two more feeding transitions were observed in the spectrum coincident with the $2_1^+ \rightarrow 0_1^+$ decay shown in Fig. A.6: one at 802 keV and another at 1644 keV. The relevant level scheme for transitions observed in coincidence with the detection of scattered ^{88}Kr projectiles is shown in Fig. A.7.

In Fig. A.6, the spectrum of γ rays detected in coincidence with the 775-keV transitions are shown with a "multiplicity-2" condition applied; i.e., exactly two of the 192 CAESAR

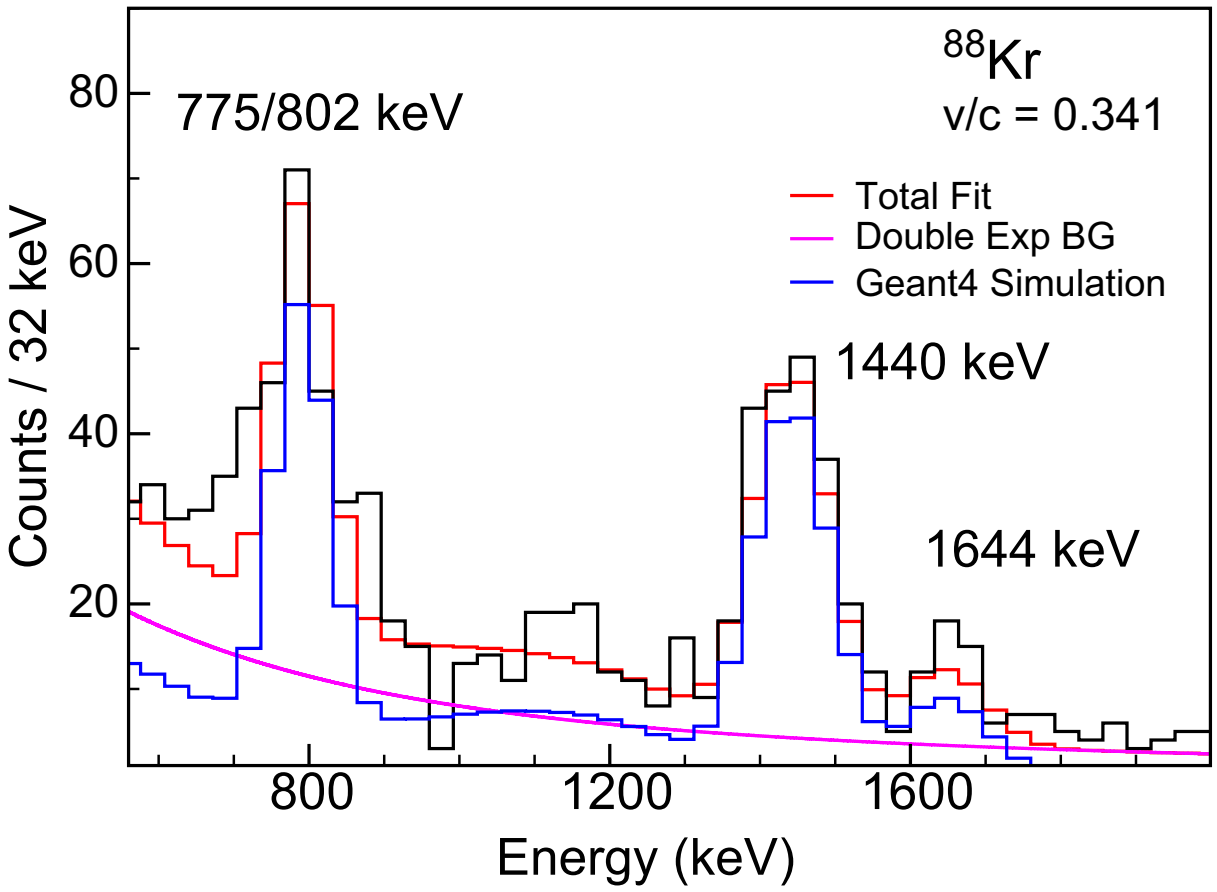

Figure A.6: Spectrum coincident with the observation of the self-coincident 775 keV-802 keV doublet of γ rays, including a fit to extract the intensity of the feeders. A detector multiplicity-2 condition is applied as explained in the text.

detectors registered an event within a prompt time gate, with one of these being the aforementioned 775-keV transition. Using this multiplicity condition, we selective reduce the beam-correlated background. Adding events with higher detector multiplicities primarily adds background to the coincidence matrix. It is clear that there is a self-coincident doublet composed of the 775-keV, $2_1^+ \rightarrow 0_1^+$ and 802-keV, $2_2^+ \rightarrow 2_1^+$ transitions. Due to the modest energy resolution of CAESAR, it was not possible to observe the 802-keV decay from the 1577-keV, 2_2^+ level in the γ singles spectrum. Furthermore, there is a γ ray at 1644 keV, which is consistent with a decay from the the 2419-keV, (3_1^-) level known in the literature [11]. It

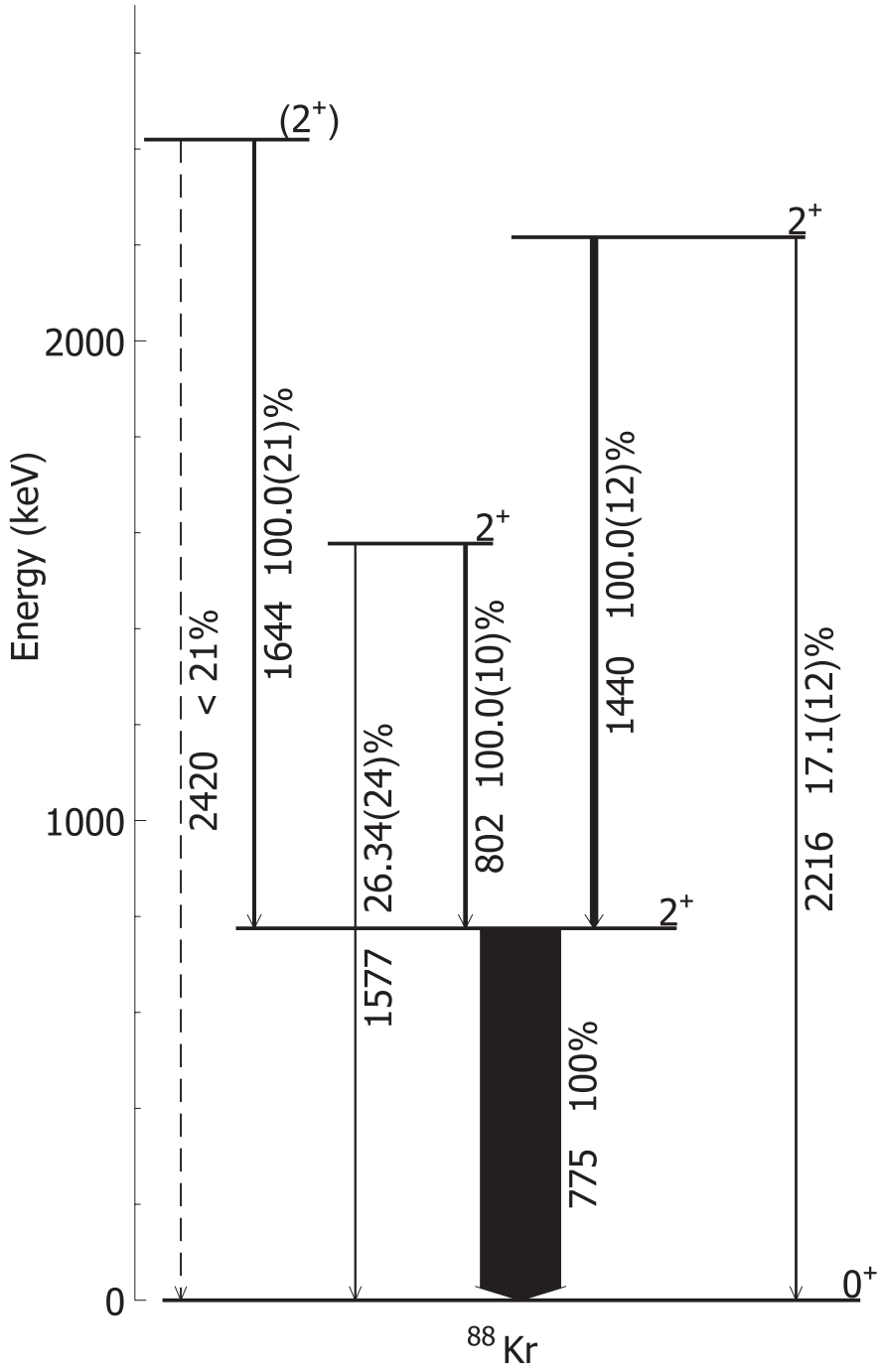

Figure A.7: Level scheme for transitions observed in coincidence with scattered ^{88}Kr projectiles. The given branching ratios are the adopted values from the NNDC database [11]. The dashed line giving an upper limit for the $(2_4^+) \rightarrow 0_1^+$ branching ratio is based on the present work.

was not possible to observe this transition in γ singles due to insufficient statistics.

Because the $2_2^+ \rightarrow 2_1^+$ transition was observed, one expects the 1577-keV, $2_2^+ \rightarrow 0_1^+$ decay to be present with a 26.34(24)% branching ratio [11]. This line is not visible in Fig. A.5(a) as it is below the sensitivity limit of the spectrum, but we use the known branching ratio quoted above to determine the cross section $\sigma(0_1^+ \rightarrow 2_2^+)$ based on the observed intensity of the 802-keV γ ray. Both the 802-keV and 1644-keV transition intensities were extracted from the fit in Fig. A.6. Because the 775-keV and 802-keV peaks form a doublet within our resolution, both were included in this fit with the constraint that each would occur with equal intensity, as every 802-keV transition in multiplicity 2 is necessarily in coincidence with a 775-keV transition. These intensities, along with the intensity of the 1440.5-keV γ ray were subtracted from the measured intensity of the 775-keV line. In this subtraction, the 802-keV transition had to be accounted for twice: as it is included in the peak area of the 775-keV transition, and it is indistinguishable in the fit of Fig. A.5. The ratio of the feeding-transition intensities to the total measured 775-keV one was determined to be 25(4)%.

The measured cross sections and deduced transition strengths for the transitions in ^{88}Kr are summarized in Table A.1. We note that a sub-barrier Coulomb excitation measurement reported in conference proceedings [65] and a thesis [66] proposed a $B(E2; 0_1^+ \rightarrow 2_1^+) = 900(90)\ e^2fm^4$, which is approximately 2σ lower than our measured value.

Using the $B(E2; 0_1^+ \rightarrow 2_2^+)$ value measured here for the first time and the known branching ratio, we could extract the transition strength to the 2_1^+ state as $B(E2; 2_2^+ \rightarrow 2_1^+) = \frac{\delta^2}{1+\delta^2}\ 2010(450)\ e^2fm^4$, where δ is the unknown $E2/M1$ multipole mixing ratio. Table A.1 quotes the upper limit of the strength as $B(E2) = 2010(450)\ e^2fm^4$.

Only the strong $2_3^+ \rightarrow 2_1^+$ branch was observed from the 2_3^+ level. The Coulomb excitation cross section, $\sigma 0_1^+ \rightarrow 2_3^+$ was deduced using the known branching ratio of 17.1(12)% [11]

relative to the $2_3^+ \rightarrow 2_1^+$ transition. The resulting absolute measurement of $B(E2; 0_1^+ \rightarrow 2_3^+) = 320(50)\ e^2fm^4$ is consistent with the rather uncertain previous measurement of $B(E2; 0_1^+ \rightarrow 2_3^+) = 400(200)\ e^2fm^4$ from relativistic Coulomb excitation, which is quoted in Ref. [64] relative to the excitation of the first 2_s^+tate using the earlier-mentioned result published solely in proceedings [65]. The $E2/M1$ multipole mixing ratio $\delta = 0.08^{+0.09}_{-0.05}$ [64] and the known branching ratio [11], we determined $B(M1; 2_3^+ \rightarrow 2_1^+) = 0.46(8)\mu_N^2$ and $B(E2; 2_3^+ \rightarrow 2_1^+ \leq 71\ e^2fm^4$.

If the 2419-keV level has spin-parity 3^- as suggested tentatively in the literature [11], the measured intensity of the $(3^-) \rightarrow 2_1^+$ γ ray would require an unphysically large excitation strength of $B(E3; 0_1^+ \rightarrow (3^-)) > 204600\ e^3fm^6$, corresponding to $B(E3\downarrow) > 63\ W.u.$ for the de-excitation. Therefore we tentatively assign $J^\pi = (2^+)$ for this state instead. No previously observed ground state transition from this 2419-keV level has been observed, and it was not observed in this experiment either, but we assign an upper limit on the branching ratio of 21% based on the experimental sensitivity at this energy in the spectrum. In the calculation of the cross section and the $B(E2; 0_1^+ \rightarrow (2^+))$ in Table A.1, a branching ratio of 10.5(105)%– exhausting the upper limit of the branching ratio–was used.

In addition to statistical and efficiency uncertainty, the quoted transition strengths and cross sections involved uncertainties from each measured peak intensity, which were determined by systematically varying the fit template and background model and determining the effect on the extracted peak area. The determined systematic uncertainty for the 775, 802, 1440, and 1644-keV transitions were 8%, 7.7%, 12%, and 9.1%, respectively. The error quoted for the extracted values for the 775-keV decay of course include the error propagated through the feeding subtraction.

^{90}Kr

For ^{90}Kr, the fit template used in Fig. A.5(b) included the four transitions represented by solid black arrows in Fig. A.8. The 655-keV, $2_2^+ \rightarrow 2_1^+$ transition was included despite forming a doublet with the 707-keV, $2_1^+ \rightarrow 0_1^+$ one by constraining its intensity through the known branching ratio of 68(4)% [11]. All observed transitions in Fig. A.8 have been reported in the literature at energies of 707.05(6), 655.17(6), 1362.32(10), and 1542.20(13) keV [11], except for the 2249-keV ground state transition, which must exist due to the population of 2249-keV level in this experiment.

In determining the $\sigma(0_1^+ \rightarrow 2_1^+)$ cross section, it is necessary to subtract the feeding intensities of the $2_2^+ \rightarrow 2_1^+$ and $(2^+) \rightarrow 2_1^+$ γ rays. This amounted to subtracting a total of 11(5)% from the measured intensity of the 707-keV transition. The extracted value of $B(E2; 0_1^+ \rightarrow 2_1^+) = 1500(230)$ is consistent with the only previously measured value [67], but with greatly reduced uncertainties. Using the known $E2/M1$ mixing ratio $\delta = 0.507^{+0.020}_{-0.022}$ [68], the $B(E2; 2_2^+ \rightarrow 2_1^+)$ strength quoted in Table A.1 was determined, in addition to the $B(E2; 2_1^+ \rightarrow 0_1^+)$.

Although the level at 2249 keV has no J^π assignment in the literature, we argue that this is a higher-lying 2^+ state based on its population in this experiment, similar to the argument made for the 2420-keV level in ^{88}Kr discussed in the previous section. An upper limit of 23% for the ground-state decay branch was determined based on the sensitivity limit posed by our spectrum. To determine the $B(E2; 0_1^+ \rightarrow (2^+))$ value shown in Table A.1, a branching ratio of 11.5(115)% was assumed, encompassing the upper limit.

The final determined uncertainties followed a similar process to ^{88}Kr. By systematically varying the fit template and background model, systematic uncertainties of 30.4%, 10.4%,

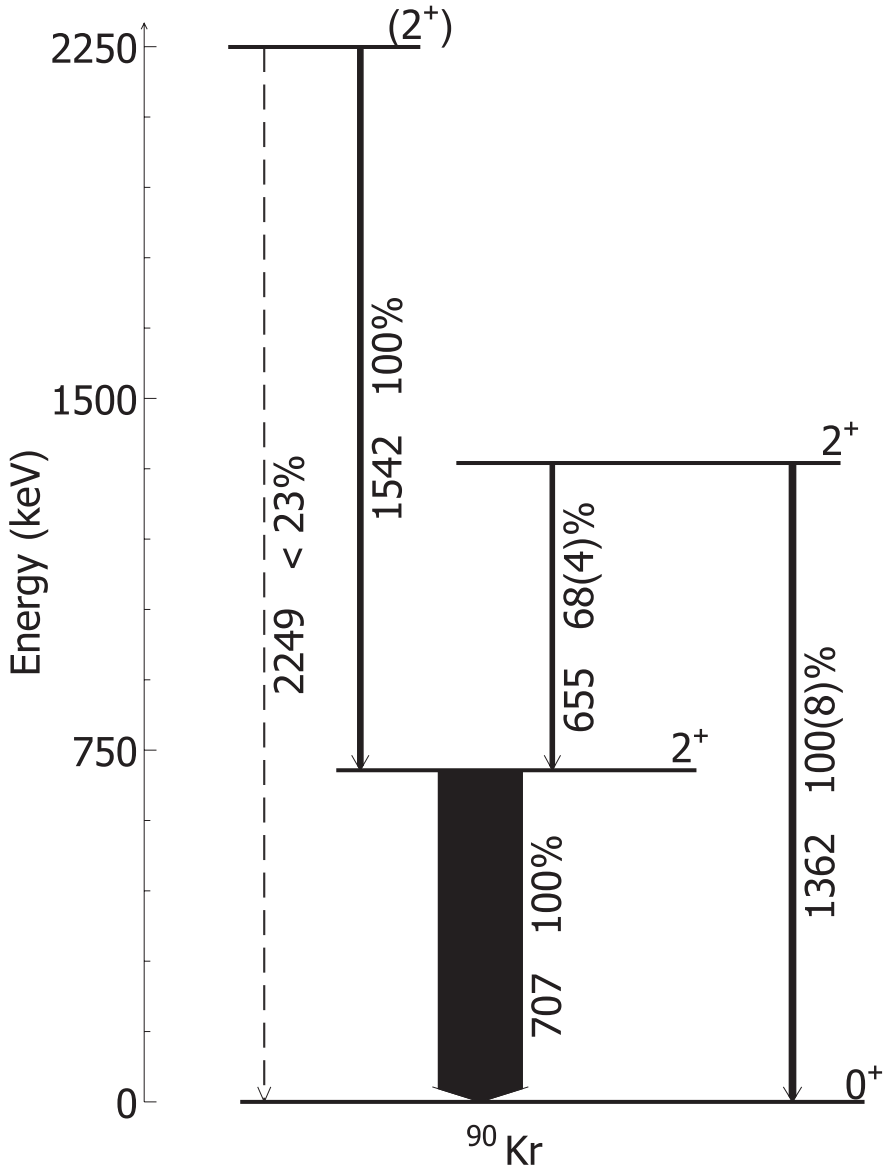

Figure A.8: Level scheme for transitions observed in coincidence with scattered ^{90}Kr projectiles. The given branching ratios are the adopted values from the NNDC database [11]. The dashed line giving an upper limit for the $(2^+) \rightarrow 0_1^+$ branching ratio is based on the sensitivity limit at this energy in the present work.

and 62% were determined for the 655-, 707-, and 1542-keV peak intensities, respectively. The final quoted errors includes these as well as statistical and efficiency uncertainties, and are propagated through the feeding subtraction for the $B(E2; 0_1^+ \rightarrow 2_1^+)$ value.

^{86}Se

The fit template for ^{86}Se was considerably simpler than the krypton isotopes, as only the expected $2_1^+ \rightarrow 0_1^+$ decay was observed in Fig. A.5(c). There was, however, a low-energy shoulder that may correspond to a peak near 613 keV. This transition energy has been reported previously [69], and was tentatively suggested to directly feed the 2_1^+ state. This would lead to a low-lying second-excited state of unknown nature. No coincidence relationship was observed between the 613- and 704-keV γ rays in this work, and this tentative 613-keV decay is considered unplaced in the evaluated data [11]. To gauge the effect of including this low-energy shoulder as peak, two fitting templates were used: one that includes a 613-keV peak and one that does not. Figure A.5(c) shows the result of including this 613-keV peak. Removing it significantly worsens the χ^2 of the fit, but only increases the cross section and $B(E2; 0_1^+ \rightarrow 2_1^+)$ value from 227(34) mb and 2110(320) e^2fm^4 to 233(35) mb and 2170(330) e^2fm^4. In Table A.1, the first set of values is quoted.

The measured $B(E2) = 2110(320)\ e^2fm^4$ agrees at considerably reduced uncertainty with the literature value from the excited-state lifetime measurement [10] of $B(E2) = 2190^{+1295}_{-855} e^2fm^4$. The quoted uncertainty for our measured $B(E2)$ value includes a systematic uncertainty of 12.4% determined by varying the fit template and background model, which was then added in quadrature to the efficiency and statistical uncertainties.

Discussion

The final results for the evolution of collectivity along the selenium and krypton isotopic chains, including the newly measured values discussed in the previous sections, are shown in Fig. A.9. The newly measured values are consistent with the picture of a gradual onset

of deformation beyond $N = 50$ for $Z = 34, 36$. For ^{88}Kr, the result shows the expected behavior of a slight increase in collectivity relative to the singly-magic ^{86}Kr, in contrast with the previously adopted value [65, 66] with which it differs by more than 1σ. This increase in collectivity is expected for even-even neighbors of singly-magic nuclei along an isotopic chain. In the case of ^{90}Kr and ^{86}Se, the newly measured values are consistent with previous measurements [10, 67], but with greatly increased precision. With these new more precise values, the evolution of B(E2) strength is now clearly consistent with the predicted smooth onset of deformation [70, 71].

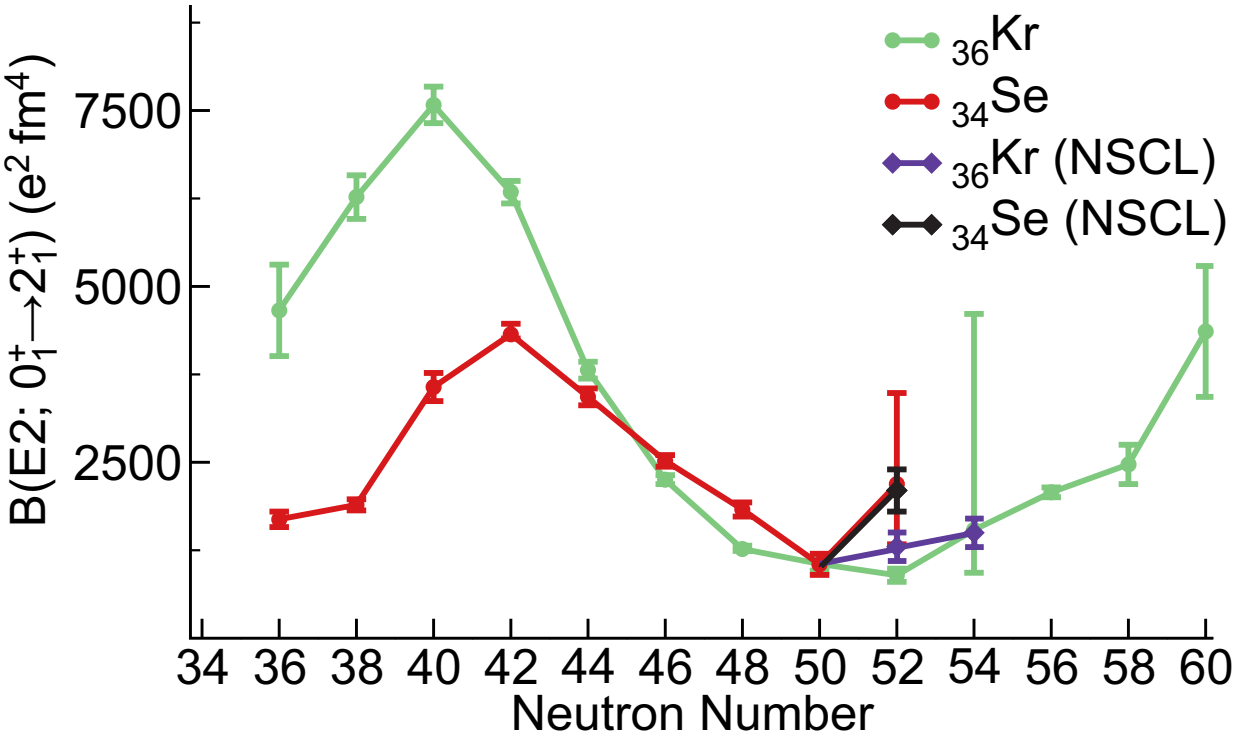

Figure A.9: Evolution of collectivity from $N = 36$ to $N = 60$ for the krypton and selenium isotopes, including adopted values and the values measured here. The adopted values are taken from Ref. [8], except for the case of ^{86}Se [10]. Note the different units used here compared to Fig. A.1 (see Sec. A).

One unique result of this experiment was the observation of several higher-lying 2^+ states for the krypton isotopes, signaling significant excitation strength. To understand

these $E2$ strength distributions, we compare to large-scale shell-model calculation using the code NUSHELLX@MSU [72] with an effective two-body interaction derived from the Idaho N^3LO nucleon-nucleon interaction [73]. The effective interaction was obtained using many-body perturbation theory to third order in the interaction following the recipe outlined in Refs. [62, 74]. A ^{78}Ni core was used with single-particle energies taken from either Ref. [75] or determined using Skyrme-Hartree-Fock calculations where missing. The model space included the proton $1f_{5/2}, 2p_{3/2}, 2p_{1/2}, 1g_{9/2}$ orbitals and the neutron $1g_{7/2}, 2d_{5/2}, 2d_{3/2}, 3s_{1/2}, 1h_{11/2}$ orbitals, without sub-shell restrictions and with the energy of the $\pi g_{9/2}$ adjusted to reproduce the $9/2^+$ state in ^{87}Rb. The software used to derive the effective Hamiltonian, and the resulting effective interaction and single-particle energies used in the shell-model calculations are available on GitHub [76].

It was necessary to adjust the effective charges that enter the calculation of $B(E2)$ values in the shell model calculation. To accomplish this, the transition strengths of ^{86}Kr were calculated in our shell-model setup, and the proton effective charge was adjusted to $e_p = 1.68$ to reproduce the known $B(E2; 0_1^+ \rightarrow 2_1^+) = 1056(95)e^2fm^4$ [77]. Assuming a simple picture of isoscalar polarization charges, where $e_p = 1 + \delta_{\rm pol}$ and $e_n = \delta_{\rm pol}$, the neutron effective charge is then $e_n = 0.68$. These choices of the effective charges are supported by the use of similar choices of effective charges in other calculations that utilize a similar model space for this region [78].

The results of the shell-model calculation for the krypton isotopes are shown both in Table A.1 and in Fig. A.10, where the calculated (red) and measured (black) $B(E2; 0_1^+ \rightarrow 2_n^+)$ are shown as a function of the excitation energy of the 2_n^+ state being considered. There is good agreement between the measured and calculated values for both the energies and transition strengths, which is somewhat remarkable considering the fact that only the single-

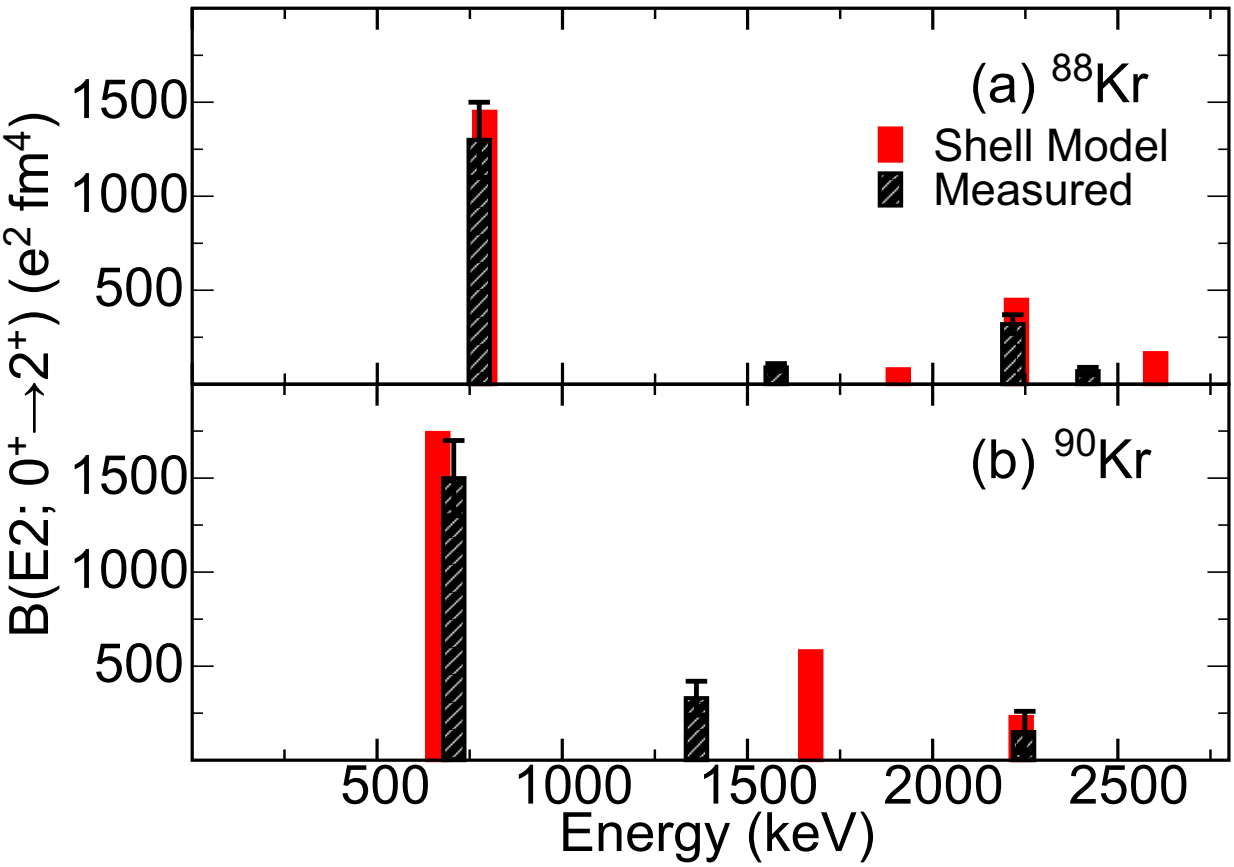

Figure A.10: Comparison between measured $B(E2)$ values and the results of a shell-model calculation for ^{88,90}Kr as a function of the energy of the 2_n^+ states.

particle energies involved in the shell-model calculation are tuned in any way. Furthermore, looking at Table A.1, the calculated $B(E2; 2_2^+ \rightarrow 2_1^+)$ for ^{90}Kr agrees with experiment. The comparison is more difficult for ^{88}Kr, as the $B(E2; 2_2^+ \rightarrow 2_1^+)$ reported in Table A.1 is only an upper limit due to the unknown $E2/M1$ multipole mixing ratio. Agreement would be exact assuming a multipole mixing ratio of $|\delta| = 0.53$, which is similar to the known mixing ratio of $\delta = 0.507^{+0.020}_{-0.022}$ for the corresponding transition in ^{90}Kr.

The 2_3^+ level of ^{88}Kr has been proposed by Ref. [64] as a candidate for a proton-neutron mixed symmetry state [79]. This is indicated by a collective $M1$ transition to the first 2^+ and a weakly collective $E2$ decay to the ground state. Using the adopted branching ratio from the

NNDC database [11], and the $E2/M1$ multipole mixing ratio from Ref. [64], we determined $B(M1; 2_3^+ \rightarrow 2_1^+) = 0.46(8)\mu_N^2$ and $B(E2; 2_3^+ \rightarrow 0_1^+) = 64(10)\ e^2fm^4 \equiv 2.8(4)W.u.$. These values are consistent with the aforementioned expectations of a mixed symmetry state, and are in good agreement with the shell-model calculation results of $B(M1; 2_3^+ \rightarrow 2_1^+) = 0.51\mu_N^2$ and $B(E2; 2_3^+ \rightarrow 0_1^+) = 90\ e^2fm^4$.

To quantify the amount of expected higher-lying strength in ^{86}Se, which we did not observe experimentally, we used the shell-model calculation and determined the peak areas expected based on the calculated $B(E2; 0_1^+ \rightarrow 2_n^+)$ for the tentatively assigned 1399-keV, (2_2^+) and 2208-keV, (2_3^+) levels from the literature [11]. We utilized the adopted branching ratios from the NNDC database. Based on the calculated transition strengths, we'd expect 6(2) and 22(5) counts to be observed for the 1399-keV, $(2_2^+) \rightarrow 0_1^+$ and 695-keV, $(2_2^+) \rightarrow 2_1^+$ decays. In terms of the 2208-keV state, we'd expect to observe 43(11) counts at 1504 keV for the $(2_3^+) \rightarrow 2_1^+$ transition and less than 2 counts at 2208-keV for the 2208-keV, $(2_3^+) \rightarrow 0_1^+$ one. Because all of these expected peak areas are below the sensitivity limit of the measurement, the observed ^{86}Se data is consistent with the predicted $E2$ strength in the shell-model calculations. Assuming the intensities deduced from the calculated shell-model strength and branching ratios, the quoted $B(E2; 0_1^+ \rightarrow 2_1^+)$ in Table A.1 would be reduced by 23%. Because we do not observe these transitions, this value serves as an upper limit on the feeding from known states.

Presented in Table A.2 are the proton and neutron orbital occupancies from the shell-model calculation described above. Note that these are consistent with those from another shell-model calculation for ^{90}Kr [68] in terms of the proton occupations. For the neutron occupations, there is a slight difference as the $g_{7/2}$ and $h_{11/2}$ orbitals have essentially 0 occupancy here, while in Ref. [68] they are substantial at 0.15 and 0.18, respectively, for the

Table A.2: Shell-model occupations of the proton and neutron orbitals for the observed levels in ^{88,90}Kr and ^{86}Se.

		Protons				Neutrons				
		$f_{5/2}$	$p_{3/2}$	$p_{1/2}$	$g_{9/2}$	$g_{7/2}$	$d_{5/2}$	$d_{3/2}$	$s_{1/2}$	$h_{11/2}$
^{88}Kr	0^+_1	4.29	2.74	0.62	0.35	0.01	1.88	0.04	0.06	0.02
	2^+_1	4.29	2.74	0.65	0.33	0.00	1.88	0.03	0.08	0.01
	2^+_2	4.21	2.84	0.72	0.23	0.00	1.83	0.03	0.12	0.01
	2^+_3	4.28	2.69	0.79	0.24	0.00	1.86	0.05	0.08	0.01
	2^+_4	4.60	2.64	0.55	0.21	0.01	1.84	0.04	0.09	0.02
^{90}Kr	0^+_1	3.96	2.96	0.79	0.29	0.01	3.68	0.16	0.13	0.03
	2^+_1	3.93	2.99	0.80	0.27	0.01	3.66	0.14	0.18	0.02
	2^+_2	3.85	2.80	1.15	0.20	0.01	3.57	0.19	0.21	0.02
	2^+_3	3.81	3.10	0.87	0.22	0.01	3.57	0.11	0.29	0.02
^{86}Se	0^+_1	3.50	1.84	0.41	0.24	0.01	1.80	0.06	0.12	0.01
	2^+_1	3.55	1.82	0.41	0.21	0.01	1.76	0.05	0.17	0.01

ground state of ^{90}Kr.

Summary

We were able to determine the electric quadrupole transition strengths for ^{88,90}Kr and ^{86}Se with considerably increased precision compared to previous measurements. Furthermore, we provide measurements of the strength to higher-lying 2^+ states for the krypton isotopes, in most cases for the first time. This fragmentation of strength to higher-lying states is remarkably consistent with the results of large-scale shell-model calculations with a minimally-tuned single-particle basis and an effective interaction based on chiral effective field theory. In closing, our results definitively complete the picture of a gradual onset of collectivity for the neutron-rich krypton isotopes beyond $N = 50$, and provide a good starting point for future explorations beyond $N = 52$ for the selenium isotopic chain.

Recently, the measured $B(E2; 2^+_1 \rightarrow 0^+_1)$ from the measurement presented in this work

were confirmed, albeit with larger uncertainties, in a recoil-distance Doppler shift measurement [80], which determines the $B(E2)$ values by measuring the lifetimes of the corresponding states.

For the krypton isotopic chain,the first spectroscopy [71] of ^{98,100}Kr using (p, 2p) from ^{99,101}Rb, respectively, was performed at the Radioactive Isotope Beam Factory (RIBF) at the RIKEN Nishina Center. A picture of shape coexistence emerges in ^{98}Kr, where a low lying $(0_2^+,2_2^+)$ state was reported.

In another experiment [54] utilizing nucleon removal reactions at RIBF, low-lying excited states in ^{88,90,92,94}Se were populated. The observed trend of the gradually-decreasing $E(2_1^+)$ energies along the isotopic chain presents a picture of gradually increasing collectivity when approaching $N = 60$ for the selenium isotopes, a situation that is quite similar to that of the krypton isotopic chain.

Future measurements utilizing intermediate-energy Coulomb excitation to measure the $B(E2)$ values of these short-lived isotopes will play an important role in determining the evolution of collectivity at the extremes of neutron-proton asymmetry. The production of these nuclei approaching the limits of nuclear stability at RIBF, and the opportunity to produce these and even more exotic nuclei at FRIB with high-intensity beams, will enable such measurements to be performed, and greatly improve our knowledge of the properties of nuclei at the limits of existence.

APPENDIX B

EVENT-BY-EVENT CORRECTION FOR THE PARTICLE VELOCITY USING *DTA*

This appendix will provide a brief derivation of the correction for the particle velocity used for Doppler reconstruction using the *dta* value described in Chapter 2. The correction proceeds as follows. The *dta* value is $\frac{dT}{T}$, where $T = E - mc^2$ is the kinetic energy. Let $\beta = \frac{v}{c}$ and $\gamma = \frac{1}{1-\beta^2}$. The following equation makes use of the relation $E = \gamma mc^2$.

$$\frac{dT}{T} = \frac{d(E - mc^2)}{E - mc^2} \tag{B.1}$$

$$= \frac{dE}{mc^2(\gamma - 1)} \tag{B.2}$$

To determine dE, recall $E\beta = pc$ for momentum p, and consider:

$$d(E^2) = 2EdE = d((pc)^2 + (mc^2)^2) \tag{B.3}$$

$$= 2pc^2dp \tag{B.4}$$

$$dE = \frac{pc^2dp}{E} = \beta cdp \tag{B.5}$$

Now plugging dE into the expression for $\frac{dT}{T}$ and recalling the relations $(\gamma\beta)^2 = \gamma^2 - 1$, and $p = \gamma\beta mc$:

$$\frac{dT}{T} = \frac{\beta cdp}{mc^2(\gamma - 1)} \tag{B.6}$$

$$= \frac{(\gamma\beta)^2 cdp}{\gamma^2\beta mc^2(\gamma - 1)} \tag{B.7}$$

$$= \frac{(\gamma^2 - 1)cdp}{\gamma(\gamma\beta mc)c(\gamma - 1)} \tag{B.8}$$

$$= \frac{(\gamma + 1)(\gamma - 1)dp}{\gamma p(\gamma - 1)} \tag{B.9}$$

$$= \frac{\gamma + 1}{\gamma}\frac{dp}{p} \tag{B.10}$$

Now we want an expression connecting $\frac{dp}{p}$ and $\frac{d\beta}{\beta}$. Recall that $\frac{d\gamma}{d\beta} = \beta\gamma^3$, and again using $(\gamma\beta)^2 = \gamma^2 - 1$:

$$\frac{dp}{p} = \frac{d(\gamma\beta mc)}{\gamma\beta mc} \tag{B.11}$$

$$= \frac{1}{\gamma\beta mc}\left(\frac{d\gamma}{d\beta}\beta mc + \gamma mc\right) d\beta \tag{B.12}$$

$$= \frac{1}{\gamma\beta mc}\left(\beta^2\gamma^3 mc + \gamma mc\right) d\beta \tag{B.13}$$

$$= \frac{(\beta^2\gamma^2 + 1)d\beta}{\beta} \tag{B.14}$$

$$= \gamma^2\frac{d\beta}{\beta} \tag{B.15}$$

Finally, plugging this into the expression for $\frac{dT}{T}$:

$$\frac{dT}{T} = \frac{\gamma + 1}{\gamma}\gamma^2\frac{d\beta}{\beta} \tag{B.16}$$

$$= \gamma(\gamma + 1)\frac{d\beta}{\beta} \tag{B.17}$$

So, we correct the reconstruction velocity for each event by the determined $dta = \frac{dT}{T}$ with:

$$d\beta = \frac{dT}{T}\frac{\beta}{\gamma(\gamma + 1)} \tag{B.18}$$

BIBLIOGRAPHY

BIBLIOGRAPHY

[1] S. Suchyta, S. N. Liddick, Y. Tsunoda, T. Otsuka, M. B. Bennett, A. Chemey, M. Honma, N. Larson, C. J. Prokop, S. J. Quinn, N. Shimizu, A. Simon, A. Spyrou, V. Tripathi, Y. Utsuno, and J. M. VonMoss, Phys. Rev. C **89**, 021301 (2014).

[2] T. Otsuka, "Type I and II shell evolutions in exotic nuclei," (2014), FUSTIPEN Topical Meeting.

[3] C. J. Chiara, D. Weisshaar, R. V. F. Janssens, Y. Tsunoda, T. Otsuka, J. L. Harker, W. B. Walters, F. Recchia, M. Albers, M. Alcorta, V. M. Bader, T. Baugher, D. Bazin, J. S. Berryman, P. F. Bertone, *et al.*, Phys. Rev. C **91**, 044309 (2015).

[4] T. Otsuka, Nuclear Physics A **693**, 383 (2001).

[5] B. Cheal, E. Mané, J. Billowes, M. L. Bissell, K. Blaum, B. A. Brown, F. C. Charlwood, K. T. Flanagan, D. H. Forest, C. Geppert, M. Honma, A. Jokinen, M. Kowalska, A. Krieger, J. Krämer, *et al.*, Phys. Rev. Lett. **104**, 252502 (2010).

[6] A. F. Lisetskiy, B. A. Brown, M. Horoi, and H. Grawe, Phys. Rev. C **70**, 044314 (2004).

[7] M. Honma, T. Otsuka, T. Mizusaki, and M. Hjorth-Jensen, Phys. Rev. C **80**, 064323 (2009).

[8] B. Pritychenko, M. Birch, B. Singh, and M. Horoi, Atomic Data and Nuclear Data Tables **107**, 1 (2016).

[9] W. Witt, V. Werner, N. Pietralla, M. Albers, A. D. Ayangeakaa, B. Bucher, M. P. Carpenter, D. Cline, H. M. David, A. Hayes, C. Hoffman, R. V. F. Janssens, B. P. Kay, F. G. Kondev, W. Korten, *et al.*, Phys. Rev. C **98**, 041302 (2018).

[10] J. Litzinger, A. Blazhev, A. Dewald, F. Didierjean, G. Duchêne, C. Fransen, R. Lozeva, K. Sieja, D. Verney, G. de Angelis, *et al.*, Phys. Rev. C **92**, 064322 (2015).

[11] "Evaluated nuclear structure data file (ensdf)," https://www.nndc.bnl.gov/ensdf/ .

[12] A. Winther and K. Alder, Nucl. Phys. A **319**, 518 (1979).

[13] B. A. Brown, Lecture notes in nuclear structure physics .

[14] K. Heyde and J. L. Wood, Rev. Mod. Phys. **83**, 1467 (2011).

[15] T. Otsuka, T. Suzuki, R. Fujimoto, H. Grawe, and Y. Akaishi, Phys. Rev. Lett. **95**, 232502 (2005).

[16] Y. Tsunoda, T. Otsuka, N. Shimizu, M. Honma, and Y. Utsuno, Phys. Rev. C **89**, 031301 (2014).

[17] B. Crider, C. Prokop, S. Liddick, M. Al-Shudifat, A. Ayangeakaa, M. Carpenter, J. Carroll, J. Chen, C. Chiara, H. David, A. Dombos, S. Go, R. Grzywacz, J. Harker, R. Janssens, *et al.*, Phys. Lett. B **763**, 108 (2016).

[18] C. J. Prokop, B. P. Crider, S. N. Liddick, A. D. Ayangeakaa, M. P. Carpenter, J. J. Carroll, J. Chen, C. J. Chiara, H. M. David, A. C. Dombos, S. Go, J. Harker, R. V. F. Janssens, N. Larson, T. Lauritsen, *et al.*, Phys. Rev. C **92**, 061302 (2015).

[19] S. Leoni, B. Fornal, N. Mărginean, M. Sferrazza, Y. Tsunoda, T. Otsuka, G. Bocchi, F. C. L. Crespi, A. Bracco, S. Aydin, M. Boromiza, D. Bucurescu, N. Cieplicka-Oryńczak, C. Costache, S. Călinescu, *et al.*, Phys. Rev. Lett. **118**, 162502 (2017).

[20] F. Nowacki, A. Poves, E. Caurier, and B. Bounthong, Phys. Rev. Lett. **117**, 272501 (2016).

[21] R. Taniuchi, C. Santamaria, P. Doornenbal, A. Obertelli, K.-i. Yoneda, G. Authelet, H. Baba, D. Calvet, F. Château, A. Corsi, A. Delbart, J.-M. Gheller, A. Gillibert, J. D Holt, T. Isobe, *et al.*, Nature **569**, 53 (2019).

[22] E. K. Warburton, J. A. Becker, and B. A. Brown, Phys. Rev. C **41**, 1147 (1990).

[23] K. Wimmer, T. Kröll, R. Krücken, V. Bildstein, R. Gernhäuser, B. Bastin, N. Bree, J. Diriken, P. Van Duppen, M. Huyse, N. Patronis, P. Vermaelen, D. Voulot, J. Van de Walle, F. Wenander, *et al.*, Phys. Rev. Lett. **105**, 252501 (2010).

[24] A. Gade, R. V. F. Janssens, D. Bazin, R. Broda, B. A. Brown, C. M. Campbell, M. P. Carpenter, J. M. Cook, A. N. Deacon, D.-C. Dinca, B. Fornal, S. J. Freeman, T. Glasmacher, P. G. Hansen, B. P. Kay, *et al.*, Phys. Rev. C **74**, 021302 (2006).

[25] P. Hansen and J. Tostevin, Annu. Rev. Nucl. Part. Sci. **53**, 219 (2003).

[26] F. Recchia, D. Weisshaar, A. Gade, J. A. Tostevin, R. V. F. Janssens, M. Albers, V. M. Bader, T. Baugher, D. Bazin, J. S. Berryman, B. A. Brown, C. M. Campbell, M. P. Carpenter, J. Chen, C. J. Chiara, *et al.*, Phys. Rev. C **94**, 054324 (2016).

[27] A. Gade and B. M. Sherrill, Phys. Scr. **91**, 053003 (2016).

[28] G. Machicoane, D. Cole, J. Ottarson, J. Stetson, and P. Zavodszky, Review of Scientific Instruments **77**, 03A322 (2006).

[29] D. Morrissey, B. Sherrill, M. Steiner, A. Stolz, and I. Wiedenhoever, Nucl. Instrum. Methods Phys. Res. B **204**, 90 (2003).

[30] D. Bazin, J. Caggiano, B. Sherrill, J. Yurkon, and A. Zeller, Nucl. Instrum. Methods Phys. Res. B **204**, 629 (2003).

[31] J. A. Caggiano, Ph.D. thesis, Michigan State University (1999).

[32] J. Yurkon, D. Bazin, W. Benenson, D. Morrissey, B. Sherrill, D. Swan, and R. Swanson, Nucl. Instrum. Methods Phys. Res. A **422**, 291 (1999).

[33] K. Meierbachtol, D. Bazin, and D. Morrissey, Nucl. Instrum. Methods Phys. Res. A **652**, 668 (2011), Symposium on Radiation Measurements and Applications (SORMA) XII 2010.

[34] S. R. Stroberg, Ph.D. thesis, Michigan State University (2014).

[35] M. Berz, K. Joh, J. A. Nolen, B. M. Sherrill, and A. F. Zeller, Phys. Rev. C **47**, 537 (1993).

[36] K. Wimmer, D. Barofsky, D. Bazin, L. Fraile, J. Lloyd, J. Tompkins, and S. Williams, Nucl. Instrum. Methods Phys. Res. A **769**, 65 (2015).

[37] S. Paschalis, I. Lee, A. Macchiavelli, C. Campbell, M. Cromaz, S. Gros, J. Pavan, J. Qian, R. Clark, H. Crawford, D. Doering, P. Fallon, C. Lionberger, T. Loew, M. Petri, *et al.*, Nucl. Instrum. Methods Phys. Res. A **709**, 44 (2013).

[38] D. Weisshaar, D. Bazin, P. C. Bender, C. M. Campbell, F. Recchia, V. Bader, T. Baugher, J. Belarge, M. P. Carpenter, H. L. Crawford, M. Cromaz, B. Elman, P. Fallon, A. Forney, A. Gade, *et al.*, Nucl. Instrum. Methods Phys. Res. A **847**, 187 (2017).

[39] L. A. Riley, "UCGretina," (unpublished).

[40] P.-A. Söderström, F. Recchia, J. Nyberg, A. Al-Adili, A. Ataç, S. Aydin, D. Bazzacco, P. Bednarczyk, B. Birkenbach, D. Bortolato, A. Boston, H. Boston, B. Bruyneel, D. Bucurescu, E. Calore, *et al.*, Nucl. Instrum. Methods Phys. Res. A **638**, 96 (2011).

[41] I. Stefanescu, D. Pauwels, N. Bree, T. E. Cocolios, J. Diriken, S. Franchoo, M. Huyse, O. Ivanov, Y. Kudryavtsev, N. Patronis, J. V. D. Walle, P. V. Duppen, and W. B. Walters, Phys. Rev. C **79**, 044325 (2009).

[42] G. Mairle, G. Kaschl, H. Link, H. Mackh, U. Schmidt-Rohr, G. Wagner, and P. Turek, Nucl. Phys. A **134**, 180 (1969).

[43] W. F. Mueller, B. Bruyneel, S. Franchoo, M. Huyse, J. Kurpeta, K. Kruglov, Y. Kudryavtsev, N. V. S. V. Prasad, R. Raabe, I. Reusen, P. Van Duppen, J. Van Roosbroeck, L. Vermeeren, L. Weissman, Z. Janas, *et al.*, Phys. Rev. C **61**, 054308 (2000).

[44] H. Mach, M. Lewitowicz, M. Stanoiu, F. Becker, J. Blomqvist, M. Berge, R. Boutami, B. Cederwall, Z. Dlouhy, B. Fogelberg, L. Fraile, G. Georgiev, H. Grawe, R. Grzywacz, P. Johansson, *et al.*, Nucl. Phys. A **719**, C213 (2003).

[45] A. Morales, G. Benzoni, H. Watanabe, Y. Tsunoda, T. Otsuka, S. Nishimura, F. Browne, R. Daido, P. Doornenbal, Y. Fang, G. Lorusso, Z. Patel, S. Rice, L. Sinclair, P.-A. Söderström, *et al.*, Phys. Lett. B **765**, 328 (2017).

[46] C. J. Prokop, Ph.D. thesis, Michigan State University (2016).

[47] F. Flavigny, J. Elseviers, A. N. Andreyev, C. Bauer, V. Bildstein, A. Blazhev, B. A. Brown, H. De Witte, J. Diriken, V. N. Fedosseev, S. Franchoo, R. Gernhäuser, M. Huyse, S. Ilieva, S. Klupp, *et al.*, Phys. Rev. C **99**, 054332 (2019).

[48] B. Elman, A. Gade, D. Weisshaar, D. Barofsky, D. Bazin, P. C. Bender, M. Bowry, M. Hjorth-Jensen, K. W. Kemper, S. Lipschutz, E. Lunderberg, N. Sachmpazidi, N. Terpstra, W. B. Walters, A. Westerberg, *et al.*, Phys. Rev. C **96**, 044332 (2017).

[49] P. Campbell, H. L. Thayer, J. Billowes, P. Dendooven, K. T. Flanagan, D. H. Forest, J. A. R. Griffith, J. Huikari, A. Jokinen, R. Moore, *et al.*, Phys. Rev. Lett. **89**, 082501 (2002).

[50] C. Kremer, S. Aslanidou, S. Bassauer, M. Hilcker, A. Krugmann, P. von Neumann-Cosel, T. Otsuka, N. Pietralla, V. Y. Ponomarev, N. Shimizu, *et al.*, Phys. Rev. Lett. **117**, 172503 (2016).

[51] T. Togashi, Y. Tsunoda, T. Otsuka, and N. Shimizu, Phys. Rev. Lett. **117**, 172502 (2016).

[52] T. Materna, W. Urban, K. Sieja, U. Köster, H. Faust, M. Czerwiński, T. Rząca-Urban, C. Bernards, C. Fransen, J. Jolie, *et al.*, Phys. Rev. C **92**, 034305 (2015).

[53] I. N. Gratchev, G. S. Simpson, G. Thiamova, M. Ramdhane, K. Sieja, A. Blanc, M. Jentschel, U. Köster, P. Mutti, T. Soldner, *et al.*, Phys. Rev. C **95**, 051302 (2017).

[54] S. Chen, P. Doornenbal, A. Obertelli, T. R. Rodríguez, G. Authelet, H. Baba, D. Calvet, F. Château, A. Corsi, A. Delbart, *et al.*, Phys. Rev. C **95**, 041302 (2017).

[55] A. Gade, T. Baugher, D. Bazin, B. A. Brown, C. M. Campbell, T. Glasmacher, G. F. Grinyer, M. Honma, S. McDaniel, R. Meharchand, *et al.*, Phys. Rev. C **81**, 064326 (2010).

[56] T. Motobayashi, Y. Ikeda, K. Ieki, M. Inoue, N. Iwasa, T. Kikuchi, M. Kurokawa, S. Moriya, S. Ogawa, H. Murakami, S. Shimoura, Y. Yanagisawa, T. Nakamura, Y. Watanabe, M. Ishihara, T. Teranishi, H. Okuno, and R. Casten, Phys. Lett. B **346**, 9 (1995).

[57] T. Glasmacher, Annu. Rev. Nucl. Part. Sci. **48** (1998).

[58] A. Gade and T. Glasmacher, Prog. Part. Nucl. Phys. **60** (2008).

[59] J. M. Cook, T. Glasmacher, and A. Gade, Phys. Rev. C **73**, 024315 (2006).

[60] F. Delaunay and F. M. Nunes, J. Phys. G **34**, 2207 (2007).

[61] O. B. Tarasov and D. Bazin, Nucl. Instrum. Methods Phys. Res. B **376**, 185 (2016).

[62] V. M. Bader, A. Gade, D. Weisshaar, B. A. Brown, T. Baugher, D. Bazin, J. S. Berryman, A. Ekström, M. Hjorth-Jensen, S. R. Stroberg, *et al.*, Phys. Rev. C **88**, 051301 (2013).

[63] D. Weisshaar, A. Gade, T. Glasmacher, G. F. Grinyer, D. Bazin, P. Adrich, T. Baugher, J. M. Cook, C. A. Diget, S. McDaniel, *et al.*, Nucl. Instrum. Methods Phys. Res. A **624**, 615 (2010).

[64] K. Moschner, A. Blazhev, J. Jolie, N. Warr, P. Boutachkov, P. Bednarczyk, K. Sieja, A. Algora, F. Ameil, M. A. Bentley, *et al.*, Phys. Rev. C **94**, 054323 (2016).

[65] D. Mücher, in *AIP Conf. Proc.*, Vol. 1090 (2009) p. 587.

[66] D. Mücher, Ph.D. thesis, Universität zu Köln (2009).

[67] J.-M. Régis, J. Jolie, N. Saed-Samii, N. Warr, M. Pfeiffer, A. Blanc, M. Jentschel, U. Köster, P. Mutti, T. Soldner, *et al.*, Phys. Rev. C **90**, 067301 (2014).

[68] T. Rząca-Urban, K. Sieja, W. Urban, M. Czerwiński, A. Blanc, M. Jentschel, P. Mutti, U. Köster, T. Soldner, G. de France, *et al.*, Phys. Rev. C **95**, 064302 (2017).

[69] C. Mazzocchi, R. Grzywacz, J. C. Batchelder, C. R. Bingham, D. Fong, J. H. Hamilton, J. K. Hwang, M. Karny, W. Królas, S. N. Liddick, A. C. Morton, P. F. Mantica, W. F. Mueller, K. P. Rykaczewski, M. Steiner, *et al.*, The European Physical Journal A - Hadrons and Nuclei **25**, 93 (2005).

[70] M. Albers, N. Warr, K. Nomura, A. Blazhev, J. Jolie, D. Mücher, B. Bastin, C. Bauer, C. Bernards, L. Bettermann, *et al.*, Phys. Rev. Lett. **108**, 062701 (2012).

[71] F. Flavigny, P. Doornenbal, A. Obertelli, J.-P. Delaroche, M. Girod, J. Libert, T. R. Rodriguez, G. Authelet, H. Baba, D. Calvet, *et al.*, Phys. Rev. Lett. **118**, 242501 (2017).

[72] B. A. Brown and W. D. M. Rae, Nuclear Data Sheets **120**, 115 (2014).

[73] D. R. Entem and R. Machleidt, Phys. Rev. C **68**, 041001 (2003).

[74] M. Hjorth-Jensen, T. Kuo, and E. Osnes, Phys. Rep. **261**, 125 (1995).

[75] O. V. Bespalova, T. A. Ermakova, E. A. Romanovskii, T. I. Spasskaya, and A. A. Klimochkina, Bulletin of the Russian Acad. of Science: Phys. **73**, 816 (2009).

[76] M. Hjorth-Jensen, "Computational environment for nuclear structure (cens)," All codes used to generate the effective interactions are available at https://github.com/ManyBodyPhysics/CENS. The specific effective interactions and single-particle energies are available from this same repository in CENS/tree/master/FCI/parallel/pnCase/benchmarks/Mass78.

[77] T. J. Mertzimekis, N. Benczer-Koller, J. Holden, G. Jakob, G. Kumbartzki, K.-H. Speidel, R. Ernst, A. Macchiavelli, M. McMahan, L. Phair, *et al.*, Phys. Rev. C **64**, 024314 (2001).

[78] K. Sieja, T. R. Rodríguez, K. Kolos, and D. Verney, Phys. Rev. C **88**, 034327 (2013).

[79] N. Pietralla, P. von Brentano, and A. Lisetskiy, Prog. in Part. and Nucl. Phys. **60**, 225 (2008).

[80] C. Delafosse, D. Verney, P. Marević, A. Gottardo, C. Michelagnoli, A. Lemasson, A. Goasduff, J. Ljungvall, E. Clément, A. Korichi, G. De Angelis, C. Andreoiu, M. Babo, A. Boso, F. Didierjean, *et al.*, Phys. Rev. Lett. **121**, 192502 (2018).